DISSERTATION

SYNTHESIS AND CHARACTERIZATION OF METAL CHALCOGENIDE AND METAL OXIDE NANOSTRUCTURES

Submitted By

Ka Yee (Anna) Chick

Department of Chemistry

In partial fulfillment of the requirements

For the Degree of Doctor of Philosophy

Colorado State University

Fort Collins, Colorado

Spring 2008

COLORADO STATE UNIVERSITY

January 10th, 2008

WE HEREBY RECOMMEND THAT THE DISSERTATION PREPARED UNDER OUR SUPERVISION BY **KA YEE (ANNA) CHICK** ENTITLED "*SYNTHESIS AND CHARACTERIZATION OF METAL CHALCOGENIDE AND METAL OXIDE NANOSTRUCTURES*" BE ACCEPTED AS FULLFILING IN PART REQUIREMENTS FOR THE DEGREE OF DOCTOR OF PHILOSOPHY.

Committee on Graduate Work

Charles Henry

Amy Prieto

Tomislav Rovis

Kevin Lear

Adviser – Bruce Parkinson

Department Head

ABSTRACT OF DISSERTATION

"SYNTHESIS AND CHARACTERIZATION OF METAL CHALCOGENIDE AND METAL OXIDE NANOSTRUCTURES"

Metal chalcogenide and metal oxide materials are of interest for sensing and energy conversion applications due to their semiconducting properties. Nanostructures made from such materials, therefore, have potential to work as building blocks for nanoelectronics. Various synthetic methods have been developed for the preparation of different nanostructures. In this dissertation, three different synthetic methods are presented in the preparation of different metal chalcogenide and metal oxide nanostructures. The as-produced nanostructures were characterized by transmission electron microscopy (TEM), high-resolution (HR-) TEM, scanning electron microscopy (SEM), energy dispersive x-ray analysis (EDX), and x-ray diffraction (XRD).

Tantalum disulfide (TaS_2) nanoplatelets were prepared from laser ablation of a TaS_2 target under an argon atmosphere using a nanosecond pulsed Nd:YAG laser (1064 nm). The dimensions and morphology of the nanoplatelets were characterized by TEM and XRD. The effect of the ablation laser power density on the size distribution of the nanoplatelets was studied.

TaS_2 closed-cage nanospheres were prepared from laser irradiation of the dispersion of TaS_2 in *tert*-butyl disulfide (TBS) using a nanosecond pulsed Nd:YAG

DEDICATION

To my loving father, John Chick (1946-1993),

who was always a hard-worker and was characterized by forbearing spirit.

laser in large quantity. And finally for the laser ablation project, MoS_2 nano-octahedra were prepared by using a femtosecond pulsed laser. The dimensions and morphology of these nanostructures were characterized by TEM and HR-TEM.

One dimensional (1-D) tin sulfide (SnS) nanostructures were prepared using a direct one-pot solution phase synthesis technique. A single source precursor, tetrakis-(*N*,*N*-diethyldithiocarbamato)tin(IV), was heated in a mixture of long-chain alcohol (tergitol and diethylene glycol) to produce the nanostructures. Reaction parameters, such as temperature and the duration of the reaction, have been investigated for the effect on yield and nanostructure morphology. The 1-D nanostructures were characterized with SEM/EDX, TEM and XRD.

One dimensional tin oxide (SnO_2) nanostructures were prepared by pyrolysis on a Sn-containing precursor in the presence of trace amount of O_2 with Au-coated silicon substrate. The effect of the reaction parameters (reaction durations, heating temperature, substrate identity, and the precursor source) on the nanostructure morphology has been investigated. The nanostructures were characterized with SEM/EDX, TEM and XRD.

Ka Yee (Anna) Chick

Department of Chemistry

Colorado State University

Fort Collins, CO 80523

Spring 2008

DEDICATION

To my loving father, John Chick (1946-1993),

who was always a hard-worker and was characterized by forbearing spirit.

ACKNOWLEDGEMENT

First of all, my sincere gratitude is directed toward my professor and advisor, Dr. Bruce Parkinson, who has helped me to become a better scientist and educator over the past few years, through his wisdom and guidance. I would like to thank my post-doctoral advisor Dr. Manashi Nath who gave freely of her time and intellect whenever I needed help with my experiments and writing. I am also grateful to every group members from the Parkinson group, together we have been through one of the most precious time of our life. Throughout this process I have learned more about myself and what I am capable of than even the chemistry I studied

Writing a dissertation and completing my Ph.D has been one of the most difficult, rewarding, and long experiences I could ever imagine for my family and friends. They have all been supportive, and understanding. There have been two people who more than any others I would not have been able to accomplish my goal of graduation without, my mother who has sacrificed so much and been so forgiving. My Fiancé, Brett has always been there for me no matter what I needed, no matter how irrational or extraordinary.

Finally, I am thankful to my Rheumatoidologist, Dr. Richard Erickson, who tried to keep my joints in good shapes for many years. I would not have been able to reach this point without his help.

Table of Contents

Index of Figures

Index of Table

Preface

On December 29th, 1959, Richard Feynman gave a lecture "There's Plenty of Room at the Bottom" at the American Physical Society meeting at Caltech.[1] In his speech, Dr. Feynman discussed the possibilities and the problems of research into the miniaturization of materials. This classic lecture opened up scientists' views on material science. Fifty years ago, a computer with equal processing power to an iphone took up an entire warehouse. Nanotechnology is the future of miniaturization, from electronic devices, to space travel, to medicine, to everyday consumer applications.

The major advancement in nanotechnology came in 1985, when Kroto and his colleagues discovered C_{60} Fullerene. The C_{60} Fullerene is the most abundant form of carbon fullerenes, with a structure similar to graphite (as carbon atoms are sp^2 hybridized) but in a curved-close-cage fashion. In 1991, Iijima discovered the cylindrical structures of fullerene, which today, are commonly known as carbon nanotubes. These two important discoveries resulted in the "nanoscience research fever" of the 1990s. Because of this research, nanomaterials (such as MoS_2 nanotubes, fullerene-like WS_2) other than carbon have been synthesized in quantity and adopted in many commercial and scientific applications.

Exactly how small is "nano"? Using the human body as an example, each human hair is approximately 100,000 nm, and a blood cell is approximately 7,500 nm, while a carbon nanotube is measured in individual nanometers [Figure 1].[2]

Obviously, substances in nanoscale cannot be seen by the naked eye; therefore techniques such as transmission electron microscopy (TEM), and scanning electron microscopy (SEM) must be utilized to image nanomaterials.

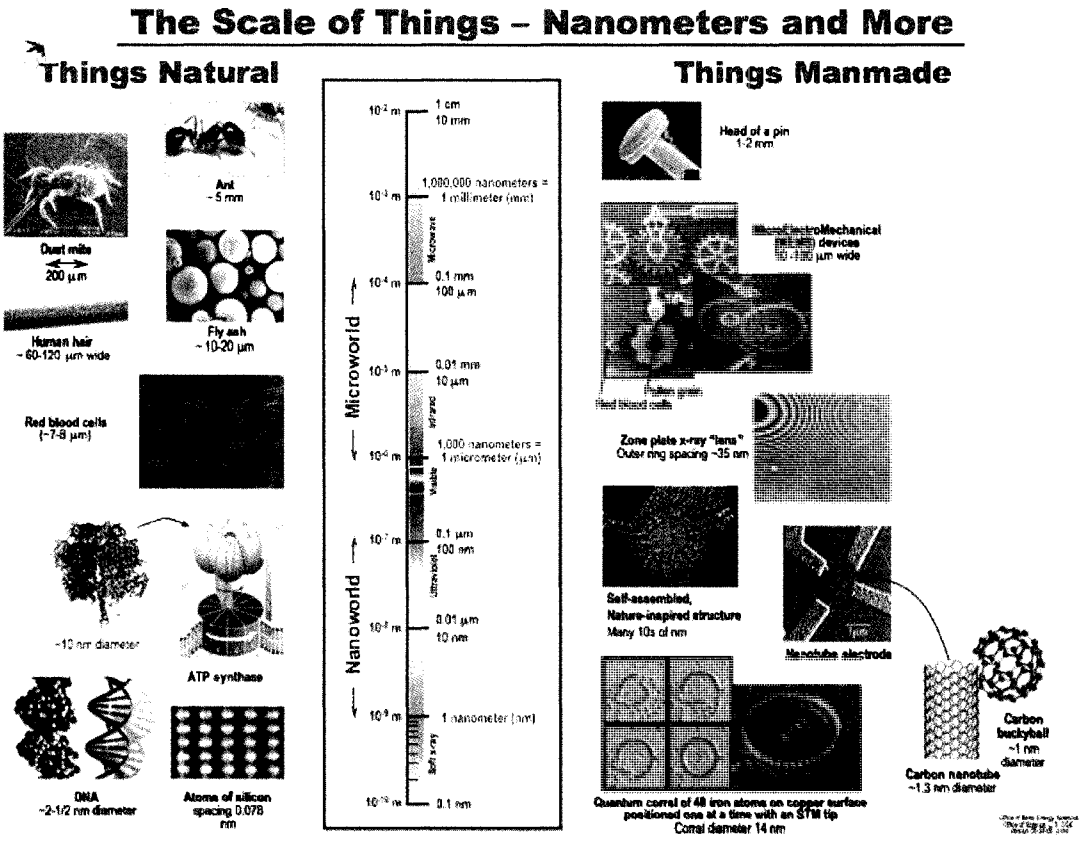

Figure P.1 Scale of nanometers and others.

The top-down method has been used to produce micro- to nano- scale devices and materials; however, the top-down method is approaching its limits. As a result, the bottom-up method becomes necessary for the continuation of material miniaturization. Synthesizing nanoparticles, which is the foundation of the bottom-up approach, with the preferred materials and structures in an efficient way is one important topic in the nanotechnology.

My research project is focused on metal chalcogenide and metal oxide nanostructure synthesis, prepared by three different synthetic approaches: laser ablation, solution phase synthesis with mixed solvent, and pyrolysis in a furnace. In most experiments, we applied a single source precursor as the starting material to simplify the procedures. In the laser ablation projects, different experimental conditions, such as the inert gas and its pressure, and the laser power, were alternated. In the colloidal synthesis project, single source precursor was suspended in different surfactants. Other reaction parameters, such as the reflux temperature, and duration, were also adjusted. In the pyrolysis, single source precursors were heated at different temperatures and different reaction durations. The goal of the research projects is to gain better understanding of different synthetic processes for gaining the ultimate control in size, and shape of the as-synthesized inorganic nanomaterials. Some improvements have been made, however, a lot more still needs to be done. As said by Dr. Feynman, "There's Plenty of Room at the Bottom".

Reference

1. Merkle, R. C., *Transcripts of There's Plenty of Room at the Bottom* [online]. Available: http://www.zyvex.com/nanotech/feynman.html [accessed 18 September 2007]
2. DOE Office of Basic Energy Sciences, *The Scale of Things* [online]. Available: http://www.science.doe.gov/bes/scale_of_things.html [accessed 18 September 2007]
3. Lu, W.; Lieber, C. M., Nanoelectronics from the bottom up. *Nature Mater.* **2007**, 6, 841-850.

Chapter 1: Layered Structure Metal Chalcogenides (LMCs) and Their Nanostructures

Layered metal chalcogenides (LMCs) have a similar structure to graphite, and have been the subject of study and experimentation by scientists for many years. Unlike graphite, LMCs are more diverse in composition, and can have different structures. The pseudo-2-dimensional (2D) structure of these materials gives them intriguing physical and electronic properties, which can be useful in many applications. MoS_2 for instance, can be used as a solid-state lubricant in a wide range of temperatures.[1,2] MoS_2 and WS_2 have been utilized as catalysts for hydrodesulfurization and hydrodenitrogenation.[3,4] WSe_2 has been incorporated into field-effect transitors.[5] TiS_2 and MoS_2 have been used for cathodes in lithium nonaqueous batteries.[6] Another important property of this class of compounds is that the layered structures can be modified through intercalation of molecular or atomic species.

1.1 Structural and electronic characteristics

1.1.1 General features

Binary compounds, such as metal monochalcogenides and metal dichalcogenides, often crystallize in a layered structure. Using a metal

dichalcogenide as an example, a metal or transition metal, denoted M, is nested between alternating layers of chalcogen atoms, X. Together they form a strong covalently bound sandwich, X-M-X, with no net charge [Figure 1.1]. The sandwich stacks layer upon layer by weak van der Waals forces, with a large interlayer spacing. Since the intra-layer interactions are much stronger than the van der Waals forces, the structure is considered a pseudo-2-D layer resulting in anisotropic chemical and physical properties. Such layered materials can be cleaved preferentially between the interlayers, without the formation of dangling bonds.

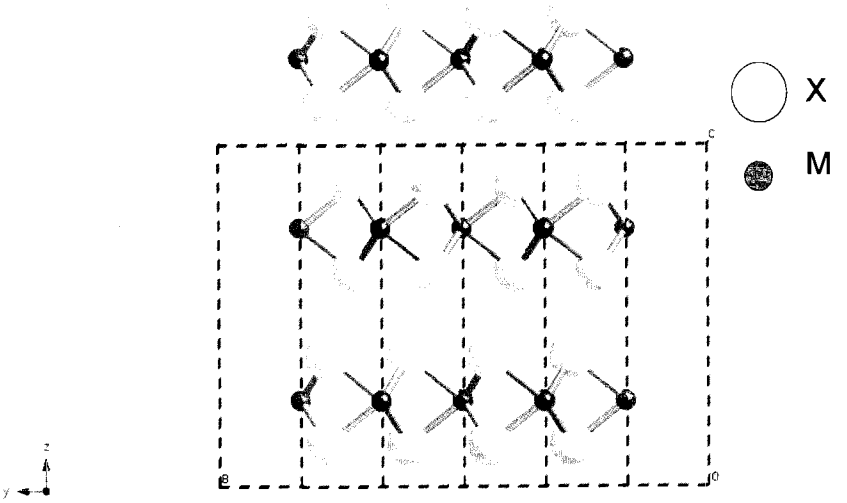

Figure 1.1. The sandwich layered structure of a 2H metal dichalcogenide.

The surfaces formed by separating two adjacent layers are termed van der Waals surfaces. These surfaces are usually hexagonally close-packed, and tend to be chemically inert. Within each interlayer, the metal atom is usually sixfold

coordinated to the chalcogen atoms with two possible geometries: trigonal prismatic and octahedral.[7] In the case of metal dichalcogenides that were used in a big portion of this work, the metal atom is six-fold coordinated to chalcogen atoms. As for other metal chalcogenides, the metal atom can also be coordinated to three chalcogen atoms (for instance, in the case of SnS, each tin atom is coordinated to three sulfur atoms). These materials can still, however, form layered structures.

Polytypism arises from the different stacking sequences of these pseudo-2D layers [Figure 1.2], as the result, a typical layered compound usually comes in more than one polytypes. For instance, in the case of MoS_2, the two most abundant polytypes are 2-H and 3-R where the 2-H is more common than the other. Table 1.1 lists some examples of common polytypes of metal dichalcogenides.

Table 1.1 Examples of common polytypes.

Polytypes	Space group	Metal coordination	Layer stacking sequence
1-T	$P\bar{3}m1$	Octahedral	AbC
2-Ha	$P6_3/mmc$	Trigonal prismatic	BcB AcA
2-Hb	P6m2	Trigonal prismatic	BcB AbA
2-Hc	$P6_3/mmc$	Trigonal prismatic	BaB AbA
4-Ha	$P\bar{6}m2$	Trigonal prismatic	BcB AcA BcB CaC
6-R	R3m	Mixed	BcB CaB CaC AbC AbA BcA

The electronic properties of LMCs are anisotropic due to the weak interactions between interlayers. For example, the conductivities of group IV and VI dichalcogenides are different when measuring parallel or perpendicular to the growth plane.[8] The stacking symmetry should have less effect on electronic properties than the metal coordination. In some rare cases, however, different polytypes may differ in their electronic properties due to contributions from other factors. For example, the two commonly seen polytypes of TaS_2, 1-T and 2-H TaS_2, have different resistivities, as shown in Figure 1.3.[9] The differences could be the result of charge density waves (CDW). LMC materials range from semiconducting to superconducting. In the case of transition metal chalcogneides, the electronic structure depends mainly on the d-orbitals of the metal atom,[7] though other interesting electronic phenomena arise from the layered structure itself.

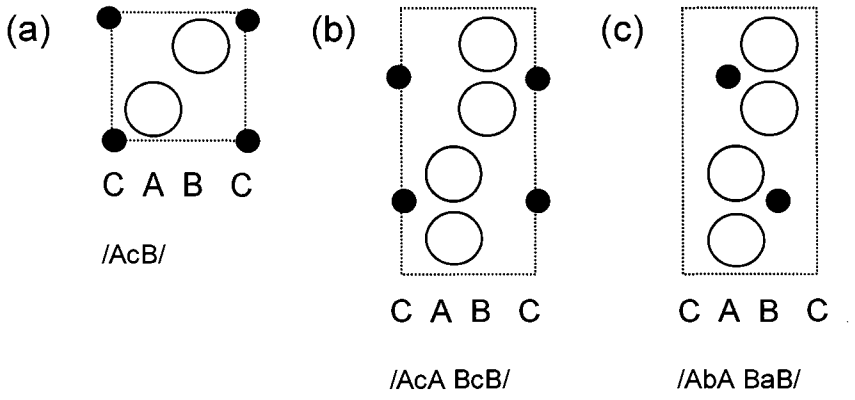

Figure 1.2 Some common polytypes in the $(11\bar{2}0)$ direction with different stackings.

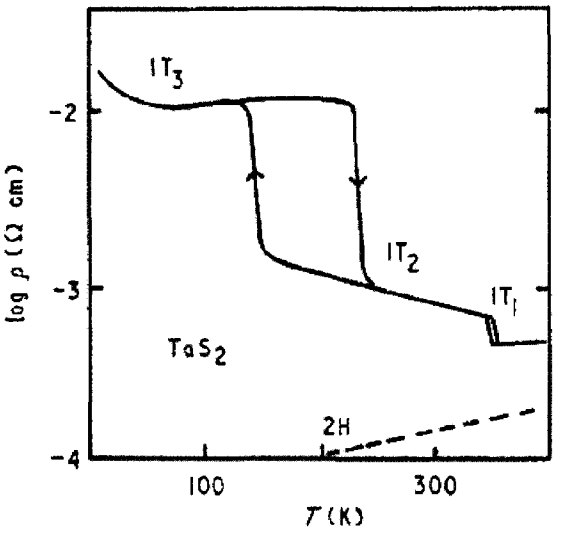

Figure 1.3 The temperature dependence of the resistivity of 1-T and 2-H TaS_2.[9]

One intriguing phenomenon, called charge density wave (CDW), is observed in transition metal dichalcogenides (TMDCs). CDW describes a low energy ordered state of solid. It can occur in anisotropic, 2-D materials (such as TMDC) at low temperature, as electrons have limited mobility in the transverse direction.[10] For example, 1T-TaS_2, one of the target materials in this thesis, exhibits four distinct temperature-dependent CDW phases. In CDW, a periodic static lattice distortion occurs in order to stabilize the conduction electron gas [Figure 1.4]. The total free energy of the material is reduced due to the distortion of both ion lattice and electrons gas. The CDW can be incommensurate or commensurate to the lattice spacing. Below a specific threshold of the electric field, which is structure dependent, no conduction occurs. With sufficient electric field, however, the CDW may slide freely resulting in a conducting and in some cases superconducting materials. The CDW

materials are different from the regular metals since they do not obey Ohm's law. The current can show large increases with a small increase in voltage. LMC materials, due to the result of CDW, can potentially be used as tunable capacitors in electronic circuits, or in the detection of electromagnetic radiation.[10]

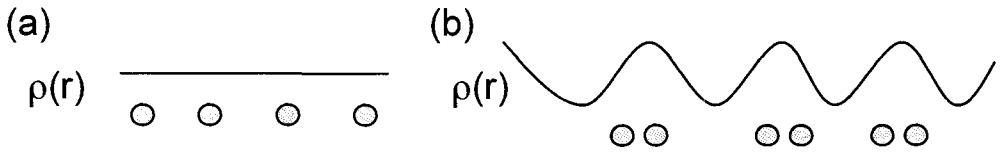

Figure 1.4 A basic representation of CDW, with the blue dots as ions, and black line as the charge density. (a) T> Tp (Peierls temperature), when phonons and electrons are not coupled. (b) T< Tp, when phonons and electrons are interacted resulting the distortion static lattice and the periodic modulations of the charge density.

1.2 Bulk materials vs. nano materials

LMCs with highly folded structures were known for several decades before the discovery of C_{60} fullerene. These rag-like and tubular structures of MoS_2 were found in 1979.[11,12] However, this discovery was not appreciated until after the discovery of C_{60}. The C_{60} fullerene is the most abundant fullerene, with a structure similar to graphene sheet (sp^2 hybridized carbon atoms, with each atom attached to three others) but in a closed-cage fashion. The carbon nanotube, another closed-cage structure of graphene, was discovered by Iijima in 1991 that was made of graphite sheets rolled into tubes.[13] The LMCs nanostructures received attention when Tenne

et al. demonstrated that Mo and W chalcogenides are capable of forming closed structures like carbon nanomaterials.[14]

Similar to graphite, as the LMC materials enter the nano-scale regime, the materials have the tendency to roll up and fold into closed structures.[14] The reason behind this phenomenon is to minimize the energy associated with the edges of the structure. The unsaturated bonds, due to the absence of either metal or chalcogen atoms at the edges, result in different coordination, and thus, destabilize the layers. Such dangling bonds on the edges of the layered materials become more significant as the size of the particles get smaller, further destabilizing the materials. By rolling and or folding into a closed structure, the number of dangling bonds can be reduced or eliminated, thereby, improving the stability of the material.[15] Like carbon, other nanostructures, such as the nested form of the inorganic-fullerene (IF, also known as onion-like), and multi-wall nanotubes are also possible. The nested structures consist of the metal chalcogenide layers stacked perpendicular to the basal plane. With weaker X-X (chalcogen atoms) interactions between each layer, distortion of the structure during the "folding-process" is possible. In many instances such nanostructures exhibit a slight expansion of the lattice constant.

1.2.1 Nanostructures overview

In this section, different types of nanostructures that have been prepared from LMCs will be reviewed. This will be followed by a detail discussion of the various synthetic methods for the preparation of both bulk and nano TMCs in the next chapter.

I. Nanoparticles [Figure 1.5-1.9]: Different morphologies of nanoparticles have successfully been made. One of the well-known morphologies is the "Tenne" structure. Generally such structures can only be found in the layered materials, such as MoS_2. These nanostructures appear to be closed-cage favors by the energy minimization from dangling bonds elimination of the layered materials. The nested-like structure can be spherical or polyhedral in shape, depending on the size (i.e. number of layers) and the nature of the materials [Figure 1.5].[16] Various synthetic methods are employed for the production of the nested nanostructure, such as conversion of metal oxides under H_2X atmosphere, arc-discharge with a Mo-MoS_2 powder anode submerged in DI water (Chapter 2 will cover various synthetic methods in more details).

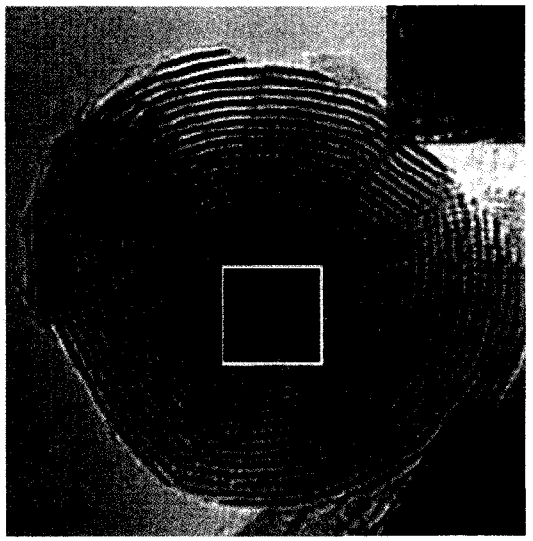

Figure 1.5 High resolution TEM (HR-TEM) image of the ReS_2 nanoparticles encapsulating ReO_2 in its core.[16]

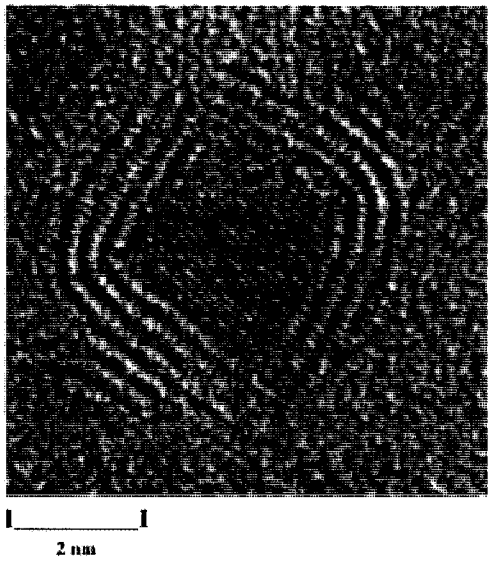

Figure 1.6 TEM image of the MoS_2 nano-octahedron obtained by laser ablation.[17]

The "Tenne" structures are usually described as fullerene-like nanostructures. They are much larger in size when compared to C_{60} fullerene. The first "true" inorganic fullerene is found to be the small (in 3-6 nm) nano-octahedra in discrete size obtained by laser ablation [Figure 1.6].[17] Experimental and mathematical results indicate that nano-octahedra structures are stable in this size range, beyond this size however, the quasi-spherical Tenne structure is found to be the dominant size.

Nanoparticles are not limited to nested structures. Nanoclusters have been prepared by colloidal synthesis with the LMC materials [Figure 1.7].[18] The sizes of nanoclusters are small, ranging from 2.5 to 9 nm. Electron diffraction results indicate that these nanocluster consists of the single sheet structures. A similar structure to nanocluster, nanoplatelets, consists of multiple sheets of the LMC materials, has also been prepared by the laser ablation methods.[19]

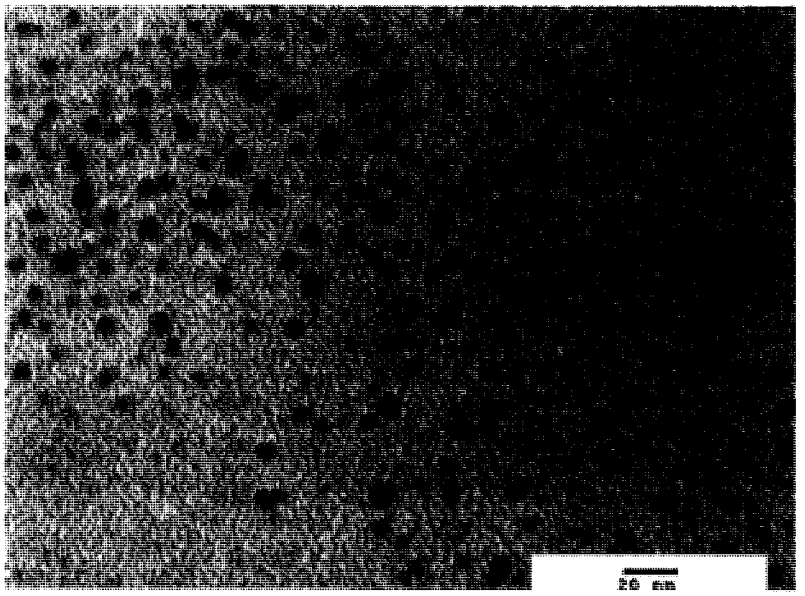

Figure 1.7 TEM image of the $MoSe_2$ nanoclusters.[18]

Another unique structure of nanoparticles is the nanobox [Figure 1.8].[20] In a typical spray pyrolysis of aqueous solutions, the spherical, nested-like nanoparticles, such as MoS_2 fullerene, can be obtained. In the case of WS_2, in contrast, spraying aqueous precursor solutions does not lead to the exclusive of WS_2 fullerene. Some WS_2 nanoparticles adopt the nested structure, in the shape of a parallelepiped, with multilayer walls and an empty core, and thus, are described as the "closed nanobox". The size of these rectangular structures ranges from ten to a few hundred nm. These structures exhibit the same length/width ratio, approximately of 1.9 regardless of their size.

Figure 1.8 TEM image of a WS_2 nanobox.[20]

Other nanoparticles with different shapes, such as nanospheres and nanorods [Figure 1.9] can be prepared via solution-phase synthesis (hydrothermal reaction and colloidal synthesis), or by ultrasound-assisted cracking process.[21-23] Monodisperse nanocrsytals can be produced if the nucleation and growth stage are controlled during synthesis.

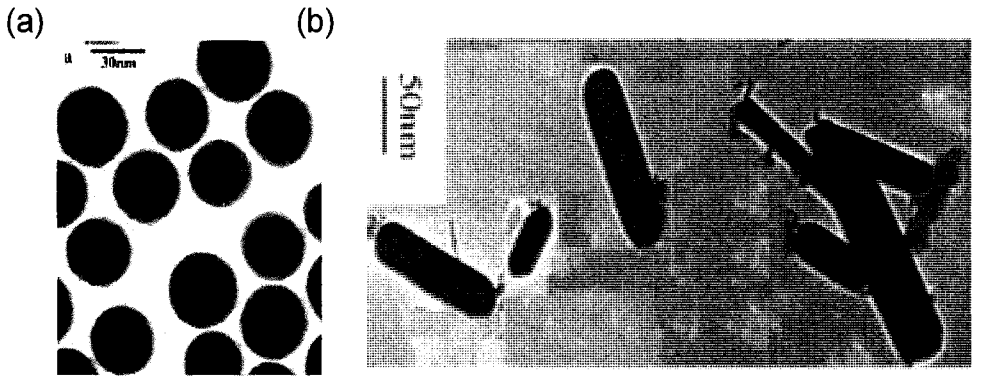

Figure 1.9 TEM images of MoS_2 nanoparticles with different shapes: (a) nanospheres, (b) nanorods.[21-22]

II. Nanotubes [Figure 1.10-1.11]:[14] These structures appear to be fullerene-like, but elongated 1-D structures. Similar to the closed-cage structure mentioned above, the basic layered structure allows the "folding" process to eliminate dangling bonds. Nanotubes are either opened-end or closed-end, depending on the termination steps of their respective synthetic processes. The defects and strain relief induce the positive curvature that can be observed from the closed-end nanotubes (or fullerene-like) materials. Various shapes of nanowire tips have been observed, as they can be polygonal caps and even rectangular tips (as shown in Figure 1.11).[15] In the case of metal dichalcogenides, the absence of metal or chalcogen atoms causes the formation of triangular or rhombohedral point defects in the tip of the nanowires. As a general rule, to form crystalline closed-cage nanostructures, layered materials are required. Different synthetic methods have been employed to prepare nanotubular structures, such as the well-known template method, and chemical vapor transport (CVT). (Details of various preparation methods will be discussed in more detail in Chapter 2.)

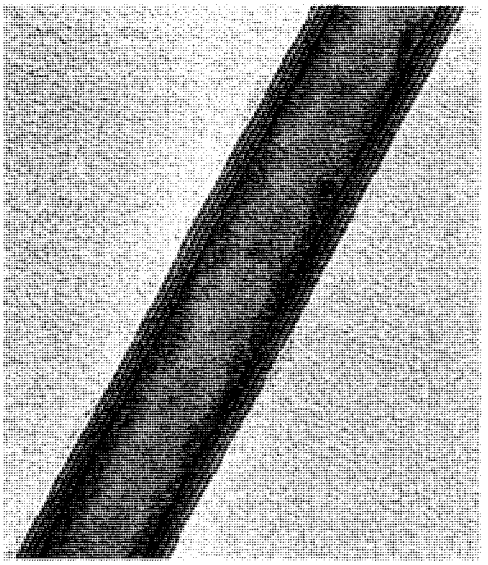

Figure 1.10 TEM image of WS_2 nanotubes.[14]

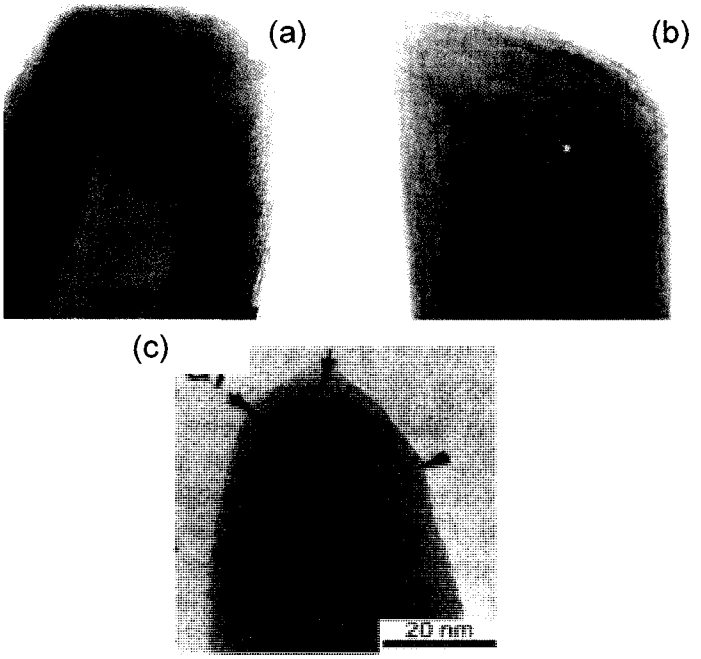

Figure 1.11 TEM images of nanotubes displaying various tip-closure.

(a) $Mo_{1-X}W_XS_2$ nanotube (b) WS_2 nanotube (c) Nb-W-S nanotube.[15]

III. Nanowires [Figure 1.12]:[24] Nanowires are another example of 1-D nanostructures. By definition, nanowires are referred to as an anisotropic nanocrystal with large aspect ratio (length/diameter). Unlike nanotubes, nanowires do not form hollow cages. One can envision them as the elongated version of nanorods, which were referred as nanoparticles previously. Different synthetic mechanisms for nanowires, such as vapor-liquid-solid (VLS), have been developed. Such growth mechanism of 1-D nanostructures should be similar to other nanocrystal growths, but there are some differences due to the promotion of the crystallization of the solid-state structures along one direction. The synthetic procedures can be summarized as follows:[25] (a) intrinsic growth of the anisotropic crystal structure; (b) directed formation by templating with 1-D structure materials; (c) introduction of a liquid/solid interface in order to reduce the symmetry of the nucleations/seeds; (d) introduction of a capping agent to control the growth kinetics of various facets of the nucleations; and (e) self-assembly of nanoparticles. The 1-D nanostructures are of importance as they may be applied as interconnects and functional components in the fabrication of nanoscale electronic and optoelectronic devices.

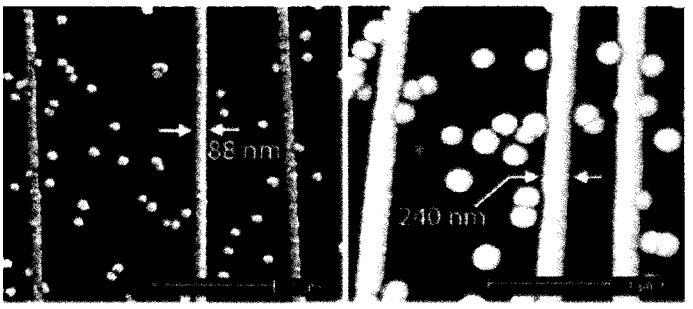

Figure 1.12 SEM images of MoS_2 nanowires with different diameters.[24]

1.2.2 Special nanostructures properties

Even though some nanostructured materials are known for consisting of their bulk phases, the chemical/physical properties of the nanostructures can be extremely different from their bulk. The deviation in properties provides the opportunity to tailor materials with the desired properties. Here, several distinct deviations in properties from the general nanostructures (including layered and not layered materials) to their bulk will be described.

I. Surface atoms /bulk atoms ratio

Reactivity

Here, the term "bulk" refers to materials inside the particle, regardless of the particle's shape. The reactivity of the atoms, due to the differences in coordination, can be different depending on the locations of the specific atom within the matter. Atoms on the surfaces, therefore, reveal higher reactivity than their bulk in general. As the sizes of the particles are reduced, more atoms are exposed on the surface. The more atoms found on surfaces, the more reaction sites are available for reaction. In conclusion, the smaller the particle, the higher the surface atoms/bulk atoms ratio is, and thus, the reactivity is improved. This is very important to the petroleum refining and catalyst industries (for hydrodesulfurization and methanation),[4,26,27] since higher reactivity allows more reactions (or reactions with faster rates) to occur. Furthermore, nanomaterials (usually 1-D structures) can also be used as chemical sensors.[28, 29] Chemical nanosensors are of interests due to their potential for detecting low concentration of analyte with the size small enough to be employed *in vivo* or on

a microchip. The high surface/bulk ratio allows more surface adsorption of the analyte molecules; therefore, improving the sensitivity and the response time of the sensors.

Melting point

Another example of property deviation attributed to increasing surface/bulk ratios, is melting point depression. The surface atoms are proportional to the surface energy of the materials, which are inversely proportional to the melting points of the materials. As a result, nanomaterials have been reported with lower melting points than their parent materials. The capability of cutting, and welding nanomaterials can therefore be achieved at relatively lower temperatures.

II. Effect on the tip apex

Tip apex refers to the pointed end of a tip. In the case of nanotubes, the diameters of the 1-D structures are extremely small, which affect the resulting dimensions of the tip apex to a large degree, and therefore, yield the extremely sharp structures. These extremely sharp materials are useful in the microscopy industry. Materials such as WS_2 nanotubes were mounted on the ultrasharp Si tip to fabricate a good atomic force microscopy (AFM) tip.[30] The specially designed tips allow the control of the tip apex ratio, and therefore, are suitable for the analysis of deep and narrow features with the AFM image.

III. Quantum size effect in semiconductor nanoparticles

Quantum size effects, described by the simple particle-in-a-box model, is a consequence of the confinement of electrons and holes within a reduced-size material.

This phenomenon allows semiconductors to alter their bandgaps based on their dimensions. The absorption bands of semiconducting nanoparticles tend to be blue-shifted as their size decrease (when $R<a_B$, where R is the nanoparticle radius, and a_B is the Bohr radius), along with the creation of the discrete, molecule-like electronic states. The size dependence of the bandgap in nanowires is weaker than nanodots, however the basic trend of dependency should be the same. As in the case of semiconducting nanowires, light absorption and emission is highly dependent on polarization (maximum on the long axis of the nanowires).[31] The anisotropy of polarization is likely caused by the sharp dielectric contrast between the nanowires and their surrounding.

Different types of semiconductor exhibit the quantum size effect, for example, the well-studied CdSe quantum dots, CdSe nanorods, CdTe tetrapods.[32-34] LMCs nanomaterials have also reported the quantum size effect, for example, MoS_2 and WS_2 nanoclusters prepared in the range of 2.5-9 nm. The direct absorption from the absorption spectra blue-shifted due to the quantum confinement.[35,36] Similar results were also reported in $MoSe_2$ and WSe_2 nanoclusters.[18]

IV. The improvement in stability (with the closed-cage nanostructure)

As mentioned previously, when the surface/bulk ratio is increased, the reactivity of the materials can also be increased. On the other hand, the global stability of nanostructures can be improved in the case of closed-cage structure. As the LMC materials roll up and fold into the closed structure, the dangling bonds from the edge of the layered materials are eliminated. The resulting seamless, closed

structure prevents oxygen and water intake, thus improving the stability of the materials under an ambient environment. The closed-cage nanoparticles can act as nano-ballbearings, due to the effective rolling and sliding motions on the contact surfaces. The lubricant performance of the nanomaterials, such as MoS_2 fullerene-like materials, can therefore be improved as the materials exhibit ultra-low friction and wear in oxygen and humidity.[37,38]

V. Mechanical properties

Besides the unique electronic and physical properties described above, nanomaterials also display distinct mechanical properties. For example, the Young's modulus of individual BN nanotube is found to be 1.18 TPa, comparable to that of high quality carbon nanotubes.[39] Nanoparticles have also been added into the polymer to increase the strength of the materials.[40] Different theories of the improved strength by size reduction have been made, including the Hall-Petch effect which states that the strength of polycrystalline materials increases, with decreasing grain size, due to the effective disruption of dislocation motion (sliding) by grain boundaries.[41] In a single crystal nanostructure, the lower density of line defects also leads to the increase in mechanical strength, stiffness and toughness. The improved strength in nanomaterials allows potential applications such as using as the mechanical actuator and using in the composite materials.

1.3 Materials used in this work

1.3.1 Materials for the laser ablation projects [Chapter 3 &4]:

I. Molybdenum sulfide (MoS_2)

MoS_2 was the parent material, as well as the product, of the laser ablation project. Bulk 2-H MoS_2, the commonly seen polytype, displays a hexagonal layered structure ($P6_3/mmc$), with two sandwich layers per unit cell (c=12.3 Å). MoS_2 is commonly used as a catalyst in the hydrogenation for the conversion of coal to liquid fuel. It can also be used as the ingredient in solid-state-lubricant, as its fullerene-like structure exhibits superior lubrication ability, with more rolling motions.[37,38] MoS_2 is a semiconducting materials with band gap of 1.23 eV.[42] It displays a better photostability since both its valence and conduction bands are primarily composed of nonbonding Mo *4d* orbitals (i.e. little bond extension and weakening from photoexcitation). As a result, MoS_2 can be very useful in optical or photochemical applications.

Since the first LMCs material with fullerene-like structure prepared by Tenne, *et al.*, many different synthetic methods for MoS_2 nanostructures production have been developed. MoS_2 clusters have been produced within the inverse micelle,[43] or by sonication of the bulk powder in water under Ar-He atmosphere.[44] The fullerene-like (Tenne structure) MoS_2 structures were prepared via electron irradiation of the grounded MoS_2 powder with high energy electrons (0.5 MeV).[45] MoS_2 nano-octahedrons, which are believed to be the true inorganic fullerene structures, were prepared by Parilla, *et al.* via pulsed laser ablation.[17] MoS_2

nanotubes have been prepared via templated methods[46] or by gas-phase reactions (either annealing the oxidized transition metals, or by thermal decomposition) involving a trisulfide intermediate.[47]

II. Tantalum sulfide (TaS_2)

TaS_2 is a group V dichalcogenide which superconducts at a relatively high temperature. TaS_2 adopts several different polytypes. The thermodynamically stable phase is 2-H at room temperature, with two sandwich layers as a unit cell structure ($P6_3/mmc$). Another commonly seen polytype, 1-T TaS_2 displays a distorted CdI structure ($P\bar{3}m1$). TaS_2 has been tested for the use in lithium ion batteries. TaS_2 is interesting due to its charge density wave phase (CDW) behavior, as four distinct temperature-dependent CDW phases have been reported for 1-T TaS_2.

Few success has been made in generating TaS_2 nanostructures. TaS_2 nanotubes, with flat rectangular tips, have been generated by reducing TaS_3 in H_2 at an elevated temperature (1270 °C).[48] TaS_2 fullerene-like nanoparticles have been synthesized by a gas-phase reaction by feeding the precursor gas ($TaCl_5$, N_2, and H_2S) into the furnace.[49] Thin films of TaS_2 have also been produced from [$Ta(NMe_2)_5$] and *t*-BuSH by aerosol-assisted chemical vapor deposition on glass at 225 °C.[50]

1.3.2 Materials for the solution phase synthesis project [Chapter 5]:

I. Tin Sulfide (SnS)

Tin sulfide is a member of the IV-VI group semiconductors. Variety of phases, such as SnS, SnS_2, Sn_2S_3, have been found due to the versatile coordinating

characteristics of tin and sulfur. The two most common tin sulfide materials are tin monosulfide and disulfide (SnS and SnS_2 respectively). Interestingly, both compositions (SnS and SnS_2) reveal layered structures. SnS will be discussed here, since this is the product in the solution phase synthesis project. The common phase of SnS obtains orthorhombic structure. As with other LMC materials, SnS (also known as herzenbergite) consists of layer stacking perpendicular to the *b-axis*, as Sn and S atoms are covalently bound. Each sandwich layer is weakly stacked by the van der Waals forces. With narrow band-gap of 1.08 eV (the indirect),[51] SnS is a p-type semiconducting material that can be used as a sensor in the environmental industry.[52] Its high conversion efficiency also makes it a good photovoltaic material.[51]

Various methods have been employed in synthesizing different SnS nanostructures. Belt-like SnS micro-size crystals have been synthesized from tin (II) chloride/sulfur/ethylenediamine solution.[51] Thermal decomposition of sulfur-containing organotin molecular precursors have been used to produce bulk SnS.[53] Nanoparticles of SnS have been prepared by refluxing tin and sulfur in diglyme.[54] The unusual zinc blende (ZB) structure of SnS nanocrystals has also been produced by thermally decomposing tin chloride and elemental sulfur in a primary amine solvent.[55] Rod-like tin sulfide nanocrystals with different compositions and phases (SnS, SnS_2, Sn_2S_3) have been prepared via solvothermal reaction as well as by laser ablation.[56]

1.3.4 Materials for the gas phase synthesis project [Chapter 6]:

I. Tin Oxide (SnO_2)

Even though numerous metal oxides have phases that are lamellar in structure, tin oxide (SO_2) does not reveal as a layered material. Tin oxide is discussed here since it is the product generated from pyrolyzing of tin diethyldithiocarbamate, an organotin compound that can be used for SnS/SnS_2 synthesis. The two commonly seen SnO_2 phases are cubic-fluorite, and rutile-type. As an n-type semiconductor with bandgap of 3.6 eV,[57] tin oxide can be used for optoelectronic devices and as a gas sensor for leakage detection of several flammable gases.[58,59]

Different synthetic methodologies have been used in metal oxide nanotube productions. Hydrolysis of metal precursors in a mixture of water, ethanol, or ammonia has been used to produce silica nanotubes. Templated syntheses have also been employed to produce all sorts of metal oxide nanotubular structures.[60,61] A sol-gel method is commonly used in the metal oxide nanomaterials production. For the more specific syntheses of SnO_2 nanostructures, tetragonal rutile-structured SnO_2 nanoribbons have been synthesized via thermal oxidation of elemental Sn powder using $Fe(NO_3)_3$ as oxidizing agent or by vapor-solid gas phase reaction with SnO_2 as the starting materials.[62] Other SnO_2 nanowires have also been produced via solution-phase reactions, followed by calcinations.

Reference:

1. Winer, W. O., Molybdenum disulphide as a lubricant: A review of the fundamental knowledge. *Wear* **1967,** 10, 422-452.

2. Spalvins, T., Morphological and frictional behavior of sputtered MoS_2 films. *Thin Solid Films* **1982,** 96, 281-288.

3. Trakarnpruk, W.; Seentrakoon, B., Hydrodesulfurization activity of MoS_2 and bimetallic catalysts prepared by in situ decomposition of thiosalt. *Ind. Eng. Chem. Res.* **2007,** 46, (7), 1874-1882.

4. Brorson, M.; Carlsson, A.; Topsoe, H., The morphology of MoS_2, WS_2, Co-Mo-S, Ni-Mo-S and Ni-W-S nanoclusters in hydrodesulfurization catalysts revealed by HAADF-STEM. *Catal. Today* **2007,** 123, (1-4), 31-36.

5. Podzorov, V.; Gershenson, M. E.; Klorc, C.; Zeis, R.; Bucher, E., High-mobility field-effect transistors based on transition metal dichalcogenides. *Appl. Phys. Lett.* **2004,** 84, (17), 3301-3303.

6. Whittingham, M. S., Electrical energy storage and intercalation chemistry. *Science* **1976,** 192, (4244), 1126-1127.

7. Wilson, J. A.; Yoffe, A. D., The transition metal dichalcogenides discussion and interpretation of the observed optical, electrical and structural properties. *Adv. Phys.* **1969,** 18, (73), 193-335.

8. Yoffe, A. D., Layered compounds. *Annu. Rev. Mater. Sci.* **1973,** 3, 147-170.

9. Grant, A. J.; Griffiths, T. M.; Pitt, G. D.; Yoffe, A. D., Pressure-induced semimetal-metal and metal-metal transitions in 1T and 2H tantalum disulfide. *J. Phys. C: Solid State Phys.* **1974,** 7, (14), L249-L253.

10. Brown, S.; Gruner, G., Charge and spin density waves. *Sci. Am.* **1994,** 270, (4), 50-57.

11. Chianelli, R. R.; Prestridge, E.; Pecorano, T.; DeNeufville, J. P., Molybdenum disulfide in the poorly crystalline "rag" structure. *Science* **1979,** 203, 1105.

12. Harris, S.; Chianelli, R. R., Catalysis by transition metal sulfides: a theoretical and experimental study of the relation between the synergic systems and the binary transition metal sulfides. *J. Catal.* **1986,** 98, 17-31.

13. Iijima, S., Helical microtubules of graphitic carbon. *Nature* **1991,** 354, 56.

14. Tenne, R.; Margulis, L.; Genut, M.; Hodes, G., Polyhedral and cylindrical structures of tungsten disulfide. *Nature* **1992,** 360, 444-446.

15. Nath, M.; Rao, C. N. R., Inorganic nanotubes. *Dalton Trans.* **2002**, (1), 1-24.

16. Coleman, K. S.; Sloan, J.; Hanson, N. A.; Brown, G.; Clancy, G. P.; Terrones, M.; Terrones, H.; Green, M. L. H., The formation of ReS_2 inorganic fullerene-like structures containing Re_4 parallelogram units and metal-metal bonds. *J. Am. Chem. Soc.* **2002,** 124, 11580-11581.

17. Parilla, P. A.; Dillon, A. C.; Jones, J. G.; Riker, G.; Schulz, D. L.; Ginley, G. S.; Heben, M. J., The first true inorganic fullerenes? *Nature* **1999,** 397, 114.

18. Huang, J. M.; Kelley, D. F., Synthesis and characterization of $MoSe_2$ and WSe_2 nanoclusters. *Chem. Mater.* **2000,** 12, 2825-2828.

19. Chick, K. Y.; Nath, M.; Parkinson, B. A., TaS2 nanoplatelets produced by laser ablation. *J. Mater. Res.* **2006,** 21, (5), 1243-1247.

20. Bastide, S.; Duphil, D.; Borra, J.-P.; Levy-Clement, C., WS_2 closed nanoboxes synthesized by spray pyrolysis. *Adv. Mater.* **2006,** 18, (1), 106-109.

21. Tian, Y. M.; Zhao, X.; Shen, L. C.; Meng, F. Y.; Tang, L. Q.; Deng, Y. H.; Wang, Z. C., Synthesis of amorphous MoS_2 nanospheres by hydrothermal reaction. *Mater. Lett.* **2006,** 60, 527-529.

22. Tian, Y. M.; Zhao, J. Z.; Fu, W. Y.; Liu, Y. H.; Zhu, Y. Q.; Wang, Z. C., A facile route to synthesis of MoS_2 nanorods. *Mater. Lett.* **2005,** 59, (27), 3452-3455.

23. Zheng, X. W.; Zhu, L. Y.; Yan, A. H.; Bai, C. N.; Xie, Y., Ultrasound-assisted cracking process to prepare MoS_2 nanorods. *Ultrason. Sonochem.* **2004,** 11, 83-88.

24. Li, Q.; Walter, E. C.; van der Veer, W. E.; Murray, B. J.; Newberg, J. T.; W., B. E.; Switzer, J. A.; Hemminger, J. C.; Penner, R. M., Molybdenum disulfide nanowires and nanoribbons by electrochemical/chemical synthesis. *J. Phys. Chem. B* **2005,** 109, 3169-3182.

25. Law, M.; Golberger, J.; Yang, P., Semiconductor nanowires and nanotubes. *Amu. Rev. Mater. Res.* **2004,** 34, 84-122.

26. Chen, J.; Li, S. L.; Xu, Q.; Tanaka, K., Synthesis of open-ended MoS_2 nanotubes and the application as the catalyst of methanation. *Chem. Commun.* **2002**, (16), 1722-1723.

27. Brorson, M.; Carlsson, A.; Topsoe, H. The morphology of MoS_2, WS_2, Co-Mo-S, Ni-Mo-S and Ni-W-S nanoclusters in hydrodesulfurization catalysts revealed by HAADF-STEM. *Cata. Today.* **2007**, 123(1-4), 31-36.

28. Varghese, O. K.; Grimes, C. A., Metal oxide nanoarchitectures for environmental sensing. *J. N. N.* **2003,** 3, (4), 277-293.

29. Lee, S. J.; Lee, S. S.; Lee, J. Y.; Jung, J. H., A functionalized inorganic nanotube for the selective detection of copper(II) ion. *Chem. Mater.* **2006,** 18, (20), 4713-4715.

30. Rothschild, A.; Cohen, S. R.; Tenne, R., WS_2 nanotubes as tips in scanning probe microscopy. *Appl. Phys. Lett.* **1999,** 75, (25), 4025-4027.

31. Wang, J.; Gudiksen, M. S.; Duan, X.; Cui, Y.; Lieber, C. M., Highly polarized photoluminescence and photodetection from single indium phosphide nanowires. *Science* **2001,** 293, 1455-1457.

32. Michalet, X.; Pinaud, F. F.; Bentolila, L. A.; Tsay, J. M.; Doose, S.; Li, J. J.; Sundaresan, G.; Wu, A. M.; Gambhir, S. S.; Weiss, S., Quantum dots for live cells, in vivo imaging, and diagnostics. *Science* **2005,** 307, 538-544.

33. Huyuh, W. U.; Dittmer, J. J.; Alivisatos, A. P., Hybrid nanorod-polymer solar cells. *Science* **2002,** 295, 2425-2427.

34. Manna, L.; Milliron, D. J.; Meisel, A.; Scher, E. C.; Alivisatos, A. P., Controlled growth of tetrapod-branched inorganic nanocrystals. *Nat. Mater.* **2003,** 2, 382-385.

35. Wilcoxon, J. P.; Samara, G. A., Strong quantum-size effects in a layered semiconductor: MoS_2 nanoclusters. *Phys. Rev. B* **1995,** 51, (11), 7299-7302.

36. Huang, J. M.; Laitinen, R. A.; Kelley, D. F., Spectroscopy and trapping dynamics in WS_2 nanoclusters. *Phys. Rev. B* **2000,** 62, (16), 10995-11005.

37. Rapoport, L.; Bilik, Y.; Feldman, Y.; Homyonfer, M.; Cohen, S. R.; Tenne, R., Hollow nanoparticles of WS_2 as potential solid-state lubricants. *Nature* **1997,** 387, 791-793.

38. Chhowalla, M.; Amaratunga, G. A. J., Thin films of fullerene-like MoS_2 nanoparticles with ultra-low friction and wear. *Nature* **2000,** 407, 164-167.

39. Chopra, N. G.; Zettl, A., Measurement of the elastic modulus of a multi-wall boron nitride nanotube. . *Solid State Commun.* **1998,** 105, (5), 297-300.

40. Lee, J. Y.; Lim, D. P.; Lim, D. S., Tribological behavior of PTFE nanocomposite films reinforced with carbon nanoparticles. *Composites Part B* **2007,** 38, ((7-8)), 810-816.

41. Schiotz, J.; Joacobsen, K. W., A maximum in the strength of nanocrystalline copper. *Science* **2003,** 301, 1357-1359.

42. Pouzet, J.; Hadouda, H.; Bernede, J. C.; Leny, R., MoS_2 thin films obtained by a new technique: Solid state reaction between the constituents in thin film form. *J. Phys. Chem. Solids* **1996,** 57, (9), 1363-1369.

43. Wilcoxon, J. P.; Williamson, R. L.; Gaughman, R., Optical properties of gold colloids. *J. Chem. Phys.* **1993,** 98, (12), 9933-9950.

44. Gutierrez, M.; Henglein, A., Preparation of colloidal semiconductor solutions of molybdenum (IV) sulfide and tungsten (IV) selenide via sonication. *Ultrasonics* **1989,** 27, 259-261.

45. Jose-Yacaman, M.; Lopez, H.; Santiago, P.; Galvan, D. H.; Garzon, I. L.; Reyes, A., Studies of MoS_2 structures produced by electron irradiation. *Appl. Phys. Lett.* **1996,** 69, (8), 1065-1067.

46. Zelenski, C. M.; Dorhout, P. K., Template synthesis of near-monodisperse microscale nanofibers and nanotubules of MoS_2. *J. Am. Chem. Soc.* **1998,** 120, 734.

47. Nath, M.; Govindaraj, A.; Rao, C. N. R., Simple synthesis of MoS_2 and WS_2 nanotubes. *Adv. Mater.* **2000,** 13, (4), 283-289.

48. Nath, M.; Rao, C. N. R., New metal disulfide nanotubes. *J. Am. Chem. Soc.* **2001,** 123, (20), 4841-4842.

49. Schuffenhauer, C.; Parkinson, B. A.; Jin-Phillipp, N. Y.; Joly-Pottuz, L.; Martin, J. M.; Popovitz-biro, R.; Tenne, R., Synthesis of fullerene-like tantalum disulfide nanoparticles by a gas-phase reaction and laser ablation. *Small* **2005,** 1, (11), 1100-1109.

50. Peters, E. S.; Carmalt, C. J.; Parkin, I. P.; Tocher, D. A., Aerosol-assisted chemical vapor deposition of NbS_2 and TaS_2 thin films from pentakis(dimethylamido)metal complexes and 2-methylpropanethiol. **2005.**

51. An, C. H.; Tang, K. B.; Shen, G. Z.; Wang, C. R.; Yang, Q.; Hai, B.; Quan, Y. T., Growth of belt-like SnS crystals from ethylendiamine solution. *J. Cryst. Growth* **2002,** 244, 333-338.

52. Parenteau, M.; Carlone, C., Influence of temperature and pressure on the electronic transitions in SnS and SnSe semiconductors. *Phys. Rev.* **1990,** B41, 5227.

53. Costa, G. A. A.; Silva, M. C.; Silva, A. C. B.; de Lima, G. M.; Lago, R. M.; Sansiiero, M. T. C., Thermal decomposition of sulfur-contaning organotin molecular precursors to produce phase-pure SnS. *Phys. Chem. Chem. Phys.* **2000,** 2, 5708-5711.

54. Schlecht, S.; Kienle, L., Mild solvothermal synthesis and TEM investigation of unprotected nanoparticles of tin sulfide. *Inorg. Chem.* **2001,** 40, 5719-5721.

55. Greyson, E. C.; Barton, J. E.; Odom, T. W., Tetrahedral zinc blende tin sulfide nano and microcrystals. *Small* **2006,** 2, 368-371.

56. Su, H. L.; Xie, Y.; Xiong, Y. J.; Gao, P.; Quan, Y. T., Preparation and morphology control of rod-like nanocrystalline tin sulfides via a simple ethanol thermal route. *J. Solid State Chem.* **2001,** 161, 190-196.

57. Hu, J. Q.; Bando, Y.; Golberg, D., Self-catalyst growth and optical properties of novel SnO_2 fishbone-like nanoribbons. *Chem. Phys. Lett.* **2003,** 372, 758-762.

58. Yamazoe, N., New approaches for improving semiconductor gas sensors. *Sens. Actuators B* **1991,** 5, 7.

59. Wang, Y. L.; Jiang, X. C.; Xia, Y., A solution-phase, precursor route to polycrystalline SnO_2 nanowires that can be used for gas sensing under ambient conditions. *J. Am. Chem. Soc.* **2003,** 125, 16176-16177.

60. Satishkumar, B. C.; Govindaraj, A. G.; Vogl, E. M.; Basumallick, L.; Rao, C. N. R., Oxide nanotubes prepared using carbon nanotubes as template. *J. Mater. Res.* **1997,** 12, 604-606.

61. Satishkumar, B. C.; Govindaraj, A.; Nath, M.; Rao, C. N. R., Synthesis of metal oxide nanorods using carbon nanotubes as templates. *J. Mater. Chem.* **2000,** 10, 2115-2119.

62. Zheng, W. P.; Zu, R. D.; Zhong, L. W., Nanobelts of semiconducting oxides. *Science* **2001,** 291, 1947-1949.

Chapter 2: Nanostructure Synthesis Techniques

2.1 Background

Different techniques with specific reaction conditions have been employed to prepare different nanostructures (such as nanowires and sphere-like nanoparticles). There are two general approaches for preparing nanoscale materials: top-down and bottom-up. Top-down approaches, such as advanced e-beam lithographic methods, have been applied to nanomaterial production; however, they are usually time consuming and costly. As a result, these procedures are not ideal for large scale use. Bottom-up approaches, on the other hand, provide more control over the reactions, and are therefore more practical. This chapter will focus on the various bottom-up synthetic techniques used to prepare inorganic nanostructures that have been developed over the past decade. These techniques fit into 4 major categories: soft chemical methods, high-temperature methods, methods requiring other energy inputs (such as electron-beam), and template methods. Many of these methods have also been used to prepare carbon nanotubes and fullerene materials.

2.1.1 Soft chemical methods

Soft chemical methods generally refer to processes requiring lower temperature when compare to other synthetic methods. The products (nanostructures) resulted from self-assembly and/or from restricted growth, such as in a micelle.[1-3] The growth process generally involves precipitation of a solid phase from solution.

Hydrothermal (solvothermal) synthesis is one example under the category of soft chemical methods. An autoclave is used as the reaction vessel to reach the reaction temperature, and since it is above the boiling point of the solvent, a high-pressure environment can be created for the reaction. Hydrothermal synthesis relies on the higher solubility of inorganic substances in water (or other solvent) under high-temperature or high-pressure conditions. By reacting precursors and possibly a reagent that serves as regulating the crystal growth in aqueous solutions at high temperature and pressure, nanocrystals with different morphologies, such as nanowires, cubes and sphere-like nanoparticles can be grown.[4-9] The process, however, rarely yields monodisperse nanocrsytals.

Hydrothermal synthesis has been reported for the production of MoS_2 nanotubes.[10] A solution containing ethylene diamine and ammonium thiomolybdate forms an intermediate compound $[(NH_3OH)_{3.9}MoS_{4.8}]$, and produces MoS_2 nanotubes after the hydrothermal treatment. In this specific reaction, ethylene diamine is believed to be the growth-directing agent that supports the formation of nanotubular structures. Another example of a hydrothermal reaction is the synthesis of nickel sulfide nanotubes.[11] They have been prepared by reacting the $Ni(NH_3)_4^{2+}$ complex

with CS_2 in aqueous ammonia under hydrothermal conditions. SnS_2 nanotubes have also been prepared by reacting $SnCl_4$ and thiourea in an autoclave, using anodic aluminum oxide (AAO) to template the nanotubular shape.[12]

Surfactant-assisted colloidal synthesis is another commonly utilized soft-chemical technique that employs self-assembled surfactant structures to control the nucleation and growth of the nanostructures. In one example, the surfactant molecules are dispersed in a non-polar medium where the reaction takes place within reverse micelles. In the reverse micelle, the hydrophilic head groups are directed toward the core of the micelles and the hydrophobic groups are directed outward. By varying the nature and the concentration of the surfactants, a different self-assembled phase of the surfactant can be formed (such as the lamellar phase). As a result, nucleation and growth of the nanoparticles can be controlled. CdSe and CdS nanotubes and nanowires have been prepared by the surfactant-assisted method, as the metal oxide reacts with the selenidizing or sulfidizing agent in the presence of surfactant, such as Triton X.[13] In some cases, surfactants can also act as molecular capping agents that inhibit the growth of specific facets, leading to 1-D growth of the materials.

The synthetic methods described above can be thought to occur through an atom-by-atom addition to an inorganic or organic template or by dissolution and reprecipitation of crystalline materials. An alternative crystal growth route can also occur as the result of a self-assembly-based coarsening mechanism. Self-assembly has been known to generate superlattices of nanoparticles (usually by slow

evaporation of the solvent from a solution of monodisperse nanoparticles). In the case of iron oxyhydrate crystal growth by the solution phase synthesis,[14] short-range interactions between adjacent surfaces can drive aggregation to occur. Another example of self-assembly is the silver nanoparticle chains formation, when ellipsoidal silver nanoparticles self-assembled into chains that were then fused into bundles to hundreds of nanometers in length in solution.[15] Generally speaking, crystal growth via self-assembly is induced by removing pairs of surfaces (coarsening the particles), which reduces the surface energy of the particles.

2.1.2 High-temperature methods

High-temperature methods refer to synthetic methods that require thermal energy for bringing the reactants to their gas phases (for example by heating in a conventional furnace). Some synthetic methods described here can also be employed via other heating techniques, such as with a pulsed laser or electron beam (these methods will be discussed briefly in section *2.1.3*).

One of the most commonly used high-temperature methods is chemical vapor deposition, CVD. This method has been used to produce thin films of metal chalcogenide nanoparticles.[16,17] During CVD, the precursor vapor is introduced into the reactor and is adsorbed onto a substrate held at an elevated temperature. The adsorbed materials can either thermally decompose or react with other vapor phase reactants to form crystals.

Chemical vapor transport (CVT), another high-temperature method, has been employed to produce bulk size materials. It has also been shown to yield

nanomaterials as well. Metal chalcogenide powders are transported from hot to cool zones in an ampoule with a transport agent (such as iodine) and formed into nanotubular structures with the help of catalysts in some cases (such as C_{60}). Uniform WS_2 and MoS_2 nanotubes have been successfully obtained via this method.[18]

Metal chalcogenide nanostructures can also be obtained by heating the respective metal chalcogenide. For example, MoS_2 nanotubes have been synthesized by heating MoS_2 powder covered by Mo foil under H_2S atmosphere.[19]

Sol-gel processes, which are based on inorganic polymerization reactions, are also under the category of high-temperature methods. In the general procedure, an organometallic compound is dissolved in an alcohol. After aging the solution, it is condensed into a gel-form, a compound that can be used for structure directing purposes. After the subsequent thermal treatment, nanowires with high crystallinity can be formed. Silica and TiO_2 nanotubes have been prepared through this method.[20] A spin-off sol-gel approach has recently been employed to generate MgB_2 nanowires.[21] The ethanolic solution of $MgBr_2$ and $NaBH_4$ forms a gel when left open to the atmosphere. By heating the gel under an atmosphere of N_2 and diborane (B_2H_6) gas, MgB_2 nanowires can be prepared.

Pyrolysis of a metal oxide is another popular method that utilizes the high-temperature to produce metal dichalcogenide 1-D nanostructures. Depending on the nature of the oxide materials, oxide nanomaterials can be prepared by either a direct gas phase reaction (such as MoO_3) or by following a vapor-solid (VS) mechanism:[22-24] metal oxides can be obtained by evaporating metal oxide powder or by heating

metal in the presence of water. The resulting metal oxide is then treated in the forming gas (95% N_2 + 5% H_2) to form sub-oxides. Heating in a stream of H_2S then converts the sub-oxide to the sulfide. In the beginning, the outermost metal oxide layers are converted into sulfides. This step is crucial as it inhibits the agglomeration of the oxide nanoparticles. Further sulfidization continues to convert the oxide materials to a trisulfide intermediate. In the last step, annealing of the intermediate forms the metal disulfide nanomaterials. In these reactions, the diffusion of vapors within the particle plays an important role in the formation of the nanostructures: oxygen diffuses out from the particles while hydrogen and hydrogen sulfide diffuses into the particles. The yield in such nanostructures, therefore, depends on the diffusion length of the reactant vapors.[25] Different morphologies of materials are obtained with different heating arrangements. MoS_2 and WS_2 inorganic fullerenes and nanotubes have been prepared with this particular methodology. Other composite nanotubes, such as W-Nb nanotubes, can also be prepared by employing a W-Nb mixed oxide.[26]

A more direct methodology, derived from the above oxide to sulfide reactions, employs metal trisulfide precursors to yield metal dichalcogenide 1-D nanostructures. During the reaction, the trisulfide is first reduced by the flux of H_2 and forms a nucleation site. At the decomposition temperature of the trisulfide, sulfur is lost and forms disulfide layers at the periphery of the trisulfide particles. This inside-out growth begins as the amorphous trisulfide core decomposes to the crystalline

disulfide, resulting in the growth of nanotubes. MoS_2, WS_2,[27] NbS_2,[28] and HfS_2 [29] nanotubes have all been synthesized using this approach.

Thermal decomposition of a single source precursor has been employed in synthesizing various nanomaterials. For example, MoS_2, $MoSe_2$, and WSe_2 nanotubes and nanorods have all been prepared by thermal decomposition of ammonium salt precursors, $(NH_4)_2MX_4$, (X = S, Se; M = Mo, W) in H_2. Mixed inorganic nanomaterials can also be produced, based on this approach. For example, $Mo_{1-x}W_xS_2$ nanotubes can be prepared by decomposing solid solutions of ammonium thiometallates, $(NH_4)_2Mo_{1-x}W_xS_4$, with varying Mo:W ratios.

2.1.3 Methods requiring other energy sources

Generally most methods using high energy input are far from equilibrium, as drastic synthetic conditions are employed. Laser ablation,[30] arc discharge,[31-33] sonochemistry[34] are the examples that have all been used for WS_2 nanotube and fullerene-like structure synthesis. Electron-beam irradiation has been employed for generating $CdCl_2$ inorganic fullerenes,[35] and $NbSe_2$[36] and WSe_2 nanotubes.[37] Microwave irradiation has been applied to synthesize MoS_2 fullerene-like materials and NbS_2 nanotubes:[38-40] a metal precursor (such as $Mo(CO)_6$) powder was vaporized and then mixed with a heated H_2S/Ar atmosphere, under the microwave irradiation, to generate fullerene-like structures.[38] Another synthetic route to obtain LMC nanostructures is using scanning tunneling microscopy (STM): MoS_2 nanostructures were formed from amorphous MoS_3 materials by passing a short electrical pulse through the STM tip situated in close proximity to MoS_3 nanoparticles.[41] The idea

was to abstract sulfur from the nanoparticles and recrystallize a few closed MoS_2 layers that encapsulate the MoS_3 core of the nanoparticles.

2.1.4 Templated methods

Template methods are one of the most commonly used routes for 1-D nanostructure preparation. This method uses a generic deposition strategy and is usually employed in tandem with other synthetic methods, such as pyrolysis. There are different kinds of templates, hard templates (such as porous nanoscale membranes), sacrificial templates, and soft templates (such as the reverse micelles), however they all serve the purpose of restraining the shape and dimension of the formed nanostructures. Here, the discussion is focused on the hard template and sacrificial template method, since the soft template method is also categorized as a soft chemical method (Section 2.1.1).

One of the earlier templating studies by Zelenski, *et al.*, involved in thermal decomposition of meal salts within the pores of an anodic aluminum oxide (AAO) membrane.[42] The porous host is first filled with the precursor solution, and is heated in the furnace to yield 1-D nanostructures. If high quality hard templates are used, the obtained 1-D nanostructures can be made with well-controlled diameters.

More advanced templating methods to produce 1-D nanostructures are known as sacrificial template methods. 1-D nanostructures are directly used as the template material and allowed to deposit or react with suitable chemicals to transform them into other substance while restraining the 1-D morphology. For example, carbon nanotubes have been used as an effective template for preparing double or multi-

walled WS_2 nanotubes. The carbon nanotubes can also be coated with metal oxide that is then converted to sulfide nanotubes by thermal treating with a H_2S, H_2 and N_2 atomsphere.[43,44]

In the following sections, three specific preparation methods for nanomaterials (laser ablation, solution-phase synthesis, and pyrolysis/thermal decomposition) will be discussed in detail, as they are used in this dissertation.

2.2 Laser ablation

The laser ablation (LA) project in the Parkinson group is based on previous work (with MoS_2) by the Heben group at the National Renewable Energy Laboratory (NREL). Recognizing that different layered transition metal dichalcogenides differ in their tendency to form fullerene-like structures during the laser ablation, a set of reaction parameters were designed to create TaS_2 nanoparticles. As experiments proceeded, TaS_2 nanoplatelets were generated. Dependent on experimental conditions, TaS_2 tends to form nanoplatelets (as will be described later in Chapter 3). The basic setup of the experiment is shown as Figure 2.1. Other LA-related experiments and results involving other materials (such as ReS_2), media (such as in a liquid), or the power source (such as a femtosecond pulsed laser) will be discussed in Chapter 4.

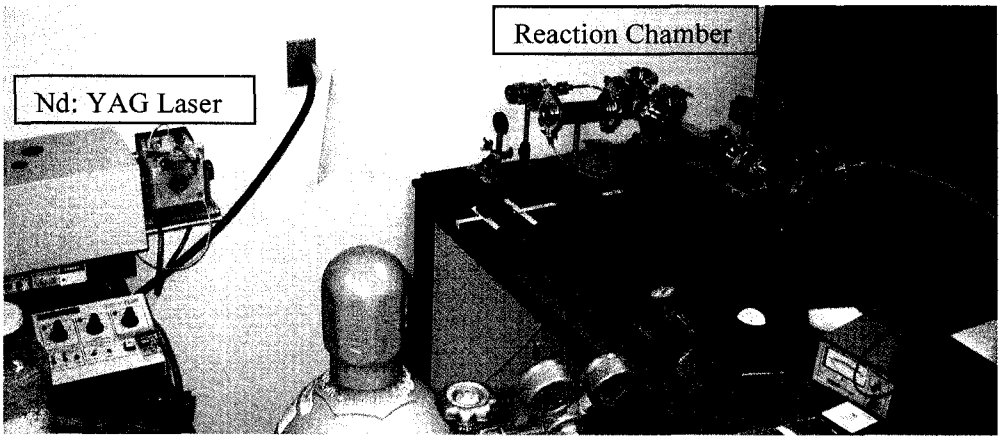

Figure 2.1 (a) Reaction chamber in the Parkinson group laboratory

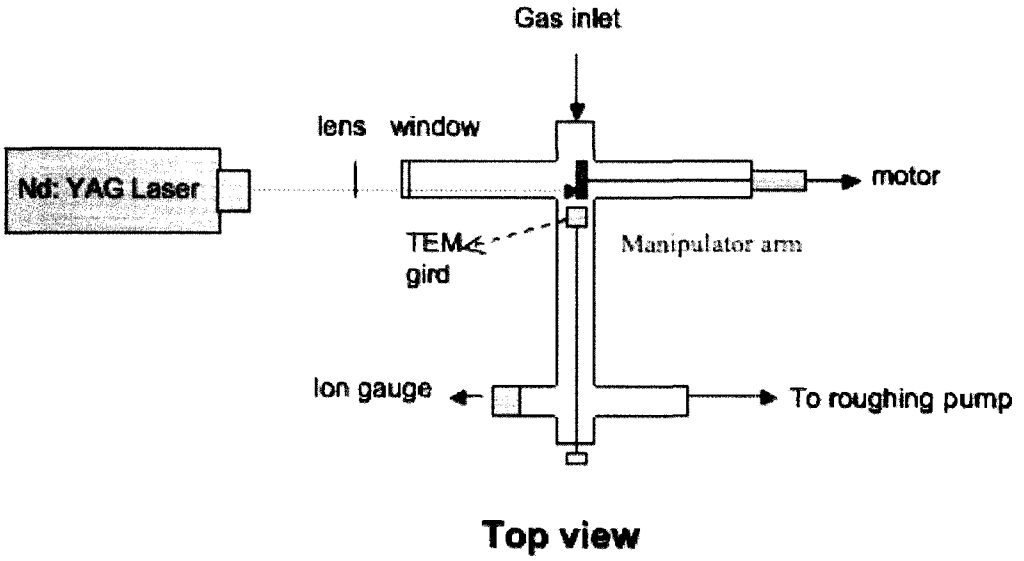

Figure 2.1 (b) Schematic of the reaction chamber.

2.2.1: Applications

Laser ablation can be applied to laser surgery,[45] chemical analysis,[46] surface oxide removal,[47] thin film production,[48] and nanoparticle synthesis.[49] Laser ablation was employed in the initial production of C_{60}[50] and the formation of the IF-MoS_2

octahedra.[51] Since then, LA has been successfully applied to synthesis of carbon nanotubes and fullerenes, inorganic fullerenes, and cluster assembled materials.[35] LA produces the highest quality carbon nanotubes.

2.2.2: General mechanisms

The exact mechanism of laser ablation is not completely understood. It is a complex process involving absorption of laser energy, radiation transport, evaporation of the ablated materials, ionization, condensation, and recombination. The overall process is governed by several experimental parameters, depending strongly on the irradiation conditions (such as the laser fluence, wavelength, and pulse duration), as well as the ablated medium. For laser ablation under the inert gas, the nature and pressure of the inert gas are also important to the ablation process. When nanosecond pulsed laser is utilized as the laser source, the general mechanisms (in vacuum) can be described as follows:

2.2.2.1 Material removal

The material to be ablated, if in powder form, is usually pressed into a target pellet. The laser beam then is focused onto the target surface. As the laser impinges on the target, the temperature at the target surface rapidly rises leading to melting of the material. As the laser power exceeds the ablation threshold, evaporation (such as elemental fractionation, non-stoichiometric ablation) and ionization of the target material then occurs. As a result, the material is being removed from the surface of the target.

2.2.2.2 Plasma formation

The plasma plume is formed using high laser power density: the interaction between the laser beam and the evaporated target material leads to the plume. Within the plasma plume, the temperature can reach thousands of degrees.[52] The high temperature near the target produces a high pressure leading to a rapid expansion. Pressure can be very high within the plume, and thus the mean free path is short. The plasma plume continues expanding via the strong laser beam-plasma plume interactions until the termination of the laser beam (pulse).

2.2.2.3 Plasma cooling and the formation of nanoparticles

Upon termination of the laser pulse, the thermal energy from the plasma plume rapidly converts into kinetic energy; consequently an adiabatic expansion of the plasma occurs. The temperature drops quickly (within 100 ns), but then cools more slowly as the result of recombination of the ions.[53] Collisions and condensation occurring during the adiabatic expansion lead to the formation of nanosize particles. Microsize materials also can be found as side-products, however they are usually caused by direct ejection from the target from a shockwave or thermal stress.

2.2.3: Mechanisms under inert gas

The previous section described the general propagation mechanism of laser ablation in a vacuum, when the plasma undergoes free-expansion. When laser ablation takes place under inert gas conditions however, collisional interaction between the plasma plume and inert gas molecules becomes significant. The resulting plasma plume, therefore, is characterized by interactions of the laser beam,

plasma plume, and the ambient gas species. A plume boundary (i.e. the confinement), along with a slow and fast moving component of the plasma plume can be observed.[53] The kinetic energy transfers from the laser plasma to the gas molecules, slowing down the adiabatic plasma expansion. The ablated materials push against the gas molecules until the plasma and gas pressure equilibrate. Since cluster/nanoparticle formation is directly related to the plume's characteristics, the inert gas pressure used during LA becomes one major parameter affecting the size and structure of the resulting nanoparticles.

2.2.4: General mechanisms in liquid

The mechanism of laser ablation in liquid can be very different from the normal laser-solid interaction in air or inert gas. The reaction conditions are different depending on the position of the ablated target: it can either be dispersed in the liquid, or positioned as a thin film/pellet. In general, the absorption of the laser beam generates temperatures as high as several thousands of degrees, along with strong light emission. The condition is therefore similar to the plasma discharge, and sonochemistry. Chapter 4 will describe several laser ablation experiments in liquid.

2.2.5: Laser ablation via specific pulse length laser (pico-second or femto-second pulsed laser)

The above mentioned LA mechanisms are applicable to nanosecond (ns) pulsed lasers. For picosecond (ps) and femtosecond (fs) pulsed lasers, the energy absorption mechanism is different from the ns pulsed laser as the electron energy is not able to turn into heat instantaneously.[54] The plasma plume formation occurred

after the termination of the laser pulse, and therefore, the plasma plume does not directly interact with the laser pulse. The non-thermal melting of the ablated target is more significant which results in a cleaner ablation. Again, Chapter 4 will describe several experiments using a fs pulsed laser for ablation.

2.3 Solution-phase synthesis

Solution-phase synthesis is also employed to prepare nanostructures using a single source precursor. Colloidal solution reactions, one example of solution-phase synthetic methods, control the particle shapes/structures (such as nanowires, nanorods, nanoplatelets, pyramid, etc). In some solution-phase reactions, surfactants act as molecular capping agents since they can control the growth kinetics of the nanocrystal by preferentially absorbing to some specific facets of the crystal and as a result, inhibit the growth of those facets, leading to a 1-D growth of the materials.

2.3.1 Crystal growth mechanism in solution

Crystal growth typically involves two steps, nucleation and growth. In the case of a solution-phase reaction, there are three different kinds of nucleation: homogeneous nucleation, heterogeneous nucleation, and secondary nucleation. Homogeneous nucleation occurs when solute molecules combine to produce nuclei. Heterogeneous nucleation occurs when more than one phase of precursor produce nuclei. For example, when soluble species deposit on a solid surface. Secondary nucleation refers to the nucleation starting from aggregation, as the unstable nuclei collide to form a bigger particle. In all three nucleation types, supersaturation of the

solution is necessary. This can be achieved by either directly dissolving the solute at an elevated temperature and cooling to low temperature; or by adding the reactants during the reaction to produce a supersaturated solution.

The nuclei begin to grow by molecular additions that decrease the overall free energy of the particles. When the concentration of solute drops below certain level, nucleation is terminated but particle growth continues. To form a monodisperse sample, it is necessary to control both the nucleation and the growth process. A relatively narrow size distribution of particles can be obtained with a short nucleation period followed by slower growth step on the existing nuclei. One approach to achieve this is to rapidly add reactants into the reaction containing hot solvent. With sufficient solution temperature, reactants undergo reaction (such as decomposition) in a short period of time and lead to the supersaturation. After the short nucleation period, the growth of the crystallite continues as long as the consumption of the reactants by the growth of the particles does not exceed the rate of the precursor addition. Smaller crystals usually grow faster than the larger crystals, and therefore, the crystals can become more uniform over time from the result of size focusing.[55]

2.4 Thermal decomposition/pyrolysis and physical vapor deposition

2.4.1 Thermal decomposition

Pyrolysis via thermal decomposition is another useful synthesis technique for nanostructure synthesis. The basic furnace setup for this synthetic route in this dissertation work is shown in Figure 2.2.

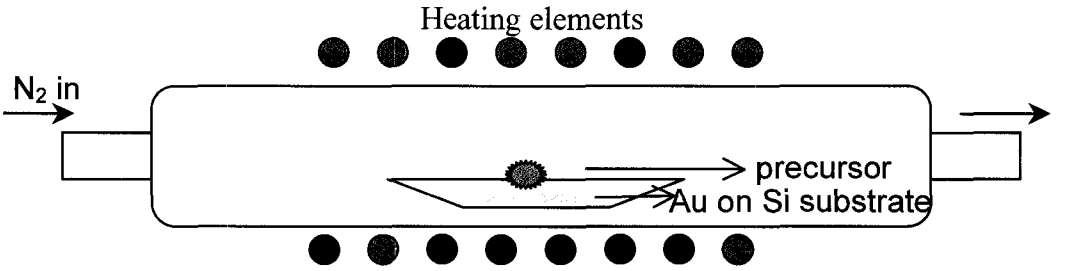

Figure 2.2 Schematic of the furnace setup

Thermal decomposition has been employed in synthesizing various LMC nanomaterials, such as MoS_2, $MoSe_2$, and WSe_2 nanotubes and nanorods, by undergoing the thermal decomposition of precursors ammonium salt, $(NH_4)_2MX_4$, (X = S, Se; M = Mo, W) in H_2. The general reaction can be written as:

$(NH_4)_2MX_4 + H_2 \rightarrow MX_2 + 2H_2X + 2NH_3$ (X = S, Se; M = Mo, W) [Equation 2.1]

Based on this strategy, other inorganic composite nanomaterials can be produced. For example, solid solutions of ammonium thiometallates, $(NH_4)_2Mo_{1-x}W_xS_4$, with varying Mo:W ratios have been used as the precursors to generate $Mo_{1-x}W_xS_2$ nanotubes under inert gas flow.[56]

Single source precursors are commonly employed in thermal decomposition. For example, cage-ring structures of the organotin precursors,[57] dithiocarbamate,[58] thiadiazole,[59] and phenylated ring system[60, 61] have all been employed for preparation of metal sulfide materials. Since no additional reactant is required throughout the reaction, better control of the synthetic process can be achieved. Furthermore, in most cases of single-source precursors, the reaction temperatures required during the

synthetic process (for example thermal decomposition) are relatively low when compared to conventional methods. Thermal decomposition of the single source precursor, therefore, provides a facile route for material synthesis.

2.4.2 Physical vapor deposition (PVD)

Physical vapor deposition (PVD) is also a relevant technique. In PVD, a volatile precursor source is evaporated or sublimed. The precursor vapor is then transported and reacted, resulting in the deposition of nanostructures in the cooler zone of the furnace or on a substrate. For example, NbS_2 nanoparticles have been prepared by heating $NbCl_5$ precursor.[62] The $NbCl_5$ vapor is carried into the reactor by an inert gas. A mixture of gas consisting of H_2, N_2, and H_2S reacts with $NbCl_5$ vapor at 450 °C and yields $Nb_{1+X}S_2$ nanoparticles. Further annealing at higher temperature (550 °C) produces NbS_2 nanoparticles. Nanowires of metal chalcogenides, such as ZnS, ZnSe, CdS and CdSe, have also been prepared by this method with metal catalysts deposited on the substrate.[63-65] The growth mechanism of these nanowires is believed to be the Vapor-liquid-solid (VLS) mechanism. The following sections will cover two growth mechanisms of one-dimensional structures: VLS and Vapor-Solid (VS) mechanisms.

2.4.3 Vapor-liquid-solid (VLS) mechanism

Proposed by Wagner in 1960s, the vapor-liquid-solid mechanism (VLS) is one of the most well-accepted growth mechanisms in nanomaterials synthesis.[66] VLS growth has been widely utilized to produce 1-D nanostructures of pure and doped inorganic materials, for example elemental semiconductor (Si, Ge),[67-69] III-V

materials (GaN, GaAs, GaP, InP, InAs),[70-76] and II-VI materials (ZnS, ZnSe, CdS, CdSe)[63-65] and a variety of metal oxide materials.[77-79] VLS utilizes gas-phase reactions that can take place in a furnace. Other techniques, such as laser ablation, molecular beam epitaxy, and sputtering, have also been employed to exploit this preparation mechanism.

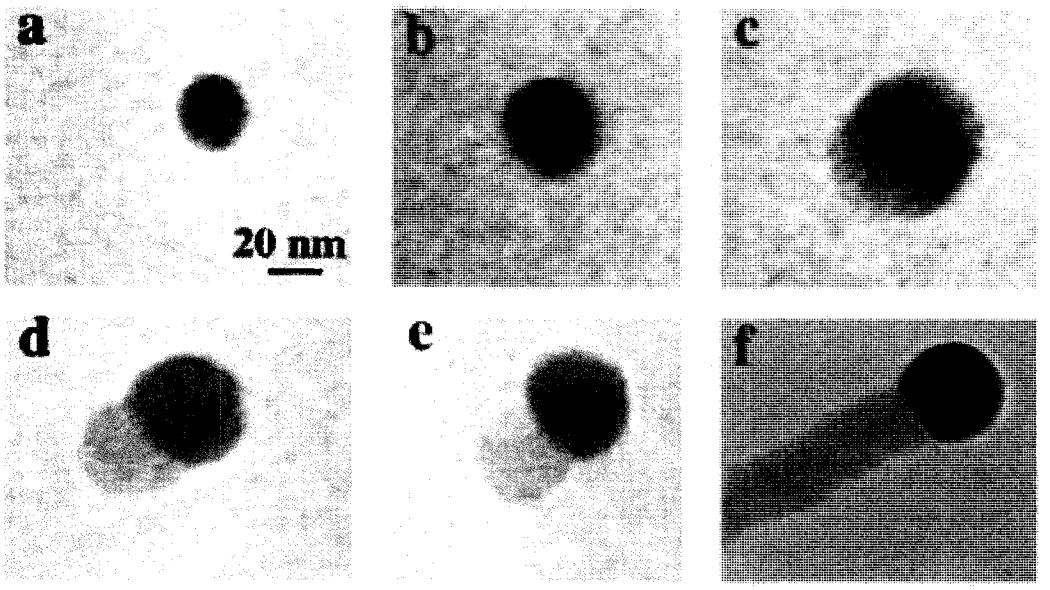

Figure 2.3 In-situ TEM images reveal the Ge nanowire growth via VLS method (from a-f), with Au as the metal catalyst.[80]

The VLS mechanism depends upon a liquid surface (a template) for deposition and alloying by melting metal seeds in the vapor of other metal or metal precursor (to form eutectic compounds). As the liquid alloy becomes supersaturated, nanowires can be grown by precipitation at the solid-liquid interface. Figure 2.3 shows the in-situ TEM images taken during the VLS growth process.[80] During the growth, the size of the metal seed determines the diameter of the resulting nanowire,

and usually remains unchanged during the wire-growth process. In some cases, however, the seeds can be consumed by the wire, which can lead to both the contamination of nanowire and a narrowing of the wire as it grows. In other cases, interfacial thermal expansion differences can dislodge the seeds from the wires during the cooling process. Nevertheless, the length of nanowires usually increases with the growth time. Besides conventional nanowires, longitudinal heterostructured nanowires can also be grown following the VLS mechanism [Figure 2.4].[81] The single-crystalline nanowires consisting of Si/SiGe superlattice structures have been grown by the VLS growth system as Si and Ge vapor sources are independently controlled and alternately delivered.[82] VLS provides the desired control to produce well-defined and coherent interfaces of the heterostructured nanowires.

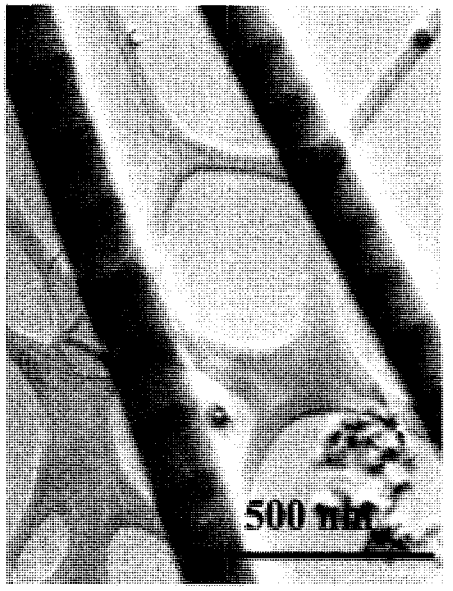

Figure 2.4 TEM image of Si/SiGe superlattice nanowires.[81]

2.4.4 Vapor-solid (VS) mechanism

A similar mechanism to VLS, the vapor-solid (VS) mechanism has also been proposed for 1-D nanocrystal growth. The exact growth mechanism is still not yet completely elucidated, however, it is generally believed that both nucleation and growth of the 1-D structures can be accomplished by the preferential reactivity and binding of gas phase reactants to the specific crystal faces or specific defects (such as screw dislocations). One distinct difference of VS from VLS mechanism is the absence of foreign materials from the tips of the as-grown nanowires. VS growth, instead of forming eutectic liquid droplets, is related to the diffusion, attachment, and adsorption of the reacting atomic species and clusters formed in the growth process.[83-85] It is believed that the atoms are impinging onto the nucleation surface and are temporarily adsorbed, following with diffusion along the lateral surface to the tips. The competition in growth rate among different crystallographic planes results the anisotropic 1-D growth. Many metal oxide nanomaterials, such as ZnO and CdO nanoribbons, have been prepared by evaporating commercial metal oxide powders at elevated temperatures following the VS mechansim.[86]

Reference

1. Chakraborty, I.; Moulik, S. P., Preparation of CoS_2 nanoparticles in aqueous micellar media of anionic surfactants: AOT and SDS. *J. Surf. Sci. Tech.* **2005,** 21, (3-4), 195-204.

2. Merkoci, A.; Marin, S.; Castaneda, M. T.; Pumera, M.; Ros, J.; Alegret, S., Crystal and electrochemical properties of water dispersed CdS nanocrystals obtained via reverse micelles and arrested precipitation. *Nanotechnology* **2006,** 17, (10), 2553-2559.

3. Yu, X. L.; Cao, C. B.; Zhu, H. S., Synthesis and photoluminescence properties of Bi_2S_3 nanowires via surfactant micelle-template inducing reaction. *Solid State Commun.* **2005,** 134, (4), 239-243.

4. Xie, R. C.; Shang, J. K., Morphological control in solvothermal synthesis of titanium oxide. *J. Mater. Sci.* **2007,** 42, (16), 6583-6589.

5. Jiang, C. L.; Zhang, W. Q.; Zou, C. F.; Yu, W. C.; Qian, Y. T., Hydrothermal synthesis and characterization of ZnS microspheres and hollow nanospheres. *Mater. Chem. Phys.* **2007,** 103, (1), 24-27.

6. Roy, P.; Srivastava, S. K., Hydrothermal growth of CuS nanowires from Cu-dithiooxamide, a novel single-source precursor. *Crystal Growth & Design* **2006,** 6, (8), 1921-1926.

7. Yue, G. H.; Yan, P. X.; Yan, D.; Fan, X. Y.; Wang, M. X.; Qu, D. M.; Liu, J. Z., Hydrothermal synthesis of single-crystal ZnS nanowires. *Appl. Phys. A* **2006,** 84, (4), 409-412.

8. Wang, Q. Q.; Xu, G.; Han, G. R., Solvothermal synthesis and characterization of uniform CdS nanowires in high yield. *J. Solid State Chem.* **2005,** 178, (9), 2680-2685.

9. Zhang, H.; Ji, Y. J.; Ma, X. Y.; Xu, J.; Yang, D., Long Bi_2S_3 nanowires prepared by a simple hydrothermal method. *Nanotechnology* **2003,** 14, (9), 974-977.

10. Afanasiev, P.; Geantet, C.; Bezverkhyy, I.; Lacroix, M., Highly active (Co)MoS_2/Al_2O_3 hydrodesulfurization catalysts prepared in aqueous solution. *J. Catal.* **2001,** 204, (2), 495-497.

11. Jiang, X. c.; Xie, Y.; Zhu, L.; He, W.; Qian, Y., Synthesis of novel nickel sulfide layer-rolled structures. *Adv. Mater.* **2001,** 13, 1278-1281.

12. Chen, D.; Shen, G. Z.; Tang, K. B.; Liu, Y. K.; Qian, Y. T., Aligned SnS_2 nanotubes fabricated via a template-assisted solvent-relief process. *Appl. Phys. A* **2003,** 77, 747-749.

13. Rao, C. N. R.; Govindaraj, A. G.; Deepak, F. L.; Gunari, N. A.; Nath, M., Surfactant-assisted synthesis of semiconductor nanotubes and nanowires. *Appl. Phys. Lett.* **2001,** 78, (13), 1853-1855.

14. Banfield, J. F.; Welch, S. A.; Zhang, H. Z.; Thomsen Ebert, T.; Lee Penn, R., Aggregation-based crystal growth and microstructure development in natural iron oxyhydroxide biomineralization products. *Science* **2000,** 289, 751-754.

15. Korgel, B. A.; Fitzmaurice, D., Self-assembly of silver nanocrystals into two-dimensional nanowire arrays. *Adv. Mater.* **1998,** 10, (9), 661-665.

16. Walters, D. A. e. a., In-plane-aligned membranes of carbon nanotubes. *Chem. Phys. Lett.* **2001,** 338, 14-20.

17. Delzeit, L., Growth of carbon nanotubes by thermal and plasma chemical vapor deposition processes and applications in microscopy. *Nanotechnology* **2002,** 13, 280-284.

18. Remskar, M.; Skarba, Z.; Regula, M.; Ballif, C.; Sanjines, R.; Levy, F., New crystal structures of WS_2. Microtubes, ribbons, and ropes. . *Adv. Mater.* **1998,** 10, (3), 246-249.

19. Hsu, W. K.; Chang, B. H.; Zhu, Y. Q.; Han, W. Q.; Terrones, H.; Terrones, M.; Grobert, N.; Cheetham, A. K.; Kroto, H. W.; Walton, D. R. M., An alternative route to molybdenum disulfide nanotubes. *J. Am. Chem. Soc* **2000,** 122, 10155-10158.

20. Kasuga, T.; Hiramatsu, M.; Hason, A.; Sekino, T.; Niihara, K., Formation of titanium oxide nanotube. *Langmuir* **1998,** 14, 3160-3163.

21. Nath, M.; Parkinson, B. A., A simple sol-gel synthesis of superconducting MgB_2 nanowires. *Adv. Mater.* **2006,** 18, 1865-1868.

22. Tenne, R.; Margulis, L.; Genut, M.; Hodes, G., Polyhedral and cylindrical structures of tungsten disulfide. *Nature* **1992,** 360, 444-446.

23. Margulis, L.; Salitra, G.; Tenne, R., Nested fullerene-like structures. *Nature* **1993,** 365, 113-114.

24. Feldman, Y.; Wassemran, E.; Srolovitch, D. J.; Tenne, R., High-rate, gas-phase growth of MoS_2 nested inorganic fullerenes and nanotubes. *Science* **1995,** 267, 222-225.

25. Rothschild, A.; Sloan, J., Growth of WS_2 Nanotubes Phases. *J. Am. Chem. Soc.* **2000,** 122, (21), 5169-5179.

26. Zhu, Y. Q.; Hsu, W. K.; Firth, S.; Terrones, M.; Clark, R. J. H.; Kroto, H. W.; Walton, D. R. M., Nb-doped WS_2 nanotubes. *Chem. Phys. Lett.* **2001,** 342, (1,2), 15-21.

27. Nath, M.; Govindaraj, A.; Rao, C. N. R., Simple synthesis of MoS_2 and WS_2 nanotubes. . *Adv. Mater.* **2001,** 13, (4), 283-286.

28. Nath, M.; Rao, C. N. R., New metal disulfide nanotubes. *J. Am. Chem. Soc.* **2001,** 123, (20), 4841-4842.

29. Nath, M.; Rao, C. N. R., Nanotubes of group 4 metal disulfides. *Angew. Chem. Int. Ed.* **2002,** 41, (18), 3451-3454.

30. Thess, A., Crystalline ropes of metallic carbon nanotubes. *Science* **1996,** 273, 483.

31. Bethune, D. S., Cobalt-catalysed growth of carbon nanotubes with single-atomic-layer walls. *Nature* **1993,** 363, 605.

32. Journet, C., Large-scale production of single-walled carbon nanotubes by the electric-arc techniques. *Nature* **1997,** 388, 756.

33. Tenne, R.; Homyonfer, M.; Feldman, Y., Nanoparticles of layered compounds with hollow cage structures (inorganic fullerene-like structures). *Chem. Mater.* **1998,** 10, 3225-3238.

34. Mackie, E. B.; Galvan, D. Z.; Adem, E.; Tapapatra, S.; Yang, G.; Migone, A. D., Production of WS_2 nanotubes by an activation method. *Adv. Mater.* **2000,** 12, (7), 495-498.

35. Popovitz-biro, R.; Twersky, A.; Rosenfeld Hachoen, Y.; Tenne, R., Nanoparticles of $CdCl_2$ with closed cage structures. . *Isr, J. Chem.* **2001,** 41, (1), 7-14.

36. Galvan, D. H.; Kim, J.-H.; Maple, M. B.; Avalos-Borja, M.; Adem, E., Formation of $NbSe_2$ nanotubes by electron irradiation. *Fullerene Sci. and Technol.* **2000,** 8, (3), 143-151.

37. Galvan, D. H.; Rangel, R.; Adem, E., WSe_2 nanotubes: their formulation by electron, irradiation. *Fullerene Sci. and Technol.* **2000,** 8, (1&2), 9-15.

38. Vollath, D.; Szabo, D. V., Synthesis of nanocrystalline MoS_2 and WS_2 in a microwave plasma. *Mater. Lett.* **1998,** 35, (3,4), 236-244.

39. Vollath, D.; Szabo, D. V., Nanoparticles from compounds with layered structures. *Acta mater.* **2000,** 48, 953-967.

40. Remskar, M.; Mrzel, A.; Jesih, A.; Levy, F., Metal-alloyed NbS_2 nanotubes synthesized by the self-assembly of nanoparticles. . *Adv. Mater.* **2002,** 14, (9), 680-684.

41. Homyonfer, M.; Mastai, Y.; Hershfinkel, M.; Volterra, V.; Hutchison, J. L.; Tenne, R., Scanning tunneling microscope induced crystallization of fullerene-like MoS_2. *J. Am. Chem. Soc* **1996,** 118, (33), 7804-7808.

42. Zelenski, C. M.; Dorhout, P. K., Template synthesis of near-monodisperse microscale nanofibers and nanotubules of MoS_2. *J. Am. Chem. Soc.* **1998,** 120, 734.

43. Zhu, J.; Fan, S., Nanostructure of GaN and SiC nanowires based on carbon nanotubes. *J. Mater. Res.* **1999,** 14, (4), 1175-1177.

44. Zhu, Y. Q.; Hsu, W. K.; Kroto, H. W.; Walton, D. R. M., Carbon nanotube template promoted growth of NbS_2 nanotubes/nanorods. *Chem. Comm.* **2001**, 2184-2185.

45. Niemz, M. H., Laser-tissue interactions: fundamentals and applications. *springer-Verlag, Berlin Heidelberhg* **1996**.

46. Vertes, A.; Gijbels, R.; Adams, F., *Laser ionization mass analysis*. Wiley: New York, 1993

47. Kearns, A.; Fischer, C.; Watkins, K. G.; Glasmacher, M.; Kheyrandish, H.; Brown, A.; Steen, W. M.; Beahan, P., Laser removal of oxides from a copper substrate using Q-switched Nd:YAG radiation at 1064 nm, 532 nm and 266 nm. *Appl. Surf. Sci.* **1998,** 127-129, 773-780.

48. Hakola, A.; Heczko, O.; Jaakkola, A.; Kajava, T.; Ullakko, K., Ni-Mn-Ga films on Si, GaAs, and Ni-Mn-Ga single crystals by pulsed laser deposition. *Appl. Surf. Sci.* **2004,** 238, 155-158.

49. Schuffenhauer, C.; Parkinson, B. A.; Neng, Y. J.; Joly, L.; Martin, J. M.; Popvitz, R.; Tenne, R., Synthesis of fullerene-like tantalum disulfide nanopoarticles by a gas-phase reaction and laser ablation. *Small* **2005,** 1, 1-11.

50. Kroto, H. W.; Heath, J. R.; O'Brien, S. C.; Curl, R. F.; Smalley, R. E., C60: buckminsterfullerene. *Nature* **1985,** 318, 162-163.

51. Parilla, P. A.; Dillon, A. C.; Jones, J. G.; Riker, G.; Schulz, D. L.; Ginley, G. S.; Heben, M. J., The first true inorganic fullerenes? *Nature* **1999,** 397, 114.

52. Zhigilei, L. V.; Kodali, P. B. S.; Garrison, B. J., A microscopic view of laser ablation. *J. Phys. Chem. B* **1998,** 102, 2845-2853.

53. Wood, R. F.; Leboeuf, J. N.; Che, K. R.; Geohegan, D. B.; Puretzky, A. A., Dynamics of plume propagation, splitting, and nanoparticle formation during pulsed-laser ablation. *Appl. Surf. Sci.* **1998,** 127-129, 151-158.

54. Bogaerts, A.; Y., C. Z.; Gijbels, R.; Vertes, A., Laser ablation for analystical sampling: what can we learn from modeling? *Spectrochimica Acta Part B* **2003,** 58, 1967-1893.

55. Burda, C.; Chen, X. B.; Narayanan, R.; El-Sayed, M. A., Chemistry and properties of nanocrystals of different shapes. *Chem. Rev.* **2005,** 105, 1025-1102.

56. Nath, M.; Mukhopadhyay, K.; Rao, C. N. R., $Mo_{1-x}W_xS_2$ nanotubes and related structures. *Chem. Phys. Lett.* **2002,** 352, (3,4), 163-168.

57. Costa, G. A. A.; Silva, M. C.; Silva, A. C. B.; de Lima, G. M.; Lago, R. M.; Sansiiero, M. T. C., Thermal decomposition of sulfur-containing organotin molecular precursors to produce phase-pure SnS. *Phys. Chem. Chem. Phys.* **2000,** 2, 5708-5711.

58. Menezes, D. C.; de Lima, G. M.; Porto, A. O.; Donnici, C. L.; Arisson, J. D.; Doriguetto, A. C.; Ellena, J., Synthesis, characterization and thermal decomposition of tin(IV) diethiocarbamate derivative-single source precursors for tin sulfide powders. *Polydehdron* **2004,** 23, 2103-2109.

59. M. Nath, S., Di- and triorganotin (IV) derivatives of 5-amino-3H-1,3,4-thiadiazole-2-thione as precursors or SnS/SnO_2: thermal studies and related kinetic parameters. *Mater. Res. Bull.* **2006,** 41, 78-91.

60. Bahr, S.; Boudjouk, P.; McCarthy, G. J., Tin-sulfur and tin-selenium phenylated ring systems as organometallic precursors to tin sulfide and tin selenide. *Chem. Mater.* **1992,** 4, 383-388.

61. Boudjouk, P.; Seidler, D. J.; Bahr, S.; McCarthy, G. J., Bis(tripheyltin) chalcogenides as convenient precursors to phase-pure binary semiconductors. *Chem. Mater.* **1994,** 6, 2106-2112.

62. Schuffenhauer, C.; Popovitz-biro, R.; Tenne, R., Synthesis of NbS_2 nanoparticles with (nested) fullerene-like structure (IF). . *J. Mater. Chem.* **2002,** 12, (5), 1587-1591.

63. Lopez-Lopez, M.; Guillen-Cervantes, A.; Rivera-Alvarez, Z.; Hernandez-Calderon, I., Hillock formation during the molecular beam epitaxial growth of ZnSe on GaAs substrates. *J. Cryst. Growth* **1998,** 193, 528-534.

64. Wang, Y.; Meng, G.; Zhang, L.; Liang, C.; Zhang, J., Catalytic growth of large-scale single-crystal CdS nanowires by physical evaporation and their photoluminescence. *Chem. Mater.* **2002,** 14, 1773-1777.

65. Wang, Y.; Zhang, L.; Liang, C.; Wang, G.; Peng, X., Catalytic growth and photoluminescence properties or semiconductor single-crystal ZnS nanowires. *Chem. Phys. Lett.* **2002,** 357, 314-318.

66. Wagner, R. S., Defects in Silicon Crystals Grown by the VLS Technique. *J. Appl. Phys.* **1967,** 38, (4), 1554-1560.

67. Westwater, J.; P., G. D.; Tomiya, S.; Usui, S.; Ruda, H., Growth of silicon nanowires via gold/silane vapor-liquid-solid reaction. *J. Vac. Sci. Technol. B* **1997,** 15, 554-557.

68. Wu, Y.; Yang, P., Germanium nanowire growth via simple vapor transport. *Chem. Mater.* **2000,** 12, 605-607.

69. Zhang, Y. J.; Zhang, Q.; Wang, N. L.; J., Y. Y.; Zhou, H. H.; Zhu, J., Synthesis of thin Si whiskers (nanowires) using SiCl4. *J. Cryst. Growth* **2001,** 226, 185-191.

70. Yazawa, M.; Koguchi, M.; Muto, A.; Hiruma, K., Semiconductor nanowhiskers. *Adv. Mater.* **1993,** 5, 577-580.

71. Shimada, T.; Hiruma, K.; Shirai, M.; Yazawa, M.; Haraguchi, K., Size, position and direction control on GaAs and InAs nanowhisker growth. *Superlattice Microstr.* **1998,** 24, 453-458.

72. Gudiksen, M. S.; Lieber, C. M., Diameter-selective synthesis of semiconductor nanowires. *J. Am. Chem. Soc* **2000,** 122, 8801-8802.

73. Shi, W. S.; Zheng, Y. F.; Wang, N.; Lee, C. S.; Lee, S. T., Synthesis and microstructure of gallium phosphide nanowires. *J. Vac. Sci. Technol. B* **2001,** 19, 1115-1118.

74. He, M.; Zhou, P.; Mohammad, S. N.; Harris, G. L.; Halpern, J. B., Growth of GaN nanowires by direct reaction of Ga with NH3. *J. Cryst. Growth* **2001,** 231, 357-365.

75. Chen, C. C.; Yeh, C. C.; Chen, C. H.; Yu, M. Y.; Liu, H. L., Catalytic growth and characterization of gallium nitride nanowires. *J. Am. Chem. Soc* **2001,** 123, 2791-2798.

76. Zhong, Z.; Qian, F.; Wang, D.; Lieber, C. M., Synthesis of p-type gallium nitride nanowires for electronic and photonic nanodevices. *Nano Lett.* **2003,** 3, 343-346.

77. Zhang, J.; Jiang, F. H.; Yang, Y. D.; Li, J. P., Molten Pb as a catalyst for large-scale growth of highly aligned silicon oxide nanowires. *J. Cryst. Growth* **2007,** 307, (1), 76-81.

78. Zhu, Y. Q.; Jin, Y. Z.; Kroto, H. W.; Walton, D. R. M., Co-catalysed VLS growth of novel ceramic nanostructures. *J. Mater. Chem.* **2004,** 14, (4), 685-689.

79. Liu, Y. M.; Li, Q. Q.; Fan, S. S., Self-catalytic growth of aluminum borate nanowires. *Chem. Phys. Lett.* **2003,** 375, (5, 6), 632-635.

80. Wu, Y.; Yang, P., Direct observation of vapor-liquid-solid nanowire growth. *J. Am. Chem. Soc* **2001,** 123, 3165-3166.

81. Wu, Y.; Fan, R.; Yang, P., Block-by-block growth of single-crystalline Si/SiGe superlattice nanowires. *Nano Lett.* **2002,** 2, 83-86.

82. Solanki, R.; Huo, J.; Freeouf, J. L.; Miner, B., Atomic layer deposition of ZnSe/CdSe superlattice nanowires. *Appl. Phys. Lett.* **2002,** 81, 3864-3866.

83. Zhang, H. Z.; Kong, Y. C.; Wang, Y. Z.; Du, X.; Bai, Z. G.; Wang, J. J.; Yu, D. P.; Ding, Y.; Hang, Q. L.; Feng, S. Q., Ga_2O_3 nanowires prepared by physical evaporation. *Solid State Commun.* **1999,** 109, 667-682.

84. Han, W. Q.; Kohler-Redilich, P.; Ernst, F.; Ruhle, M., Growth and microstructure of Ga_2O_3 nanorods. *Solid State Commun.* **2000,** 115, 527-529.

85. Li, J. Y.; Qiao, Z. Y.; Chen, X. L.; Chen, L.; Cao, Y. G.; He, M.; Li, H.; Cao, Z. M.; Zhang, Z., Synthesis of β-Ga_2O_3 nanorods. *J. Alloys Compd.* **2000,** 306, 300-302.

86. Pan, Z. W.; Dai, Z. R.; Wang, Z. L., Nanobelts of semiconducting oxides. *Science* **2001,** 291, 1947-1949.

Chapter 3: TaS_2 Nanoplatelets Produced By Laser Ablation

Published: Ka Yee Chick, Manashi Nath and B. A. Parkinson,

Journal of Materials Research, **21**, 1243, (2006).

3.1 Abstract:

Tantalum disulfide nanoplatelets were produced by laser ablation of a TaS_2 target under an argon atmosphere. The nanoplatelet dimensions and morphology were characterized by transmission electron microscopy and x-ray diffraction. The effect of the ablation laser power density on the size distribution of the nanoplatelets was studied. The TaS_2 nanoplatelets were prone to oxidation upon exposure to air but could be stabilized by using 3-mercaptopropionic acid as the capping agent.

3.2 Introduction:

Layered transition metal dichalcogenides (TMD) have a structure similar to graphite, however, each graphene sheet is replaced by a MX_2 layer containing the transition metals (such as Ta, W, Mo) in a trigonal prismatic or octahedral coordination sandwiched by layers of chalcogen atoms.[1] Nanosized TMD materials tend to fold into closed structures in order to reduce the energy of the dangling bonds, thus a range of closed—cage structures such as multishell onion-like clusters, generically called inorganic fullerenes have been prepared.[2] Nanotubes,[3,4] nanowires and nanoribbons can also be obtained.[5] TMD nanomaterials have a wide range of chemical and physical properties that make them attractive for many applications.[6-9] TMD materials can be semiconducting, metallic or even superconducting.[1]

There are a variety of synthetic methods for producing TMD nanomaterials. Nanotubes have been synthesized by gas-phase methods,[2,3] template methods[10] and sonochemical methods.[11] Inorganic fullerene (IF) materials can be prepared by a gas-phase method,[12] electron irradiation[13] or by laser ablation.[12,14,15,16,17] Nanoplatelets of MoS_2 and InSe can be prepared via solution chemistry.[18,19] Laser ablation, commonly applied in mass spectrometry[20] and for thin film deposition,[21] is a non-equilibrium growth process useful for synthesizing nanomaterials and was used in the discovery of C_{60}.[22] Laser ablation for nanoparticle production can take place under either an inert gas environment[14,15] or in a liquid medium.[16] In the case of laser ablation under an inert gas, the laser beam removes material from the surface of the target by

vaporization. Subsequently during the adiabatic cooling process of the vaporized target material, nanoparticles can be formed.

In this article, we report the production of TaS_2 nanoplatelets via laser ablation of a TaS_2 target in an argon gas environment and investigate the size distribution of the TaS_2 nanoplatelets as a function of the laser power. We also report the stabilization of solution suspensions of TaS_2 nanoplatelets by 3-mercaptopropionic acid (3-MPA).

3.3 Experimental method:

TaS_2 powder (99.9% Ta) was purchased from Strem Chemicals, Inc. and was used without further purification. 3-mercaptopropionic acid (3-MPA) was purchased from Aldrich and was also used without further purification. Copper transmission electron microscopy (TEM) grids, with lacey Formvar/carbon polymer as the support film, were purchased from Ted Pella, Inc. TEM was carried out on JEOL 2000 TEM, operating at an accelerating voltage of 100-200 kV. Powder X-ray diffraction (XRD) of the samples was carried out on Brüker D-8 Discover x-ray diffractometer (Cu x-ray source, line focus) with a Göbel mirror on the primary beam side and a scintillation detector on the diffracted beam side. The angle of incidence was 0.5° and the measurements were performed with soller slits. Topas P Version 1.0.1 was used as the profile fitting software for the size analysis of the nanoplatelets.

A pulsed Nd:YAG laser (DCR11 from Spectra-Physics), with a fundamental wavelength at 1064 nm, was used as the laser source. It was operated in the Q-switch

mode at 10 Hz with a 9 ns pulse width. The laser average output power was set between 0.1 – 2.6 W resulting in a peak power between 1.1 – 29 MW. A 40 cm focal length lens was used to converge the laser beam to the spot close to 3 mm in diameter. The laser pulse energy density, therefore, was calculated to be between 16–410 MW cm^{-2}.

TaS_2 powder (5-6 grams) was pressed into a 33 mm diameter pellet. The as-prepared pellet was clipped to a sample holder located in the reaction chamber equipped with an optical window. The reaction chamber was first pumped down to a pressure below 50 mTorr before filling with 200 Torr of argon. This argon pressure was found to be optimum for preparation of the nanoplatelets. To increase the efficiency of ablation, the sample holder was attached to a motor to rotate the TaS_2 pellet during the experiment thus allowing more areas on the pellet to be ablated. A TEM grid was placed in the reaction chamber to collect samples generated from the laser ablation. The laser ablation was started after 10 min of purging or when the Ar pressure inside the reaction chamber stabilized. The duration of a typical laser ablation run was 20 min.

3.4 Results/discussion:

Laser ablation of the TaS_2 target produced black soot-like material. Figure 1a-c show the TEM images of the soot collected in the reaction chamber at various laser power densities. The TEM images revealed that hexagonal nanoplatelets were the dominant product however some nanospheres were also seen. Figure 2a-c shows

the TEM images of TaS_2 nanoplatelets oriented at different angles that clearly are projections of the hexagonal form of the platelets. Tilting experiments in the TEM also verified the hexagonal structure. The interlayer distances in the nanoplatelets, obtained from the TEM lattice fringes, were between 6.50 and 5.50 Å, whereas the bulk TaS_2 materials has an interlayer distance of 5.94 Å.[1]

The edge lengths of the nanoplatelets were also measured from the TEM images. Figure 3a-d show the histograms of size distributions of nanoplatelets produced at various laser power densities. It can be seen that the laser pulse energy density has an effect on the size distribution of the nanoplatelets. Comparing the histograms of Figure 3a to Figure 3d, shows that smaller nanoplatelets with a narrower size distribution were produced at a higher laser power density. One could speculate that the higher laser power densities produce a higher pressure plasma resulting in a faster adiabatic expansion of the vaporized plume, and thus a higher cooling rate, resulting in a shorter growth time for the nucleated nanoparticles and thus a narrower size distribution.

One can also speculate about the mechanism of growth of the TMD nanoparticles. The high power densities in the initial stage of ablation results in complete vaporization of a portion of the target material. The subsequent adiabatic expansion cools the plume resulting in an initial nucleation and growth of the least volatile component of the plume, in this case Ta metal. The Ta metal nanoparticles are still engulfed in an environment of hot chalcogenide vapor resulting in a reaction to form TaS_2 nanoparticles. If the Ta nanoparticles in the plume are hexagonal, a

reasonable morphology for a metal crystal, a hexagonal nanoplatelet is then templated. Octahedral nanoparticles of MoS_2, previously prepared by laser ablation of an MoS_2 target,[23] could be formed from a reaction of an octahedral nanocrystal of Mo templating the MoS_2 layers from subsequent reaction with sulfur vapor.

The powder XRD pattern of material generated by the laser ablation power density of 158 MW cm^{-2}, and containing a large fraction of nanoplatelets, revealed diffraction peaks associated with TaS_2 (Figure 4a).[24] Analyzing the peak broadening observed for a particular TaS_2 powder XRD peak using the Scherrer method (profile fitting program Topas P Version 1.0.1) gives an average particle size of 18.8 nm. The same sample of nanoplatelets analyzed with TEM images showed sizes between 6-20 nm (Figure 3b).

The TaS_2 nanoplatelets generated by laser ablation were not very stable under ambient conditions. The powder XRD pattern in Figure 4a was obtained immediately following the synthesis. Exposure of the same sample to air for one day produced a different powder XRD pattern showing that the TaS_2 converted to TaO_2 and Ta_2O_5 (Figure 4b). The powder XRD results were reproducible for all experiments, with variations in tantalum sulfide and tantalum oxide ratio. TEM images, after samples were exposed to air, lose their clarity as the sample degrades with time due to conversion to the oxide, and no longer showed the lattices fringes associated with the nanoplatelet's 5.50 to 6.50 Å interlayer distances.

Stabilizing the nanostructures with a capping agent could possibly reduce the oxidation rate of the TaS_2 nanoplatelets. Many other nanomaterials have been

stabilized by capping agents.[25,26] The oxidation of the nanoplatelets most likely starts with the dangling bonds at the edge of the nanoplatelets, since the hexagonal faces are rather inert van der Waals surfaces. Therefore we attempted to react the dangling bonds associated with the tantalum edge states with a thiol containing ligand. 3-Mercaptopropionic acid (3-MPA) was chosen as the capping agent since we are also interested in producing a charge on the platelets to disperse the nanoplatelets and stabilize the solution as a colloid. TaS_2 nanoplatelets generated from the laser ablation were collected from the reaction chamber and soaked in a 1.4 M aqueous solution of the sodium salt of 3-MPA. TEM images of the nanoplatelets, which were kept for 8 days in the aqueous 3-MPA solution exposed to air, showed fringes of the usual spacing indicating that the TaS_2 nanoplatelets were successfully stabilized for at least a week by the 3-MPA solution.

As discussed above, the laser power density affected the particle size. Lower laser power densities also produced a higher percentage of spherical nanoparticles amongst the nanoplatelets. The spherical nanoparticles showed a wide range of diameters from 10 to 500 nm. Energy dispersive X-ray spectroscopy, EDS, analysis of the nanospheres revealed that they were composed of tantalum and sulfur, but were tantalum rich. Lattice fringes were observed in TEM images in different domains on the surface of the sphere, however the fringe interlayer distances were not uniform even on the same nanosphere. Those nanospheres could be the produced when the droplets of melted Ta produced by the laser only partially reacted with sulfur during cooling. The lower laser power density results in some tantalum liquid droplets rather

than complete vaporization as discussed in the mechanism above. The tantalum droplets are then only partially reacted with sulfur resulting in Ta rich spherules. An SEM image, shown in Figure 5, shows that the surface of a nanosphere is not smooth. This suggests that some nanoclusters can aggregate on the surface of the nanospheres.

3.5 Conclusions:

We have demonstrated the synthesis of nanoplatelets of TaS_2 via laser ablation in an Ar atmosphere. The size distribution of nanoplatelets was dependent on the laser power density. Spherical tantalum-rich nanoparticles are also produced under some ablation conditions. The TaS_2 nanoplatelets were not very stable and converted to Ta_2O_5 when exposed to air and moisture for even short periods. However, by employing 3-MPA as a capping agent the TaS_2 nanoplatelets were stabilized in aqueous solutions for over one week.

Acknowledgements

Financial support from NSF grant number DMR 0107429 supported this work. Dr. Paul Schroeder and Jerimiah Forsythe are acknowledged for the design of the reaction chamber. Technical support from Dr. Sandeep Kohli from Colorado State University is also acknowledged.

References

1. A. D. Yoffe, J. A. Wilson: The transition metal dichalcogenides: Discussion and interpretation of observed optical, electrical and structural properties. *Adv. Phys.* **18**, 193 (1968).

2. R. Tenne, L. Margulis, M. Genut, G. Hodes: Polyhedral and cylindrical structures of tungsten disulfide. *Nature* **360**, 444 (1992).

3. R. Tenne, M. Homyonfer, Y. Feldman: nanoparticles of layered compounds with hollow cage structures (inorganic fullerene-like structures). *Chem. Mater.* **10**, 3225 (1998).

4. C. N. R. Rao, M. Nath: Inorganic nanotubes. *Dalton Trans.* **1**, 1 (2003).

5. Q. Li, E. C. Walter, W. E. van der Veer, B. J. Murray, J. T. Newberg, E. W. Bohannan, J. A. Switzer, J. C. Hemminger, R. M. Penner: Molybdenum disulfide nanowires and nanoribbons by electrochemical/chemical synthesis. *J. Phys. Chem. B.* **109**, 3169 (2005).

6. A. Carlsson, M. Brorson, H. Topsoe: Morphology of WS_2 nanoclusters in WS_2/C hydrodesulfurization catalysts revealed by high-angle annular dark-field scanning transmission electron microscopy (HAADF-STEM) imaging. *J. Catal.* **227**, 530 (2004).

7. L. M. Kulikov, A. A. Semenov-Kobzar, K. E. Grinkevich, I. A. Kossko, L. G. Aksel'rud, L. P. Romaka: Dispersion of transition-metal dischalcogenides and their intercalation compounds. *Inorg. Chem.* **33**, 1008 (1997).

8. M. Remskar, Z. Skraba, R. Sanjines, F. Levy: MoS_2 and WS_2 nanotubes alloyed with gold and silver. *Surf. Rev. Lett.* **6**, 1283 (1999).

9. L. Rapoport, Y. Leshchinsky, Y. Volovik, M. Lvovsky, O. Nepomnyashchy, Y. Fieldman, R. Popovitz-Biro, R. Tenne: Modification of contact surfaces by fullerene-like solid lubricant nanoparticles. *Surf. Coat. Technol.* 405 (2003).

10. C. M. Zelenski, P. K. Dorhout: Template synthesis of near-monodisperse microscale nanofibers and nanotubules of MoS_2. *J. Am. Chem. Soc.* **120**, 734 (1998).

11. L. Qiu, V. G. Pol, Y. Wei, A. Gedanken: A two-step process for the synthesis of $MoTe_2$ nanotubes: combing a sonochemical technique with heat treatment. *J. Mater. Chem.* **13**, 2985 (2003).

12. C. Schuffenhauer, B. Parkinson, N. Y. Jin-Phillipp, L. Joly-Porttuz, J. Martin, R. Popovitz-Biro, R. Tenne: Synthesis of fullerene-like tantalum disulfide nanoparticles by a gas-phase reaction and laser ablation. *Small.* **0**, 1 (2005).

13. M. Jose-Yacaman, H. Lopez, P. Santiago, D. H. Galvan, I. L. Garzon, A. Reyes: Studies of MoS_2 structures produced by electron irradiation. *Appl. Phys. Lett.* **69**, 1065 (1996).

14. P. A. Parilla, A. C. Dillon, K. M. Jones, G. Riker, D. L. Schulz, D. S. Ginley, M. J. Heben: The first true inorganic fullerene? *Nature* **397**, 6715 (1999).

15. R. Sen, A. Govindaraj, K. Suenaga, S. Suzuki, H. Kataura, S. Iijima, Y. Achiba: Encapsulated and hollow closed-cage structures of WS_2 and MoS_2 prepared by laser ablation at 450-1050°C. *Chem. Phys. Lett.* **340**, 242 (2001).

16. M. Nath, C. N. R. Rao, R. Popovitz-Biro, A. Albu-Yaron, R. Tenne: Nanoparticles produced by laser ablation of HfS_3 in liquid medium: inorganic fullerene-like structures. *Chem. Mater.* **16**, 2238 (2004).

17. Y. Rosenfeld-Hacohen, R. Popovitz-Biro, Y. Prior, S. Gemming, G. Seifert, R. Tenne: Synthesis of $NiCl_2$ nanotubes and fullerene-like structures by laser ablation: theoretical considerations and comparison with MoS_2 nanotubes. *Phys. Chem. Chem. Phys.* **5**, 1644 (2003).

18. V. Chikan, D. F. Kelley: Size-dependent spectroscopy of MoS_2 nanoclusters. *J. Phys. Chem. B.* **106**, 3794 (2002).

19. S. Yang, D. F. Kelley: The spectroscopy of InSe nanoparticles. *J. Phys. Chem. B.* **109**, 12701 (2005).

20. V. Carre, F. Aubriet, P. T. Scheepers, G. Krier, J. F. Muller: Potential of laser ablation and laser desorption mass spectrometry to characterize organic an inorganic environmental pollutants on dust particles. *Rapid Commun. Mass Spectrom* **19**, 871 (2005).

21. C. V. Ramana, R. J. Smith, O. M. Hussain, M. Massot, C. M. Julien: Surface analysis of pulsed laser-deposited V_2O_5 thick films and their lithium intercalated products studied by raman spectroscopy. Surf. *Interface Anal,* **37**, 406 (2005).

22. H. W. Kroto, J. R. Heath, S. C. O'Brein, R. E. Smalley: C_{60}: Buckminsterfullerene. *Nature* **318**, 162 (1985).

23. P. A. Parilla, A. C. Dillon, B. A. Parkinson, K. M. Jones, J. Alleman, G. Riker, D. S. Ginley, M. J. Heben: Formation of nanooctahedra in molybdenum disulfide and molybdenum diselenide using pulsed laser vaporization. *J.Phys. Chem. B.* **108**, 6197 (2004).

24. [JCPDS file, card number 83-48] for orthorhombic (with lattice constant: a=5.7500 Å, b=3.30800 Å, c=23.76000 Å); [JCPDS file, card number 73-2201]) for hexagonal (Rh) TaS_2 (with lattice constant: a=3.3400 Å, b=3.3400 Å, c=35.9400 Å)

25. N. K. Chaki, K. P. Vijaymohanan: Temperature-induced phase transitions of the ordered superlattice assembly of Au nanoclusters. *J. Phys. Chem. B* **109**, 2552 (2005).

26. Z. Peng, T. Walther, K. Kleinermanns: Influence of intense pulsed laser irradiation on optical and morphological properties of gold nanoparticle aggregates produced by surface acid-base reactions. *Langmuir* **21**, 4249 (2005).

Captions for the figures

Figure 1. TEM images of TaS_2 nanoplatelets produced at different laser power densities: 409 MW cm^{-2} (b) 79 MW cm^{-2} (c) 28 MW cm^{-2}. The scale bar in each image is to 20 nm.

Figure 2. High magnification TEM images of different hexagonal TaS_2 nanoplatelets in various orientations : a) top view b) side view c) oblique angle (all nanoplatelets shown here were produced with a laser power density of 409 MW cm^{-2}).

Figure 3. Histograms of the size distribution of nanoplatelets produced at different laser power densities: (a) 409 MW cm^{-2} (b) 158 MW cm^{-2} (c) 79 MW cm^{-2} (d) 28 MW cm^{-2} (x-axis: Platelet Length (nm), y-axis: Frequency %)

Figure 4. XRD patterns of the nanomaterials: (a) collected immediately after opening the chamber; (b) after the product was kept in air for a day. Unlabeled peaks could not be identified. (The nanoplatelets were produced with a laser power density of 409 MW cm^{-2}.)

Figure 5. SEM image of nanospheres produced by laser ablation at 330 MW/cm^{-2} of Laser power density. The scale bar is 100 nm.

Figures

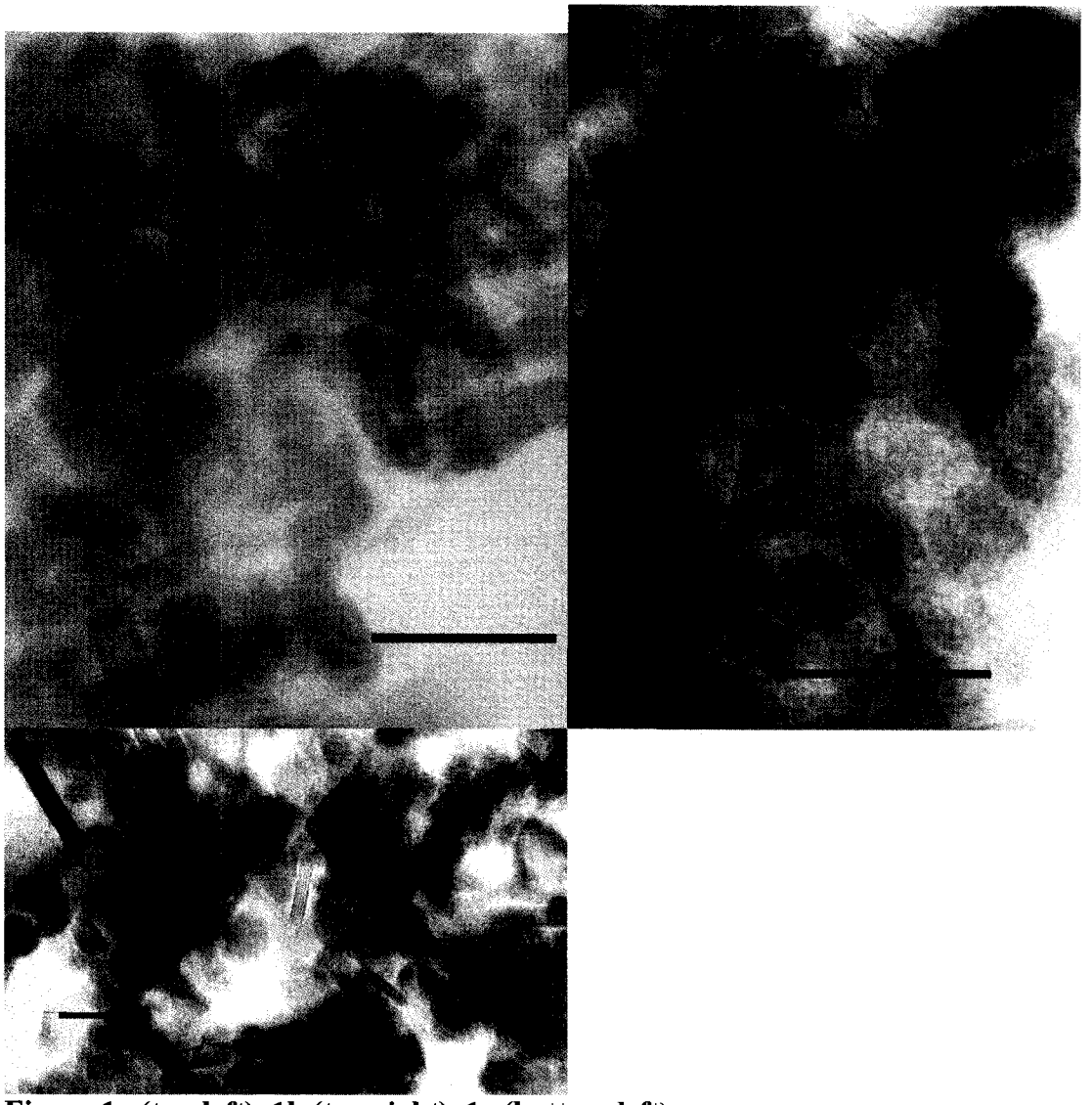

Figure 1a (top left), 1b (top right), 1c (bottom left)

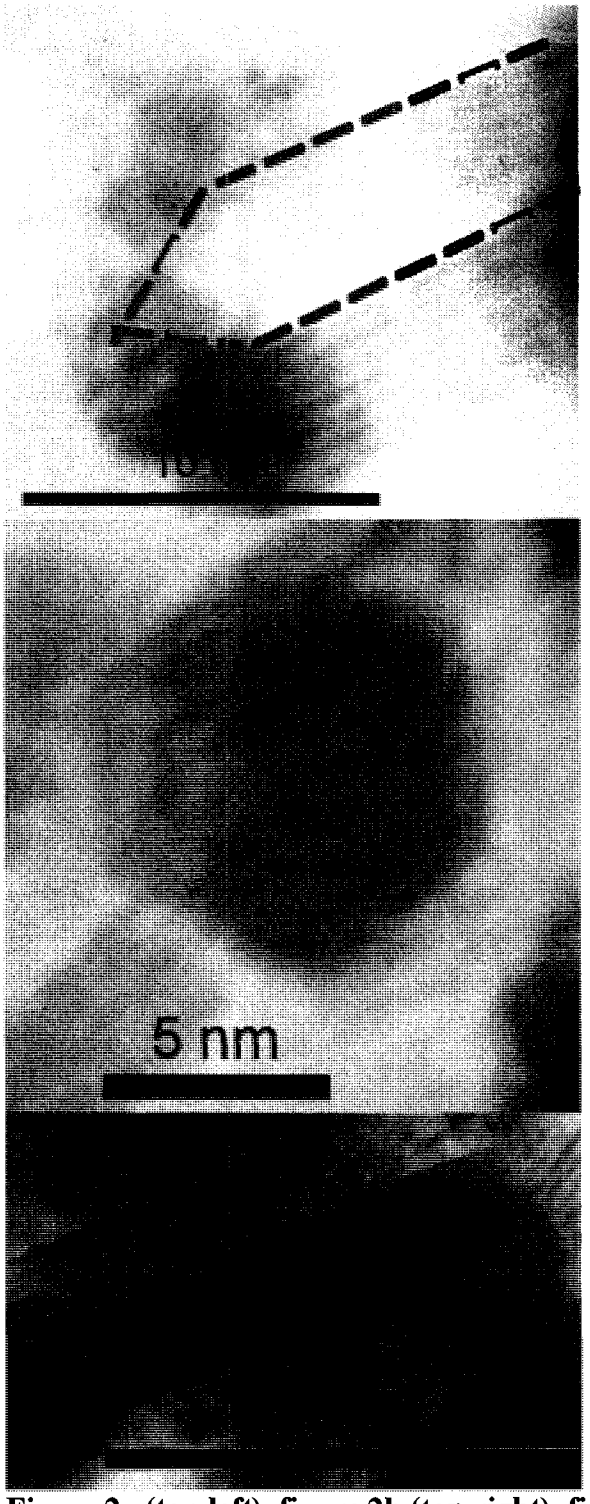

Figure 2a (top left), figure 2b (top right), figure 2c (bottom left)

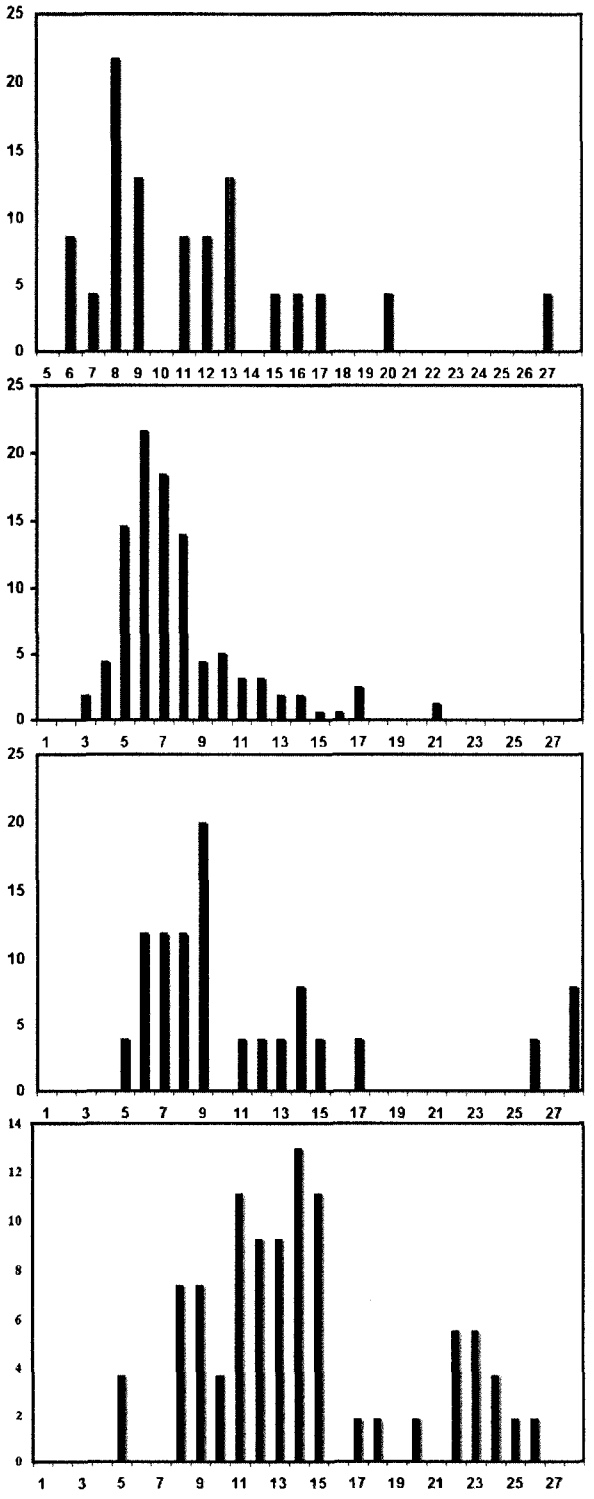

Figure 3 a (top left), figure 3b (top right), figure 3c (bottom left), figure 3d (bottom right)

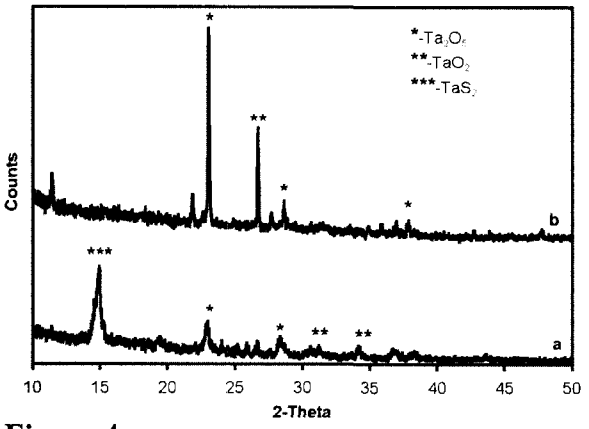

Figure 4

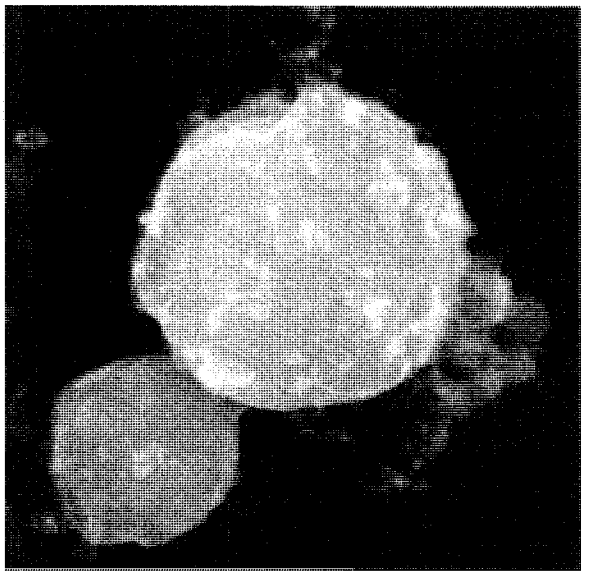

Figure 5

Chapter 4: Laser Irradiation In Liquid Medium And Laser Ablation Using A Femtosecond Pulsed Laser

4.1 Abstract

In this chapter, two different laser irradiation/ablation experiments will be described: laser irradiation of TaS_2 in liquid phase, and laser ablation of MoS_2 using a femtosecond pulsed laser. Different nanostructures resulted from the two different laser irradiation/ablation experiments. Significant effort was expended, however future work needs to be done.

4.2 Laser irradiation of TaS_2 in liquid medium

4.2.1 Introduction

Laser ablation of solid in liquid medium for material synthesis was first reported in 1987,[1] when meta-stable iron oxides were prepared on the surface of bulk iron by laser ablating an iron target in water. Research has shown that higher pressures can be generated within the plasma, when laser ablation takes place in a liquid medium instead of an inert gas atmosphere or vacuum. The ablation rate, therefore, can be much faster in a liquid than in a gas environment, which ultimately improves the overall yield from the laser ablation process.[2] The quenching time of laser plasma in liquid medium is also shorter when compared to an inert gas or vacuum environment. Because the characteristics of the plasma in liquid are different from inert gas, a new opportunity for nanomaterial synthesis is provided. Significant progress has been made in synthesizing nanomaterials by using laser ablation of solids in various confining liquids. For example, colloidal nanoparticles of noble metals have been prepared by laser ablation in solvents.[3-5] ZnSe and CdS nanoparticles have been synthesized by laser ablation of corresponding bulk semiconductors in liquid media (such as diethylene glycol and ethanol).[6]

According to the previous findings for laser ablation of a TaS_2 pellet (Chapter 3), the as-produced nanoplatelets were unstable when exposed to air. The unstable materials made sample collection and characterization difficult. This raised several questions, first, is it possible to increase the yield of nanoplatelets in a liquid medium? Second, can the integrity of these materials be maintained, in other words,

stabilizing the nanoplatelets by laser ablating in a liquid medium? Furthermore, the growth mechanism of nanomaterials by laser ablation in a liquid medium, as mentioned above, can be different than the growth mechanism at work in the inert gas atmosphere.[7] This brings us to the last question, is it possible to alter the morphology of these ablated materials when they are produced in liquid medium?

To answer these questions, several attempts were made by using TaS_2 powder, and laser irradiating it in *tert*-butyl disulfide ($C_8H_{18}S_2$, TBS). The exact definition of laser ablation is the massive removal of target materials by laser irradiation. The experimental procedure for this project, which will be described in greater detail in the next section, however, did not qualify to be laser ablation, since no target material was removed. This project, therefore, can only be referred to as laser irradiation for the production of nanoparticles. The research was based on previous work from Nath. *et.al.*[8] TBS was chosen as the liquid medium for this experiment due to its transparency at the irradiation wavelengths. More importantly, it can undergo decomposition under laser ablation to produce sulfur. The decomposition of TBS can be written as follows:

$$Bu^t\text{-}S\text{-}S\text{-}Bu^t \rightarrow 2CH_2{=}CMe_2 + HSSH \qquad \text{(Equation 4.1)}^9$$

and HSSH further decomposes into:

$$HSSH \rightarrow H_2S + S \qquad \text{(Equation 4.2)}^9$$

4.2.2 Experimental procedure

TaS_2 powder and TBS both were used without further purification. A Q-switched pulsed Nd:YAG laser was employed for laser irradiation. Both fundamental (1064 nm), and the second harmonic (532 nm) laser wavelengths were used. Laser power was varied from 0.35 to 0.5 W. The time of laser irradiation ranged from 20 to 30 min.

The schematic of the experimental setup is shown in Figure 4.1. TaS_2 powder (0.004 g, 0.16 μmol) was dispersed in TBS (varied from 4-8 mL) under sonication for 10 min. The dispersion (4 mL) was then transferred to a special quartz cell (Figure 4.1 in grey) right before the laser ablation. The center of the quartz cell was adjusted to be 40 cm away from the 40 cm focusing lens. Duration the laser irradiation, bubbles and illumination were generated at the focus spot in the liquid medium. The color of the dispersion was changed from gray to deep black during the laser irradiation. The amounts of TaS_2 and laser power used for laser irradiation were varied in order to study the effect of changing the reaction parameters on structures of the as-produced nanomaterials.

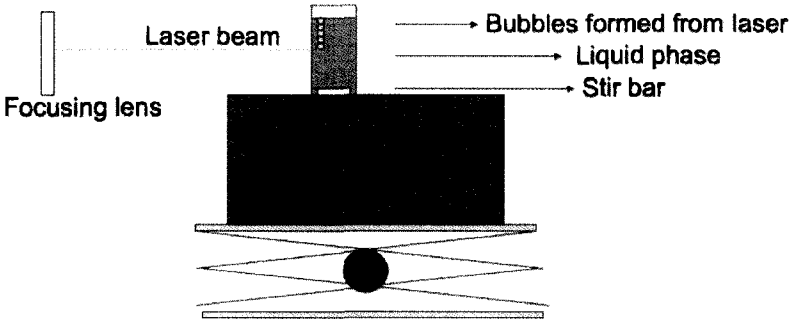

Figure 4.1 The schematic of the laser ablation in liquid medium setup. (not in scale)

After the irradiation, the dispersion was allowed to set for 30 minutes, to allow for sedimentation. The nanomaterials from laser irradiation in TBS were characterized by TEM. To prepare samples for the TEM, products were collected from the top portion of the dispersion since largest particles (i.e. bulk size materials) usually settled near the bottom. Next the TBS was evaporated. Because the boiling point of TBS is around 200 °C, TBS was removed in the Schlenk line located in the Dorhout group overnight before TEM imaging.

4.2.3 Experimental results and discussion

TEM results indicate that the nanomaterials prepared by laser irradiation of TaS_2 in liquid medium formed different morphologies [Figure 4.2] than those prepared under an inert gas atmosphere. Sphere-like nanoparticles were the majority product, however, with a wide size distribution, ranging from 2 to 200 nm in diameter.

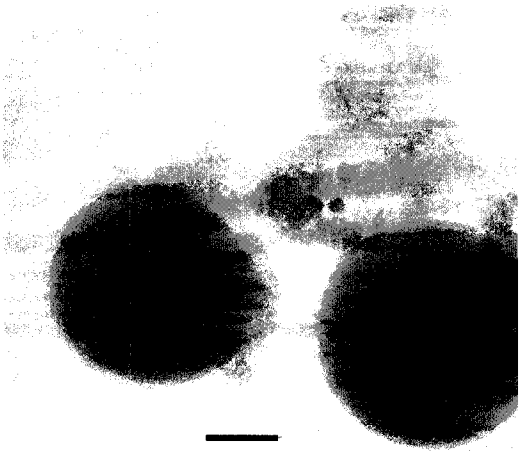

Figure 4.2 TEM image of typical laser irradiation products in liquid TBS. Scale bar is equal to 20 nm.

The appearance of these spherical nanoparticles was different, depending on their size. High magnification TEM images of the larger size nanospheres (at least 50 nm in diameter) revealed the closed-cage, layered structures [Figure 4.3]. The interlayer spacing of these structures was measured to be 0.7 nm (± 0.1 nm), comparable to the literature value of TaS_2 (001) plane (0.602 nm).[10] The average number of layers in these nanospheres was 6. The layers usually were not smooth and frequently showed many defects (for instance, kinks and dislocations). It is believed that such defects relieved strain from the curvature of the TaS_2 layers. It is unclear whether or not the core of these close-caged nanospheres was hollow. Smaller size nanoparticles (5 nm on average) were found agglomerating on the larger close-caged nanospheres (see Figure 4.3). TEM images showed periodic fringes on some of these smaller size nanoparticles, suggesting that they were crystalline materials. However, the true identity of the smaller size nanospheres is still unknown.

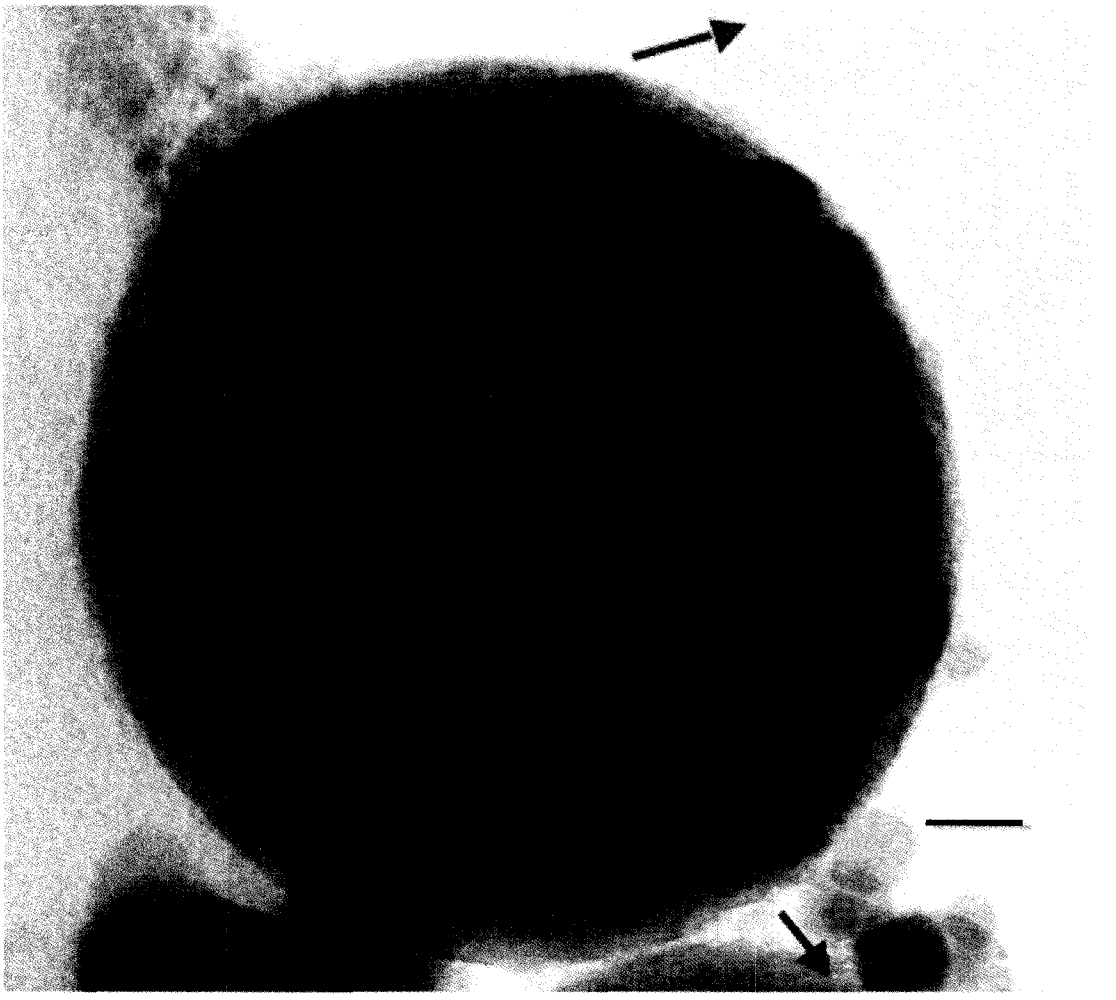

Figure 4.3 TEM image of one closed-cage nanosphere of tantalum sulfide, with smaller size nanoparticles distributed on its surface. Aqua arrow: the dislocation of the layered structures. Red arrow: the kink from the layered structures. Scale bar is equal to 10 nm.

Variations in the reaction parameters, including the amount of TaS_2 and the amount of laser power, did not yield different results in the experiment. The majority of products produced by the experiment continued to be polydisperse nanospheres. The results, however, were inconclusive due to the small variation in the laser power (0.35 -0.5W) used. More drastic variations will be necessary in order to show the impact on the nanomaterials formations. To do so, a different cell design will be required: walls of the original cell used in this laser ablation were too thin to sustain under the high laser power impact.

A small plasma plume was observed from laser irradiation in liquid. This laser-induced plasma was in a high temperature and high pressure state. The new phase of material, therefore, could be formed by the high-temperature chemical reactions of the target materials. It is believed that the amorphous droplets of material were formed initially, acting as the templates for the resulting spherical shape nanoparticles. When the plasma plume condensed and spread into the liquid during the plasma quenching, recrystallization occurred to some of these templates, which lead to the formation closed-cage nanospheres.

The advantage of this particular laser irradiation setup over the traditional laser ablation in liquid media was about the position of solid target. Most researches constructed laser ablation in liquid by using a fixed solid target, with the pellet of solid was submerged in liquid. When the dispersion of solid powder was used, it was under stirring throughout the irradiation. The irradiated materials were able to transport to the different parts of the dispersion, which allowed the continuation of the

irradiation with fresh target materials. As a result, the efficiency of this laser irradiation process should be higher than laser ablation process in liquid media.

4.3 Laser ablation with femtosecond pulsed laser

4.3.1 Introduction

In order to construct a detail investigation of laser ablation under inert gas atmosphere, different reaction conditions, including laser parameters, has been studied. The detailed description of different experimental parameters variations have already been presented in Chapter 3. A pulsed Nd:YAG laser has been employed as the laser source for the laser ablation project at the Parkinson group, however, the maximum laser power density was limited to 160 MW/cm^2. Furthermore, the pulse width produced from the Nd:YAG laser was fixed as constant of 9 ns. Studies have shown that the laser ablation mechanism of ultra-short pulsed laser (such as femtosecond pulsed laser) can be different from the nanosecond pulsed one.[11-15] In order to extend the coverage in laser parameters, laser ablations with femtosecond pulsed laser were proposed to perform. Our group is now collaborating with the Squier group from Colorado School of Mines since their laboratory is equipped with Kilohertz TW laser [Figure 4.4]. The results presented here are preliminary, since the project is still on going.

Figure 4.4 Kilohertz TW laser system located in the Squier laboratory at CSM.

The ultra-short pulsed laser-material interaction is a non-equilibrium process, with the heating, plasma plume formation, and material ejection occur well after the laser pulse.[16] When a fs pulsed laser impinges on a sample, electrons are excited by the photoionization and avalanche ionization process in a tens of femtoseconds timescale, with a subsequent energy transfer from electrons to ions in the picosecond timescale. The lattice temperature, as the result, remains unchanged during the absorption of ultra-short laser pulse. The laser pulse energy is mainly transferred through the photon–electron interaction process. Therefore, the photon absorption depth rather than thermal diffusion depth governs the heated volume. Eventually heat transfer leads to the vaporization of transiently heated target. The plasma plume is generated as the result of high temperature and vapor ion/electron amount. Since no plasma absorption of laser energy occurs during the laser ablation, the absorbed laser

energy is fully deposited to the target, and thus, higher efficiency of laser ablation can be obtained.

During the plasma plume expansion the plasma plume expands without any other heating process (i.e. absence of laser pulse), this process is different than the laser ablation with nanosecond pulsed laser. As a result, the plasma plume expansion loses the temperature (pressure) faster, with shorter lifetime. The photomechanical effects induced by the pressure relaxation plays an important role in material ejection. After the laser pulse, material ejection continues as the result of relaxation of the laser-induced pressure gradient. Since laser ablation mechanism with femtosecond pulsed laser is different from the mechanism with nanosecond pulsed laser, it is possible to generate different structures of nanomaterials with femtosecond pulsed laser than with nanosecond pulsed laser.

MoS_2 was used as the target materials in this laser ablation experiment. Bulk 2-H MoS_2, the commonly seen polytype, displays a hexagonal layered structure ($P6_3/mmc$), with two sandwich layers per unit cell (c=12.3 Å). Belongs to the family of layered material, MoS_2 nano-octahedra had been prepared from laser ablation with nanosecond pulsed laser, however, the yield of such nano-octahedra was low.[17] It is, therefore, of interest to investigate the effect of using femtosecond pulsed laser on the production of MoS_2 nano-octahedra.

4.3.2 Experimental procedures

Nicholas Brown, a graduate student from the Squier group, was the operator for the laser ablation with femtosecond pulsed laser. The laser ablation apparatus

described in Chapter 2 was relocated to the Squier laboratory. Copper transmission electron microscopy (TEM) grids (from Ted Pella, Inc) were used to collect sample for TEM use. JEOL 2000 TEM, operating at an accelerating voltage of 160 kV, was carried out on the prepared Cu TEM grids. HR-TEM, operating at an accelerating voltage of 200 kV, was also carried out on Philips CM200 TEM.

Basic setup

MoS_2 was pressed into a pellet of 2.5 cm in diameter, and was placed into the reaction chamber. Mechanical pump was employed to evacuate the reaction chamber. When the chamber reached a pressure of 100 mTorr, 100 Torr of Ar gas was purged into the chamber to begin the laser ablation. The total duration of the laser ablation was 3 min. The as-produced nanomaterials were collected on a glass plate during the laser ablation process, and were transferred to TEM grids before sample characterization.

Femtosecond pulsed laser conditions

The femtosecond laser ablation was performed with a repetition rate of 1 kHz, Ti:sapphire chirped pulse amplification system. Laser pulses of 1 nJ from a 20 fs, 100 MHz Ti:sapphire oscillator were first stretched to 800 ps. A pockel cell pulse selector (located after the pulse stretcher) selected a 1 kHz pulse train (from the 100 MHz train) that was sent to the Ti:sapphire regenerative amplifier. The stretched, nanojoule pulses were then amplified to approximately 1.2 mJ. After amplification, the amplified pulses were sent through a grating compressor, resulting in 40 fs, 1 mJ pulses.

4.3.3 Experimental results

Craters were found on the ablated target after the laser ablation produced by femtosecond laser [Figure 4.5]. Spherical craters were the result of the off-angle-360° motion from the motor. The resulting craters, when compared to those generated from the nanosecond pulsed laser, were smoother. The finding confirmed the idea that femtosecond pulsed laser allowed for cleaner ablation.

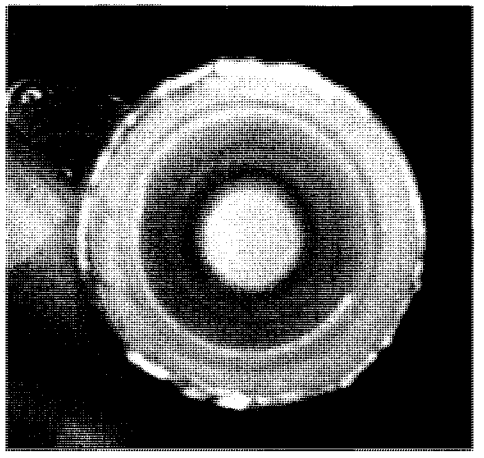

Figure 4.5 Typical target (MoS_2 pellet) after laser ablation, the spherical rings were the craters from the impact of laser ablations.

TEM images showed that different morphologies were generated within the sample during laser ablation. Different sizes of spherical-like particles were found. No fringes were found from these nanospheres, indicates that they could be amorphous materials.

A surprising discovery of this laser ablation experiment is that the nano-octahedra were also found from the same sample [Figure 4.6], with relatively high yield. The discovery confirmed the superior bending ability of MoS_2 layered

structures when compare to other layered materials, such as TaS_2. MoS_2 closed-cage structures consistently formed with different laser conditions (with nano- and femtosecond laser).

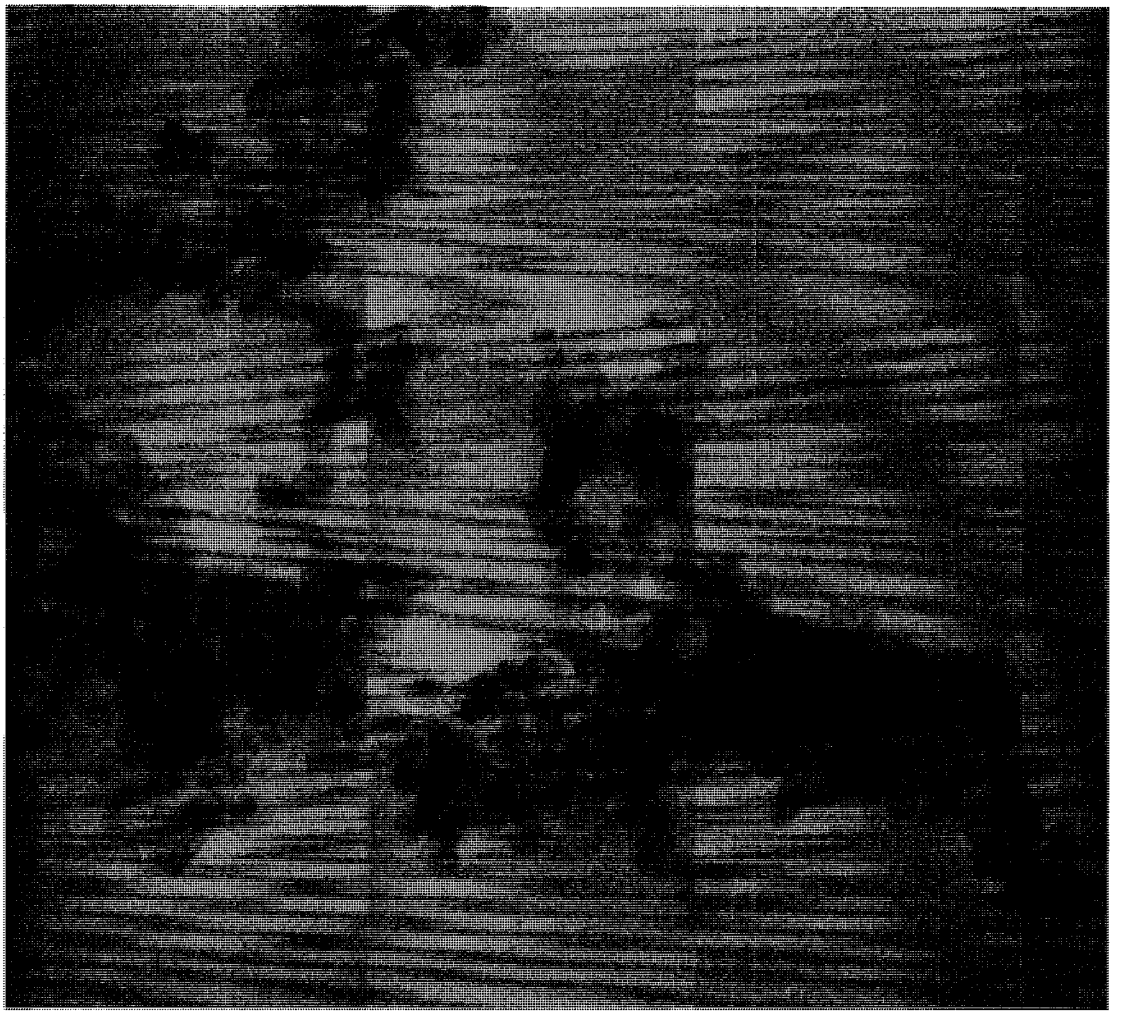

Figure 4.6 TEM image of the agglomerations of MoS_2 nano-octahedra. Scale bar is equal to 10 nm.

HR-TEM images of the MoS_2 nano-octahedra, which have been synthesized using the nanosecond pulsed laser, were also obtained [Figure 4.7].[17] The majority of

MoS_2 nano-octahedra formed in a 2-layer-nested structure, with some exceptions of 3-layer-nested structure. The direct measurement of spacing between the layers of nano-octahedra was 6.1 Å (± 0.5 Å), comparable to the bulk MoS_2 value (6.15 Å). Their outer edge lengths were measured to be 4.36 nm on average.

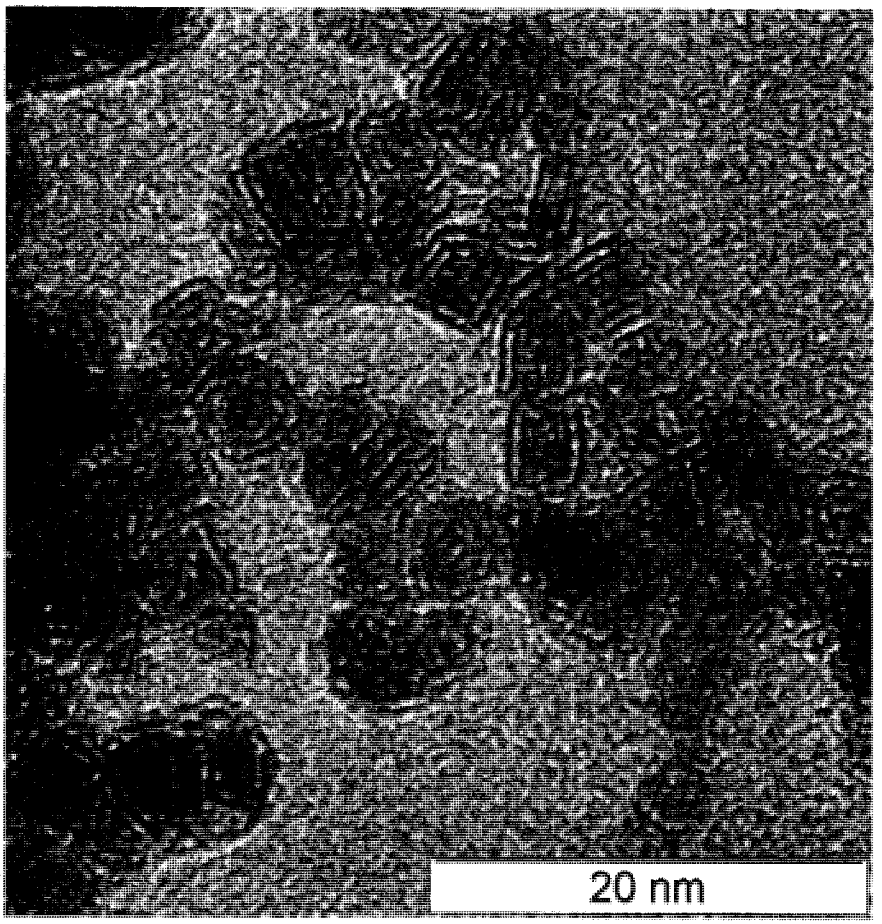

Figure 4.7 HR-TEM image of the MoS_2 nano-octahedra clusters.

4.4 Conclusion

Preliminary results of two different laser ablation projects were presented. In the projects of laser ablation of TaS_2 in liquid medium, different sizes of spherical-

like nanostructures were the majority products. Some of these products displayed layered shells (closed-cage structures). It is believed that droplets of amorphous tantalum sulfide formed after laser ablation in liquid, and the quick plasma quenching due to the liquid environment leads to the fast temperature drops. Recrystallization took place during the cooling process and formed the closed-cage spherical structures. In the projects of laser ablation of MoS_2 with femtosecond laser, two different morphologies of nanomaterials were found within the sample: nanospheres, and most importantly, nano-octahedra structures. These nano-octahedra were comparable to those generated by the nanosecond pulsed laser. The finding shows the high bending ability of MoS_2 layered structures, as the same closed-cage structures of MoS_2 were produced with different laser ablation parameters. These materials, however, required further characterization, such as SEM and XRD. Other experiments of laser ablation with femtosecond laser are ongoing, with new and more detailed conclusions to come.

Reference:

1. Patil, P. P.; Phase, D. M.; Kulkarni, S. A.; Ghaisas, S. V.; Kulkarni, S. K.; Kanetkar, S., M.; Ogale, S. B.; Bhide, V. G., Pulsed-laser-induced reactive quenching at liquid-solid interface: aqueous oxidation of iron. *Phys. Rev. Lett.* **1987,** 58, 238-241.

2. Zhu, S.; Lu, Y. F.; Hong, M. H.; Chen, X. Y., Laser ablation of solid substrates in water and ambient air. *J. Appl. Phys.* **2001,** 89, (4), 2400-2403.

3. Fojtik, A.; Henglein, A.; Bunsenges, B., Formation of nanometer-size silicon particles in a laser induced plasma in SiH_4. *Phys. Chem.* **1993,** 97, 252.

4. Simakin, A. V.; Voronov, V. V.; Shafeev, G. A.; Brayner, R.; Verduraz, F. B., Nanodisks of Au and Ag produced by laser ablation in liquid environment. *Chem. Phys. Lett.* **2001,** 348, 182.

5. Shafeev, G. A.; Freysz, E.; Verduraz, F. B., Self-influence of a femtosecond laser beam upon ablation of Ag in liquids. *Appl. Phys. A* **2004,** 78, (3), 307-309.

6. Anikin, K. V.; Melnik, N. N. S., A. V.; Shafeev, G. A.; Voronov, V. V.; Vitukhnovsky, A. G., Formation of ZnSe and CdS quantum dots via laser ablation in liquids. *Chem. Phys. Lett.* **2002,** 366, 357-360.

7. Fabbro, R.; Fourntier, J.; Ballard, P.; Devaux, D.; Virmont, J., Physical study of laser-produced plasma in confined geometry. *Appl. Phys.* **1990,** 68, 775-785.

8. Nath, M.; Rao, C. N. R.; Popovitz-Biro, R.; Albu-Yaron, A.; Tenne, R., Nanoparticles produced by laser ablation of HfS_3 in liquid medium: inorganic fullerene-like structures of Hf_2S. *Chem. Mater.* ***2004,*** 16, 2238-2243.

9. Voronkov, M. G.; Deryagina, E. N., Thermal transformations of organic compounds of divalent sulfur. *Russ. Chem. Rev.* ***2000,*** 69, (1), 81-94.

10. Chapela, V. M.; Parry, G. S., Intercalation of amino acids and polypeptides into 2H-TaS_2. *Nature* ***1979,*** 281, 134-135.

11. Teghi, R.; De Beonis, A.; Galasso, A.; Santagata, A.; Villani, P.; J., J. D., Role and importance of nanoparticles in femtosecond pulsed laser ablation deposition of Al-Cu-Fe quasicrystal. *Chem. Phys. Lett.* ***2007,*** 438, (1-3), 85-88.

12. Jia, T. Q.; Chen, H. X.; Huang, M.; Wu, X. J.; Zhao, F. L.; Baba, M.; Suzuki, M.; Kuroda, H.; Qiu, J. R.; Li, R. X.; Xu, Z. Z., ZnSe nanowires grown on the crystal surface by femtosecond laser ablation in air. *Appl. Phys. Lett.* **2006,** 89, 101116-1 - 101116-3.

13. Tull, B. R.; Carey, J. E.; Sheehy, M. A.; Friend, C.; Mazur, E., Formation of silicon nanoparticles and web-like aggregates by femtosecond laser ablation in a background gas. *Appl. Phys. A* **2006,** 83, 341-346.

14. Yasumaru, N.; Miyazaki, K.; Kiuchi, J., Fluence dependence of femtosecond-laser-induced nanostructure formed in TiN and CrN. *Appl. Phys. A* **2005,** 81, 933-937.

15. Zeng, X.; Mao, X. L.; Greif, R.; Russo, R. E., Experimental investigation of ablation efficiency and plasma expansion during femtosecond and nanosecond laser ablation of silicon. *Appl. Phys. A* **2005,** 80, 237-241.

16. Furusawa, H.; Sakka, T.; Ogata, Y. H., Characterization of ablated species in laser-induced plasma plume. *J. Appl. Phys.* **2004,** 96, (2), 975-982.

17. Parilla, P. A.; Dillon, A. C.; Jones, J. G.; Riker, G.; Schulz, D. L.; Ginley, G. S.; Heben, M. J., The first true inorganic fullerenes? *Nature* **1999,** 397, 114.

Chapter 5: Tin Sulfide Nanowires Prepared From Single Source Precursors

Prepared for publishing: K. Y. Chick, Manashi Nath and B. A. Parkinson

5.1 Abstract

The present paper reports a facile route to produce tin sulfide, SnS, one-dimensional (1-D) nano-structures. The synthesis is a direct one-pot method carried out by heating the single source precursor, tetrakis-(*N, N*-diethyldithiocarbamato)tin(IV), in a mixture of long-chain alcohol (tergitol and diethylene glycol). Reaction parameters, such as temperature and the duration of the reaction, have been investigated for their effect on yield and nanostructure morphology. The as-produced nanostructures were characterized with scanning electron microscopy (SEM), energy dispersive x-ray analysis (EDX), transmission electron microscopy (TEM), selected-area electron diffraction (SAED) and powder x-ray diffraction (XRD).

5.2 Introduction

Tin sulfide (SnS), also known as Herzenbergite, is a IV-VI p-type semiconductor.[1,2] SnS consists of layers stacked along the *b*-axis where within the layer: each tin atom is coordinated to three sulfur atoms while each sulfur atom is bonded to three tin atoms. The SnS layers are held together by weak van der Waals forces, resulting in a larger interatomic distance along the (001) plane. The high-temperature phase of SnS is the orthorhombic phase (with lattice parameter of a=0.432, b=1.121, and c=0.399), which is the GeS type structure with space group *Pnma*. In the orthorhombic phase, there are two SnS layers in one unit cell. Each tin atom is coordinated to two sulfur atoms that are in plane with the layer and to one other sulfur atom is at a short distance perpendicular to the plane of the same layer [Figure 5.1]. The lower temperature, less common, phase of SnS has a monoclinic structure.[3] Other phases such as the unusual zinc blende (ZnB) structures have also been observed for SnS.[4]

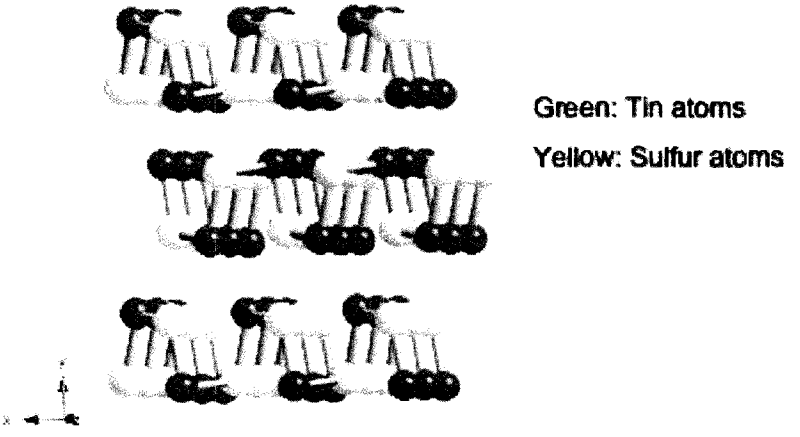

Figure 5.1 The layered-structure of SnS orthorhombic phase

SnS is an inexpensive, nontoxic and stable material that is useful for many applications. SnS is useful in solar photovoltaic energy conversion due to the indirect band gap of 1.08 eV and the direct band gap of 1.30 eV.[1,5,6] SnS has been tested as a Li-insertion material for an anode for the rechargeable Li batteries.[7] SnS can also be used in the environmental industry as sensors, in holographic recording systems, and electrical switching devices.[8]

It is well-known that inorganic materials with different morphologies can exhibit different electrical and chemical properties.[9,10] Electrical and chemical properties of 1-D structures, such as nanowires, nanobelts, nanorods and nanotubes, differ from other nanostructures, such as nanospheres, due to the anisotropy of the structure.[9,10] The 1-D structures are desirable due to the important role that they have as interconnects and functional components in the fabrication of nanoscale electronic and optoelectronic devices. The goal of this paper is to provide a facile route to produce 1-D nanostructures of SnS.

There has been considerable previous research on SnS synthesis. For example, thin SnS films have been synthesized by spray pyrolysis.[11] SnS nanoparticles have been prepared by refluxing tin and sulfur in diglyme,[12] solvothermal decomposition of a single source precursor[13] or by the solution dispersion method.[14] SnS nanoflowers have been prepared by thioglycollic acid-assisted hydrothermal synthetic method.[15] SnS nanoflakes have been produced by a microwave-assisted synthesis method.[7] Belt-like SnS micro-size crystals have been synthesized from tin (II) chloride/sulfur/ethylenediamine solution.[1] Urchain-like SnS

nanostructures have been synthesized via the solvothermal methods.[2] SnS nanowires have also been grown by surfactant-assisted synthesis.[16] And finally, nano-tetrahedra of the rare zinc blende (ZB) phase of SnS have been produced by thermally decomposing tin chloride and elemental sulfur in a primary amine solvent.[4]

Single source precursors, such as the cage-ring structure organotin precursors,[17] dithiocarbamates,[18] thiadiazoles,[19] and phenylated ring systems,[20,21] have been reacted to prepare SnS materials through thermal decomposition. Such compounds are easy to use since no other reactant is required throughout the reaction, and thus, there are fewer parameters to adjust to optimize the reaction. Better control of the synthesis process could be achieved. Furthermore, in most cases of single-source precursors, lower reaction temperatures are needed when compared to other conventional methods. Despite the advantages of employing single-source precursors, research has been mainly focused on the preparation of bulk SnS films. There has been little research into synthesizing other SnS morphologies using a single-source precursor.

In this paper, a facile, one-pot method to produce SnS 1-D nanostructures is presented. That uses a single-source precursor, tin(IV) diethyldithiocarbamate, in the presence of mixture of solvents (tergitol and diethylene glycol). Different SnS nanostructures were prepared by variation of the synthetic conditions and were characterized by several analytical techniques.

5.3 Experimental

All chemicals were used as received without further purification. Sodium diethyldithiocarbamate trihydrate (98%), tin (IV) tetrachloride pentahydrate (98%) were obtained from Alfa Aesar. Absolute ethanol, tergitol 15-S-5, diethylene glycol (98%) and methylene chloride were from AAPER Alcohol and Chemical company, Dow chemicals, Sigma Aldrich, and Fisher Scientific respectively.

Copper TEM grids, with Formvar as the support film, were purchased from Ted Pella, Inc. TEM was carried out on JEOL 2000 TEM, operating at an accelerating voltage of 160 kV. SEM was carried out on JEOL JSM-6500F, operating at an accelerating voltage of 15 KV. Powder X-ray diffraction (XRD) of the as-produced samples was carried out on Brüker D-8 Discover x-ray diffractometer (Cu Kα radiation) with a Göbel mirror on the primary beam side and a scintillation detector on the diffracted beam side. The angle of incidence was 0.5° and the measurements were performed with soller slits. High-resolution (HR) TEM was also carried out on Philips CM200 TEM (with an accelerating voltage of 200 kV) located at Colorado School of Mines.

Synthesis of tetrakis-(N, N-diethyldithiocarbamato)tin(IV) {$Sn[(C_2H_5)_2NCS_2]_4$} [also known as $Sn(dedtc)_4$][Figure 5.2]:

$Sn(dedtc)_4$ was synthesized using the procedure previously been reported.[22] The chemical reaction for obtaining $Sn(dedtc)_4$ can be written as,

$$4Na(C_2H_5)_2NCS_2 + SnCl_4 \rightarrow Sn[(C_2H_5)_2NCS_2]_4 + 4NaCl \qquad \text{[Equation 5.1]}$$

In a typical synthesis, sodium diethyldithiocarbamate trihydrate $[Na(C_2H_5)_2NCS_2 \cdot 3H_2O]$ [Na(dedtc) · $3H_2O$] (1.9336g, 8.5820 mmol) and tin (IV) tetrachloride pentahydrate ($SnCl_4 \cdot 5H_2O$) (0.3874g, 1.105 mmol) were each dissolved in 25 mL and 10 mL of ethanol respectively. The Na(dedtc) solution was then added dropwise into the $SnCl_4$ solution under stirring, a yellow precipitate of $[Sn(dedtc)_4]$ was immediately formed. The precipitate was filtered and washed with several aliquots of water. The product was dried in the vacuum oven at 60 °C for at least 3 hours to ensure the complete removal of solvent. The final product $[Sn(dedtc)_4]$ was characterized by melting point, nuclear magnetic resonance spectroscopy (NMR), and thermogravimetric analysis (TGA).

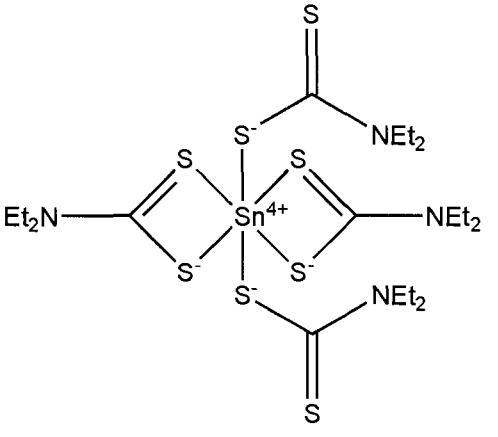

Figure 5.2 Structure of Tetrakis-(*N, N*-diethyldithiocarbamato)tin(IV)

This single source precursor, which provides both tin and sulfur sources for the synthesis, was chosen due to its facile preparation procedure, which can be

performed in the ambient atmosphere. $Sn(dedtc)_4$ is also a moisture and air stable material which can be stored for months.

Synthesis of the 1-D SnS structures:

In a typical procedure, the single source precursor [$Sn(dedtc)_4$] was added twice during the reaction process. Two solvents (tergitol and diethylene glycol) were employed for the reaction. In the reflux apparatus, 10 mL of tergitol (the primary solvent) was heated in the sand-bath to 290 °C, while $Sn(dedtc)_4$ (0.0740 g, 0.105 mmol) was sonicated in 2.2 mL (23.18 mmol) of diethylene glycol (DEG, the secondary solvent). The yellowish dispersion of $Sn(dedtc)_4$ was added dropwise into tergitol and the color of the tergitol turned brown at 290 °C. A dark brown precipitate was observed immediately after the addition. Three hours after the first addition, the second aliquot of precursor dispersion [$Sn(dedtc)_4$ (0.0750 g, 0.105 mmol) in 2.2 mL (24.23 mmol) of DEG] was added to the mixture, that was further heated for 12 hours at 350 °C. After the reaction, the color of the reaction mixture changed to black, while a dark brown precipitate remained in the mixture. The precipitate was filtered and washed several times with methylene chloride and ethanol in order to remove any soluble by-products and solvents.

The investigations of reaction parameters:

Several reactions were carried out with slight variations of the reaction parameters. These variations were focused optimizing the yield of 1-D SnS nanostructures. The following parameters were varied: (a) Single source precursor [$Sn(dedtc)_4$] concentration; (b) the addition temperature; (c) the secondary solvent,

and (d) the reaction duration. See Table 5.1 and 5.2 for a summary of reaction parameters used (Reactions #1-9).

The separation (/purification) procedures of the as-produced nanostructures:

Attempts to separate the different nanostructures from the product used the following procedures: after the washing sequences (using methylene chloride and ethanol), the products (in ethanol) were first sonicated for 1 minute, and allowed to settle for 2 minutes. The top portion of the aliquot was then separated from the bottom portion. The separation procedure was repeated at least 3 times. Each portion of the sample was examined by SEM.

Table 5.1 The summary of precursor concentration, and addition temperatures for the reactions.

Reaction #	$Sn(dedtc)_4$ 1st addition (mmol)	Tergitol volume	DEG volume	1st addition temperature* (+/- 5 °C)
1	0.104	10 mL	2.2 mL	310 °C
2	0.206	10 mL	2.2 mL	300 °C
3	0.248	5 mL	2.2 mL	300 °C
4	0.106	10 mL	2.2 mL	230 °C
5	0.104	10 mL	2.2 mL	306 °C
6	0.104	10 mL	2.2 mL	342 °C

*Note: the addition temperature here referring to the temperature at which the first portion of the tin precursor colloid was added.

Table 5.2 The reaction summary of the secondary solvent effect.

Reaction #	$Sn(dedtc)_4$*	Tergitol volume	Secondary surfactant/volume
7	0.372 mmol	3 mL	Tergitol/2.8 mL
8	0.343 mmol	3.2 mL	Diethylene glycol (DEG)/2.0 mL
9	0.347 mmol	3 mL	Ethylene glycol (EG)/2.0 mL

*Note: the calculation is based on the Sn(dedtc)4 molecular weight of 711g/mol.

5.4 Results and discussion

The $Sn(dedtc)_4$ has an interesting structure, as shown in Figure 5.2. It contains two bidentate and two monodentate dithiocarbamate ligands. The melting point of the vacuum oven-dried yellow product was in agreement with its literature value (162 °C).[22] Chemical shifts obtained from the ^{13}C NMR spectrum (198.4, 49.7 and 12.1 ppm.) were comparable to the reported values (198.4, 49.6 and 11.9 ppm).[23] ^{1}H NMR indicated that two major hydrogen types can be observed: a triplet at 1.268 ppm and a quartet 3.8 ppm (a 3:2 ratio). TGA was performed under a He atmosphere. Two-step decomposition was observed with an onset temperature at 169 °C [Figure 5.3]. The TGA spectrum is similar to the reported results.[24] The slight difference between the literature value and the collected data could be due to the heating rate, and the nature of purging gas. The powder after the TGA was examined by XRD, which indicated that SnS_2 was produced from heating the precursor in a He atmosphere.

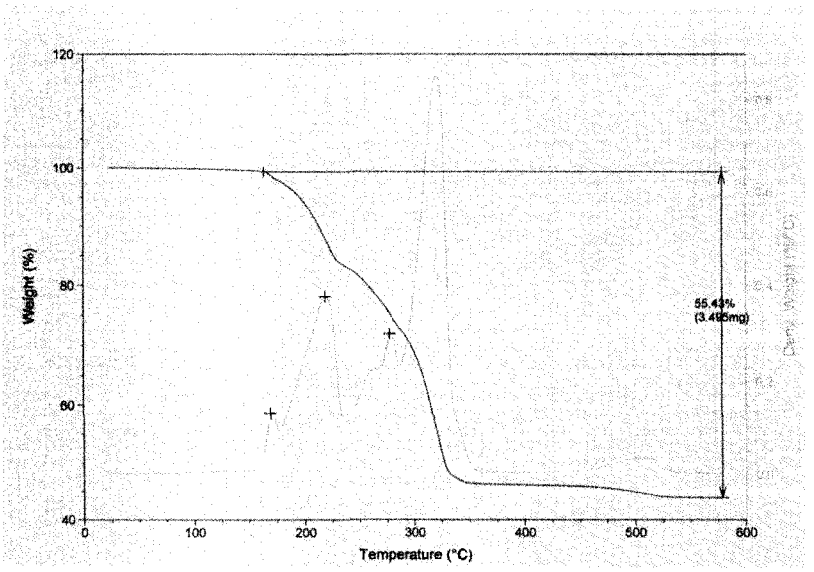

Figure 5.3 TGA results of $Sn(dedtc)_4$ under He atmosphere.

SEM images revealed the typical products from the reflux reactions. A majority of the product was urchin-like one-dimensional structures [Figure 5.4]. The as-produced samples were not morphologically monodisperse and varied as a function of the reaction parameters. Both nanowire [Figure 5.5] and ribbon-like 1-D structures [Figure 5.6] were found within the same sample, along with bulk materials. The dimensions of these nanostructures were also not monodisperse. The diameters of the 1-D structures ranged from 10 nm up to micron size. These structures were all longer than about 10 microns. EDX in the SEM indicated that all structures contained Sn and S with a ratio close to 1:1. Contaminants, such as carbon and oxygen, were found as well. In some cases, other crystalline structures, such as tetrahedral or other polyhedral micro- or nanocrystals [Figure 5.7] were also found within the sample.

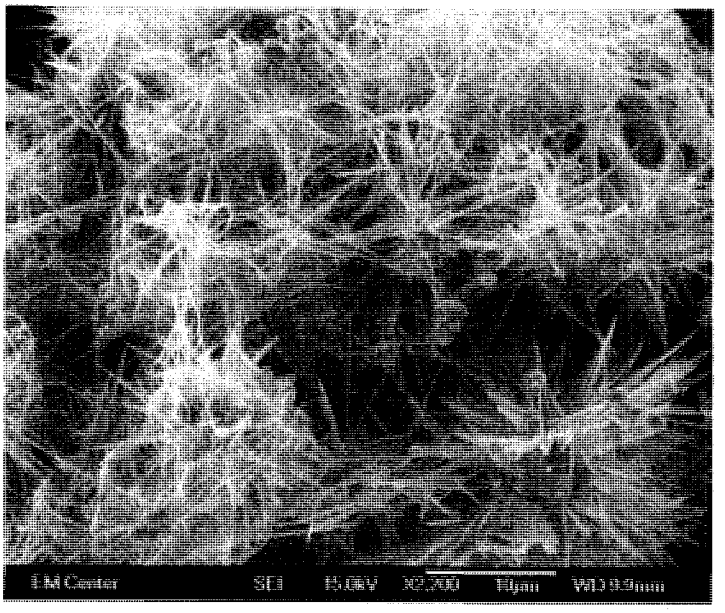

Figure 5.4 The SEM image of the SnS product (after wash) reveals the overall yield.

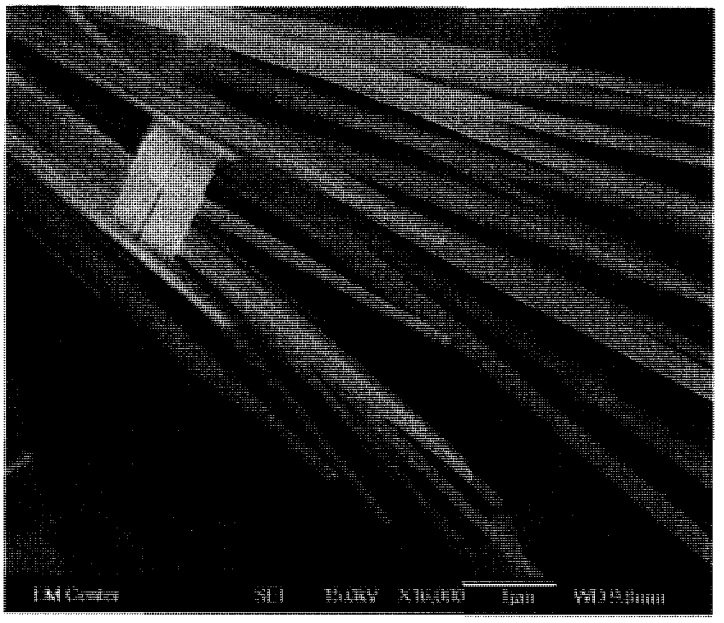

Figure 5.5 SEM image of a bundle of SnS nanowires.

Figure 5.6 SEM image of the ribbon-like structures.

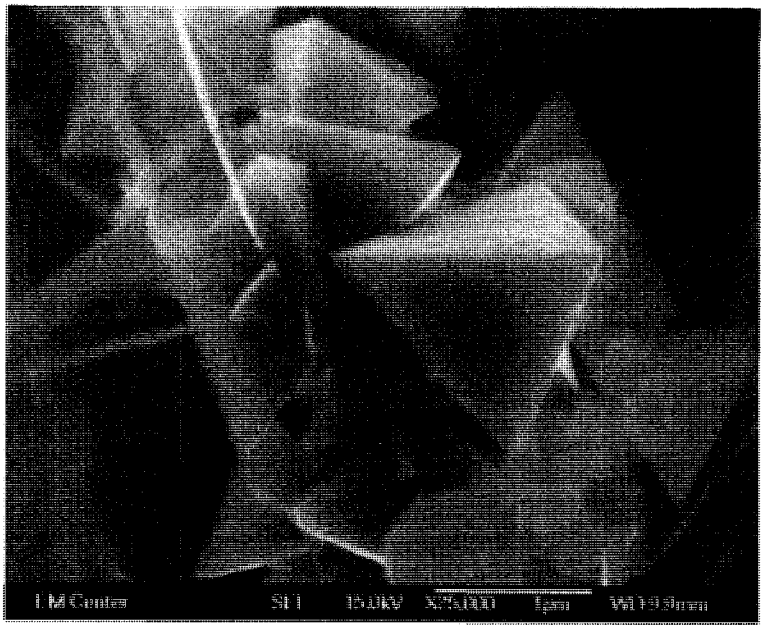

Figure 5.7 SEM image of tetrahedral micron size crystals.

High magnification TEM images also revealed a variety of nanostructures. Surfaces of these structures were not completely smooth due to particulate deposits on the surface. SAED patterns could be obtained from several nanowires as shown in Fig. 5.8. The SAED patterns confirmed the presence of SnS orthorhombic phases, and the diffraction spots could be indexed to (101), (200) lattice planes. HR-TEM images of the SnS 1-D nanostructures were also obtained [Figure 5.9]. Uniform lattice fringes were observed in the 1-D nanostructures, with spacing close to 2.8 Å, corresponding to the (111) lattice planes of the orthorhombic SnS phase. The uniform lattice fringes indicated these nanostructures were single crystalline.

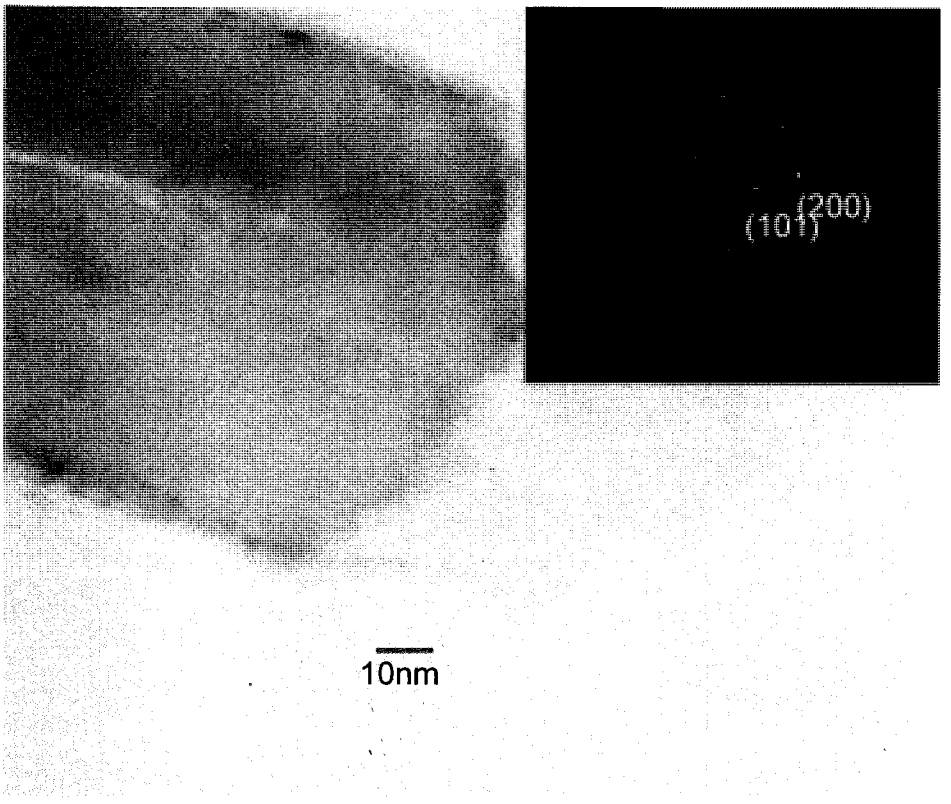

Figure 5.8 TEM image of the SnS 1-D nanostructure. Insert: the corresponding SAED pattern.

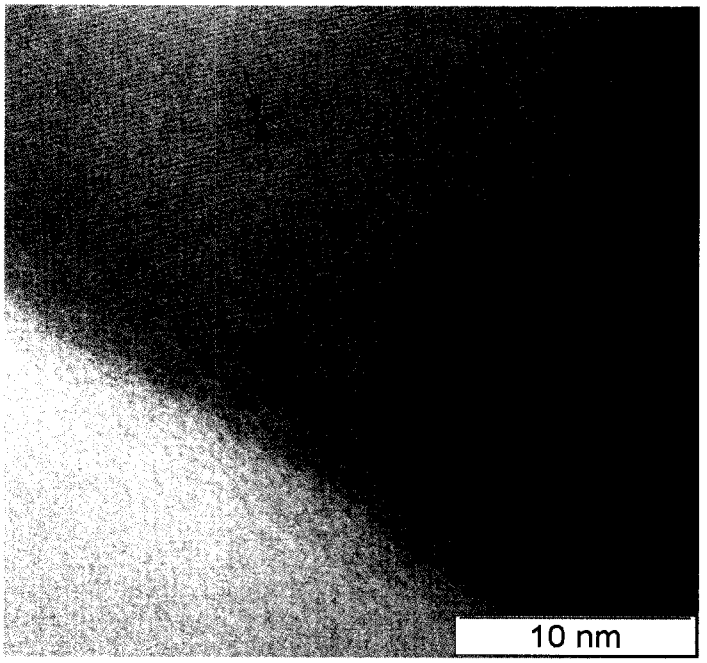

Figure 5.9 HR-TEM image of SnS 1-D nanostructure.

XRD data was also collected on the as-produced nanostructures. Figure 5.10 shows a typical XRD data. A mixture of two SnS polymorphs, orthorhombic (JCPDS Cards No. 39-354) and zinc-blende,[4] were found among the products. The orthorhombic phases of SnS, are the most commonly seen among the SnS phases. The zinc blende phase, on the other hand, is an unusual SnS structure, and has only been reported few times.[4,25] Greyson *et al.* suggested the zinc-blende structure can be obtained at lower temperature, while the orthorhombic structure is thermodynamically stable. Both SEM and XRD results depict that the polyhedra [Figure 5.7] in the product are the zinc-blende structures; while most of the 1-D

structures were orthorhombic in phase. Further purification of sample will allow the confirmation of the identity of the monodisperse polyhedra.

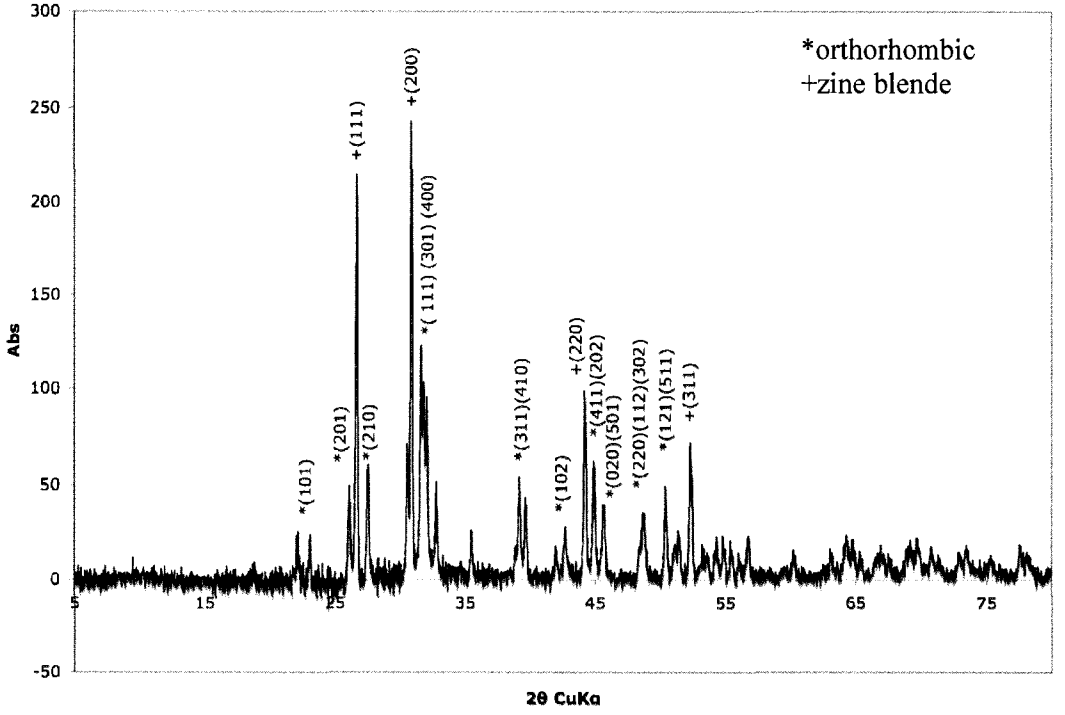

Figure 5.10 XRD confirmed the mixture of SnS polymorphs: *orthorhombic and +zinc blende.

Variation of reaction parameters allows the elucidation of the growth mechanism. Several reaction parameters have been adjusted, as mentioned in the previous section. The product morphologies for each reaction were summarized in Table 5.3, which indicated that the reaction parameters contribute to the formation of different morphologies of the SnS materials.

Table 5.3 Summary of the product morphologies when reaction parameters were varied.

Reaction #	Product morphologies
1	Nanoflowers, and 1-D nanostructures
2	Nanoflowers, 1-D nanostructures, tetrahedral crystals, and bulk
3	Nanoflowers, spindles, and spheres-like nanoparticles
4	Nanoflowers, and sphere-like nanoparticles
5	Nanoflowers, 1-D nanostructures, sphere-like nanoparticles, and bulk
6	Micron-size needles, and bulk
7	Sphere-like nanoparticles, and spindles-like nanoparticles
8	Nanoflowers, sphere-like nanoparticles, and short 1-D structures
9	Nanoflowers, and sphere-like nanoparticles

(The results of Table 5.1, and Table 5.2).

Reactions # 1-3 from Table 5.3 demonstrated the effect of single source precursor concentration, using tergitol as the primary solvent. The concentration of $Sn(dedtc)_4$ was varied by either changing the amount of $Sn(dedtc)_4$ or by changing the volume of tergitol. The reactions were carried out as described in the general synthesis procedures, by adding the precursors twice into the same reaction mixture. The precursor concentration for the first addition, however, controls the initial nucleation and growth step, and thus determines the morphologies of the final products. As a result, the first addition was more critical than the second one.

In the case of reaction #1, when the initial precursor concentration was lower, 1-D structures were observed as the dominant morphology. In reaction #2, 1-D structures still remained as the primary products, despite increasing the initial precursor concentration. In reaction #3, however, the result was very different, the

long, 1-D structures seen in reaction #1 and #2 were no longer found. Instead, small amounts of short, spindle-like nanoparticles were observed. It is important to note that the yield of the 1-D structures was higher in reaction #1 than reaction #2, as they are the majority of the products, with fewer side-products (such as bulk of SnS). One can speculate that more controlled-growth was allowed with the lower concentration, and therefore, more monodisperse morphologies of SnS materials resulted. Figure 5.11 exhibits the general morphology trend with precursor concentration.

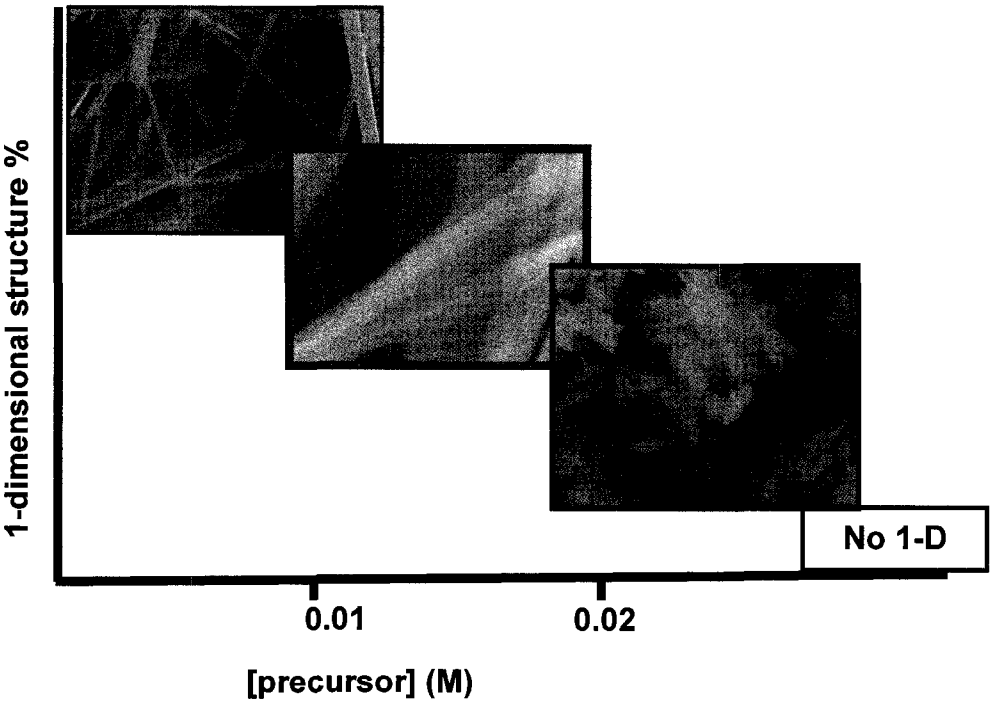

Figure 5.11 Plot of 1-D structures vs. precursor concentration. Lower concentration yields higher percentages of 1-D structures (in green and orange boxes). With the increasing concentration, however, only materials without 1-D structures or spindle-like structures (in purple box) were generated. (The pictures do not reflect the actual size of the nanostructures).

The addition temperature was also found to play an essential role in the synthesis of 1D structures. The addition temperature as referred here is the temperature at which the first portion of the single source precursor dispersion was added. Three different addition temperatures, between 230 to 340 °C, were used, as the temperature of the second additions for all reactions remained the same (at around 350 °C). See Table 5.1 (Reactions #4-6) for a summary of the reaction parameters. When the addition temperature is lower (Reaction #4, at 230 °C), only sphere-like and nanoflower shaped particles were found. With the appropriate temperature (Reaction #5, at 310 °C), nanowires and other structures could be formed. As the addition temperature increased (Reaction #6, at 340 °C), however, only larger size micro-needles and bulk material were produced.

The addition temperature served two purposes in this reaction: (1) to decompose the tin single source precursor, (b) to control the temperature of initial nucleation and growth. When the initial nucleation temperature was too low, the commonly-seen sphere-like nanoparticles (Reaction #4) resulted. When the addition temperature was too high, rapid decomposition of the precursors and rapid growth of the nanostructures promotes the growth of more thermodynamically stable micron-size needles and bulk materials (Reaction #6). Only an intermediate addition temperature provided the appropriate reaction environment for the nucleation and growth of the desired 1-D nanostructures (Reaction #5).

The role of secondary solvent in the reaction was also investigated. Three different solvents were used as the secondary surfactant: DEG, tergitol, and ethylene

glycol (EG) (Table 5.2, Reactions #7-9). The reactions were simplified to a one-time addition, and the volume of primary surfactant was reduced to 3 mL. All three reactions employed the same addition temperature (310 °C). Only DEG yielded some short, 1-D nanostructures (Reaction #8). It is believed that the secondary solvent does not dissolve the single source precursor [$Sn(dedtc)_4$], but after sonication transfers precursor to the tergitol. During the addition, the temperature of the reaction mixture can be reduced as the result of adding the secondary solvent to the mixture. Depending on the nature of the secondary solvent, the impact on the temperature of the reaction mixture varies. For example, by adding the DEG to the hot tergitol, the temperature drop of the resulting mixture is less (when compared with EG as the secondary solvent). As a result, the temperature of reaction mixture with DEG can support the decomposition and initial nucleation of the 1-D structures, whereas with EG the temperature is too low to sustain the initial nucleation of the 1-D structure.

Finally, the effect of the duration of the reaction was investigated. A comparison of the reflux time was done for each reaction. To monitor the products throughout the reaction, several aliquots were withdrawn from the sample at different time periods throughout the reaction time. The 1st aliquot was usually withdrawn 30 min after the 1st addition of the single source precursor. Generally speaking, nanoflowers or needle-like small particles already appeared in the 1st aliquot sample. As the reaction proceeded, the amount of nanoflowers decreased, and the number of sphere-like particles and bulk materials increased. Interestingly, the amount of 1-D structures, remained almost unchanged throughout the reaction. The size of those 1-

D structures, however, increased (in both length and diameter) during the reaction. It was found that a reaction duration of between 6 and 12 hours yielded the best results where the 1-D nanostructures had higher aspect ratios, where the diameter approached 0.5 microns as the upper limit.

The overall growth mechanism is proposed to be as follows: the precursor, $Sn(dedtc)_4$, is first dispersed by the secondary surfactant, DEG. The role of DEG is to transfer the precursor into the hot-tergitol-environment and to support the appropriate reaction temperature. The precursor then decomposes, nucleates, and forms the nanoflower-like particles and the 1-D structures of SnS. The nanoflowers are not the stable structure. The re-dissolution of the nanoflower-like particles therefore takes place, which acts as the source for further growth of other 1-D nanostructure. The growth of the nanostructures continued with the second addition of precursors, until all sources material was consumed to form 1-D structures, sphere-like structures and bulk materials.

5.5 Conclusion

A facile, one-pot synthesis of 1-D SnS nanostructures has been achieved. The dependence of the product morphology on the various reaction parameters such as concentration, temperature and duration has also been investigated. Morphologies other than nanowires, such as nanoflowers and nanospheres have also been obtained. The question on how to gain control in the nanostructure assembly so that the size or the shape can be tailored-made still remains as an open question. More investigations are necessary in order to gain more understanding on the synthesis procedure to get better reaction control.

Reference:

1. An, C. H.; Tang, K. B.; Shen, G. Z.; Wang, C. R.; Yang, Q.; Hai, B.; Quan, Y. T., Growth of belt-like SnS crystals from ethylendiamine solution. *J. Cryst. Growth* **2002,** 244, 333-338.

2. Hu, H. M.; Yang, B. J.; Zeng, J. H.; Qian, Y. T., Morphology evolution of SnS nanocrystals: from 3D urchin-like architectures to 1D nanostructures. *Mater. Chem. Phys.* **2004,** 86, 233.

3. Rajagopalan, M.; Kalpana, G.; Priyamvadha, V., Pressure induced structural phase transition in SnS-An ab initio study. *Bull. Mater. Sci.* **2006,** 29, 25-28.

4. Greyson, E. C.; Barton, J. E.; Odom, T. W., Tetrahedral zinc blende tin sulfide nano and microcrystals. *Small* **2006,** 2, 368-371.

5. Niinobe, D.; Wada, Y., Controlled deposition of SnS into/onto SnO_2 nano-particle film and application to photoelectrochemical cells. *Bull. Mater. Sci. Jpn.* **2006,** 79, (3), 495-497.

6. Johnson, J. B.; Jones, H.; Latham, B. S.; Parker, J. D.; Engelken, R. D.; Barber, C., Optimization of photoconductivity in vacuum-evaporated tin sulfide thin films. *Semicond. Sci. Technol.* **1999,** 14, (6), 501-507.

7. Patra, C. R.; Odani, A.; Pol, V. G.; Aurbach, D.; Gedanken, A., Microwave-assisted synthesis of tin sulfide nanoflakes and their electrochemical performance as Li-inserting materials. *J. Solid State Electrochem.* **2007,** 11, 186-194.

8. Parenteau, M.; Carlone, C., Influence of temperature and pressure on the electronic transitions in SnS and SnSe semiconductors. *Phys. Rev.* **1990,** B41, 5227.

9. Xia, Y. N.; Yang, P. D.; Sun, Y. G.; Wu, Y. Y.; Mayers, B.; Gates, B.; Yin, Y. D.; Kim, F.; Yan, H. Q., One-dimensional nanostructures: synthesis, characterization, and applications. *Adv. Mater.* **2003,** 15, (5), 353-389.

10. Yu, S.; Wu, Y.; Yang, J.; Han, Z.; Xie, Y.; Qian, Y., A novel solventothermal synthetic route to nanocrystalline CdE (E= S, Se, Te) and morphological control. *Chem. Mater.* **1998,** 10, 2309-2312.

11. Devika, M.; Ramakrishna Reddy, K. T.; Koteeswara Reddy, N.; Ramesh, K.; Ganesan, R.; Gopal, E. S. R.; Gunasekhar, K. R., Microstructure dependent physical properties of evaporated tin sulfide films. *J. Appl. Phys.* **2006,** 100, 0 23518.

12. Schlecht, S.; Kienle, L., Mild solvothermal synthesis and TEM investigation of unprotected nanoparticles of tin sulfide. *Inorg. Chem.* **2001,** 40, 5719-5721.

13. Koktysh, D. S.; McBride, J. R.; Rosenthanl, S. J., Synthesis of SnS nanocrystals by the solvothermal decomposition of a single source precursor. *Nanoscale Res. Lett.* **2007,** 2, 144-148.

14. Zhao, Y. B.; Zhang, Z. J.; Dang, H. X.; Liu, W. M., Synthesis of tin sulfide nanoparticles by a modified solution of dispersion method. *Mater. Sci. Eng., B* **2004,** 113, 175-178.

15. Zhu, H. L.; Yang, D.; Zhang, H., Hydrothermal synthesis, characterization and properties of SnS nanoflowers. *Mater. Lett.* **2006,** 60, 2686-2689.

16. Panda, S. K.; Datta, A.; Dev, A.; Gorai, S.; Chaudhuri, S., Surfactant-assisted synthesis of SnS nanowires grown on tin foils. *Cryst. Growth Des.* **2006,** 6, (9), 2177-2181.

17. Costa, G. A. A.; Silva, M. C.; Silva, A. C. B.; de Lima, G. M.; Lago, R. M.; Sansiiero, M. T. C., Thermal decomposition of sulfur-containing organotin molecular precursors to produce phase-pure SnS. *Phys. Chem. Chem. Phys.* **2000,** 2, 5708-5711.

18. Menezes, D. C.; de Lima, G. M.; Porto, A. O.; Donnici, C. L.; Arisson, J. D.; Doriguetto, A. C.; Ellena, J., Synthesis, characterization and thermal decomposition of tin(IV) diethiocarbamate derivative-single source precursors for tin sulfide powders. *Polydehdron* **2004,** 23, 2103-2109.

19. M. Nath, S., Di- and triorganotin (IV) derivatives of 5-amino-3H-1,3,4-thiadiazole-2-thione as precursors or SnS/SnO_2: thermal studies and related kinetic parameters. *Mater. Res. Bull.* **2006,** 41, 78-91.

20. Bahr, S.; Boudjouk, P.; McCarthy, G. J., Tin-sulfur and tin-selenium phenylated ring systems as organometallic precursors to tin sulfide and tin selenide. *Chem. Mater.* **1992,** 4, 383-388.

21. Boudjouk, P.; Seidler, D. J.; Bahr, S.; McCarthy, G. J., Bis(tripheyltin) chalcogenides as convenient precursors to phase-pure binary semiconductors. *Chem. Mater.* **1994,** 6, 2106-2112.

22. Harreld, C. S.; Schlemper, E. O., The crystal and molecular structure of tetrakis-(N, N-diethyldithiocarbamato) tin (IV)). *Acta. Cryst.* **1971,** B27, 1964.

23. van Gaal, H. L. M.; Diesveld, J. W.; Pijpers, F. W.; van der Linden, J. G. M., ^{13}C NMR spectra of dithiocarbamates. Chemical shifts, carbon-nitrogen stretching vibration frequencies, and pi bonding in the NCS2 fragment. *Inorg. Chem.* **1979,** 18, (11), 3251-3260.

24. Bratspies, G. K.; Smith, J. F.; Hill, J. O., A thermogravimetry/differential thermal analysis and pyrolysis/gas chromatography-mass spectrometry study of several tin(IV) dithiocarbamate complexes in an air atmosphere. *Thermochimica Acta.* **1977,** 19, 373-382.

25. Badachhape, S. B.; Goswami, A., Structure of evaporated tin sulfide. *J. Phys. Soc. Jpn.* **1962,** 17(Supp. B-II), 251-253.

Chapter 6. Synthesis Of One-dimensional Structures Of Tin Oxide Via Pyrolysis Reactions

Prepared for publishing: K. Y. Chick, Manashi Nath, and B. A. Parkinson

6.1 Abstract

One-dimensional (1-D) nanostructures of the rutile phase of SnO_2 has been synthesized on a gold-coated silicon wafers by the one-step low temperature pyrolysis of single source precursor, tetrakis-(*N, N*-diethyldithiocarbamato)tin(IV) $[Sn[(C_2H_5)_2NCS_2]_4]$. The nanostructures were characterized by scanning electron microscopy (SEM), X-ray diffraction (XRD), and transmission electron microscopy (TEM). The results indicate that these 1-D nanostructures of SnO_2 have single crystal domains at least several tens of microns long. Several experimental parameters, including reaction duration, reaction temperature, substrate identity, and single source precursor, were varied in order to elucidate the growth mechanism and optimize the yield of the 1-D structures. It is proposed that the resulting 1-D growth follows a vapor-liquid-solid (VLS) mechanism.

6.2 Introduction

Nanomaterials are key elements in the development of nanotechnology. It is known that different nanomaterial geometries, such as one-dimensional (1-D) nanostructures (nanowires, nanotubes and nanobelts), can exhibit unique properties. 1-D nanostructures are of interest due to their dimensionality that are desirable for applications.[1-3] Various synthetic methods have been utilized to generate 1-D nanostructures, such as template methods,[4-6] solution phase synthesis,[7,8] and gas-phase methods.[9-11] In the case of gas-phase methods, different growth mechanisms for nanostructures have been proposed, for example, the vapor-liquid-solution (VLS) mechanism.

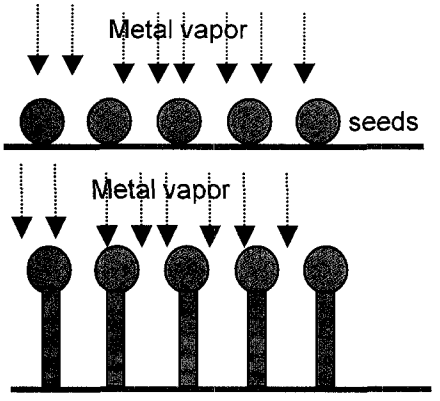

Figure 6.1 Schematic representation of the VLS mechanism. Top: metal vapor deposits and alloys with metal seeds. Bottom: Supersaturation of alloy seeds leads to the growth of 1-D structures by precipitation at the liquid-solid interface.

Proposed by Wagner in the 1960s, the vapor-liquid-solid mechanism (VLS) is one of the most widely accepted growth mechanisms for nanomaterials synthesis.

The idea behind the mechanism is to provide a liquid surface, usually a metal, that when exposed to another metal or metal precursor vapor, reacts and dissolves or alloys the other metal. When supersaturation of the liquid alloy is reached, nanowires are grown by precipitation at the solid-liquid interface [Figure 6.1].

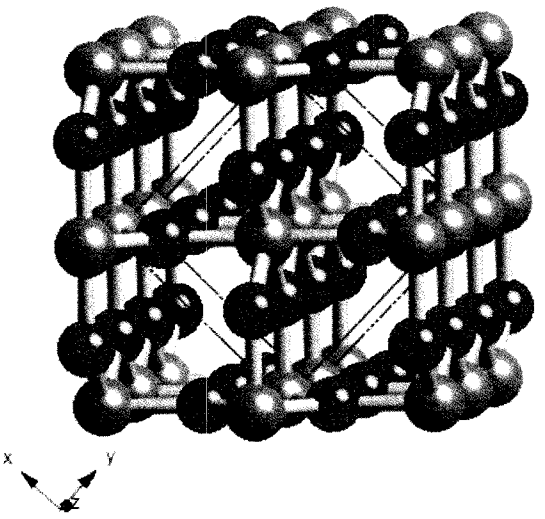

Figure 6.2 Structure of the rutile phase of SnO_2. (Blue: Ti atoms, Red: O atoms)

During the last decade, several studies suggested that the polycrystalline semiconductor metal oxides are very promising materials for the development of small dimensions of MO_X based devices, due to their sensing ability and thermal stability, as well as their low cost of production.[12,13] Tin oxide (SnO_2), for example, crystallizing in the rutile phase [Figure 6.2], is an n-type semiconductor with large band gap of 3.6 eV.[14] It is used as a transparent conducting electrode for organic light emitting diodes (OLEDs) and solar cells.[15-17] SnO_2 thin films have also been studied and used as gas sensors to detect leakage of gases, such as H_2, S, and CO, in

environmental protection, and industrial applications.[18-21] SnO_2 nanowires have the potential for various nanoelectronics applications.[22]

Various synthetic methods have been reported to prepare SnO_2 nanostructures. For example, SnO_2 nanocrystalline thin films have been grown on a *p*-InSb (111) substrate by radio-frequency magnetron sputtering with polycrystalline Sn and oxygen gas as the sources.[23] SnO_2 nanograins have been prepared by the hydrothermal reaction between $SnCl_4$ and nitric acid.[24] SnO_2 nanobelts can be prepared by evaporating the source compounds, such as SnO_2 or SnO powder,[9,25] or by heating a mixture of Sn powder and SiO_2 nanopowder in a furnace.[26] A similar heating strategy can also yield SnO_2 fishbone-like nanoribbons by heating a mixture of Sn powder and $Fe(NO_3)_3$ in a furnace.[14] SnO_2 nanorods have been prepared using molten salt synthesis.[27] SnO_2 nanowires have been fabricated by electrochemical deposition, following by thermal oxidation within an alumina membrane.[28] Polycrystalline SnO_2 nanowires have also been produced by refluxing a precursor containing Sn mixed with poly(vinylpyrrolidone) (PVP) in ethylene glycol (EG).[22]

In this paper, a simple pyrolysis route based on the VLS mechanism was employed to prepare 1-D SnO_2 nanostructures. The as-produced SnO_2 nanostructures were then characterized by different methods, including transmission electron microscopy (TEM), scanning electron microscopy (SEM), energy dispersive X-ray spectroscopy (EDX), and X-ray diffraction (XRD). The effect of different experimental parameters, such as reaction duration, reaction temperature, substrate

identity, and single source precursor, were also investigated. The growth mechanism of SnO_2 1-D nanostructures will be further discussed.

6.3 Experimental

All chemicals were used as received without further purification. Sodium diethyldithiocarbamate trihydrate (98%) and tin (IV) tetrachloride pentahydrate (98%) were from Alfa Aesar. Absolute ethanol was from AAPER alcohol and chemical CO.

Synthesis of tetrakis-(N, N-diethyldithiocarbamato)tin(IV) {$Sn[(C_2H_5)_2NCS_2]_4$} [also known as $Sn(dedtc)_4$:

$Sn(dedtc)_4$ was synthesized using the procedure previously been reported. In a typical synthesis, sodium diethyldithiocarbamate trihydrate [$Na(C_2H_5)_2NCS_2 \cdot 3H_2O$] [$Na(dedtc) \cdot 3H_2O$] (1.9336g, 8.5820 mmol) and tin (IV) tetrachloride pentahydrate ($SnCl_4 \cdot 5H_2O$) (0.3874g, 1.1050 mmol) were each dissolved in 25 mL and 10 mL of ethanol respectively. The Na(dedtc) solution was then added drop wise into the $SnCl_4$ solution under stirring, resulting in yellow precipitate [$Sn(dedtc)_4$]. The precipitate was filtered and washed with several aliquots of water. The product was dried in the vacuum oven at 60 °C for at least 3 hours to ensure the removal of solvent. The product then was recrystallized with methylene chloride in the glove box to remove trace of water. The identity of the final product [$Sn(dedtc)_4$] was confirmed by melting point, nuclear magnetic resonance spectroscopy (NMR), and thermogavimetric analysis (TGA).

Preparations of SnO_2 nanowires:

The silicon wafer was cut into 1" x 1" pieces, and was cleaned via sonication in ethanol. The cleaned Si wafer was then coated with 5 nm of Au by sputter deposition. Small amounts (4.0 mg, 5.6 μmol) of the single source precursor powder, $Sn(dedtc)_4$, was randomly loaded on the surface of the Au-coated Si wafer. The wafer with precursor powder was taken in a quartz boat and transferred to the center heating zone of a commercial furnace (Lindberg Hevi-Duty) [Figure 6.3]. The furnace was purged with ultra high purity N_2 with flow rate of 50 sccm for at least 2 hours prior to heating. The furnace temperature was then raised to 600 °C and maintined at this temperature for 1 hour under the flow of nitrogen. The furnace was then allowed to cool down to room temperature. After the reaction, the Si wafer was seen to be covered by gray powder of reacted precursor. Surrounding the reacted precursor powder was an area with a blue hue where tin oxide nanowires were found.

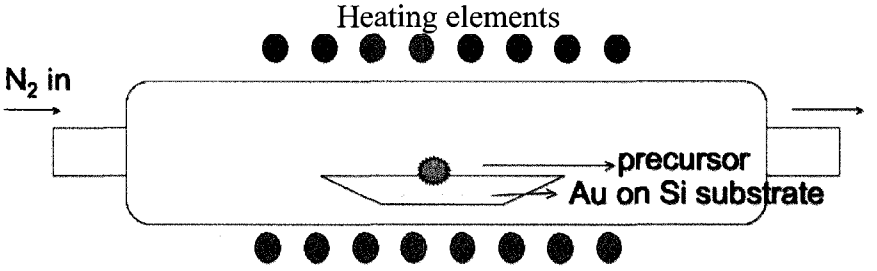

Figure 6.3 Schematic of the furnace setup.

Various experimental parameters of the pyrolysis were investigated: including reaction duration that was varied from ½ hour to 1½ hours. Furnace temperature was varied from 375 to 600 °C. Different substrates were also used, including, Si wafers

with a gold coating (the standard), Si wafers without a gold coating, Cu plates with a gold coating, and Mo plates with gold coating. Finally, the precursor was changed from $Sn(dedtc)_4$ to $SnCl_4 \cdot 5H_2O$. Table 6.1 summarized the variations of experimental parameters.

Table 6.1 Summary of reaction parameters and results.

Exp. #	Reaction Time (hr)	Substrate	Furnace temperature (°C)	Single source precursors	1-D nanostructures? (Y/N)
1	0.5	Au-Si	600	$Sn(dedtc)_4$	Y*
2	1	Au-Si	600	$Sn(dedtc)_4$	Y
3	1.5	Au-Si	600	$Sn(dedtc)_4$	Y
4	1	Au-Si	350	$Sn(dedtc)_4$	N
5	1	Au-Si	475	$Sn(dedtc)_4$	N
6	1	Au-Si	600	$Sn(dedtc)_4$	Y
7	1	Si	600	$Sn(dedtc)_4$	N
8	1	Au-Mo	600	$Sn(dedtc)_4$	Y
9	1	Au-Cu	600	$Sn(dedtc)_4$	N
10	1	Au-Si	600	$SnCl_4$	Y

In order to evaluate the role of oxygen contamination from the furnace, a similar pyrolysis experiment was carried out in a different furnace. The furnace (Thermo Electron Corporation, Lindberg blue M) located in the Prieto group was employed. Argon used in this experiment was purified by running a column containing Purification Catalyst R3-11G. The inner quartz tube liner for the furnace was thermally treated with methane to produce a carbon layer. A Au-coated Si substrate with $Sn(dedtc)_4$, as descried previously, was heated for two hours to a temperature of 600 °C, under a flow of purified argon, at a rate of 15 sccm. The

furnace temperature was held at 600 °C for 1 hour. The substrate was allowed to cool to room temperature under nitrogen flow before removing from the furnace.

The Si wafer containing the SnO_2 nanowires was characterized with SEM (JEOL JSM-6500F, operating at an accelerating voltage of 15 KV) and powder XRD (Brüker D-8 Discover x-ray diffractometer, with Cu Kα radiation) without further separation or purification. Copper TEM grids (with Formvar as the support film, from Ted Pella, Inc) were lightly tapped on the area containing the SnO_2 nanostructures in order to collect a TEM sample. TEM (JEOL 2000 TEM, operating at an accelerating voltage of 160 kV) was then carried out on the prepared Cu TEM grids. Finally, high resolution (HR-) TEM was also carried out on Philips CM200 TEM (with an accelerating voltage of 200 kV) located at Colorado School of Mines.

6.4 Results and discussion

6.4.1 General results

The XRD pattern of the area A2 was collected and indexed as the tetragonal lattice of SnO_2 (the rutile phase) in agreement with JCPDS No.41-1445 [Figure 6.4]. No obvious extra peaks were observed from the pattern, indicating that the majority product in area A2 was SnO_2. However, one of the reference XRD patterns for Si is similar to that of SnO_2. Therefore, the possibility of Si contamination of SnO_2 1-D nanostructures cannot be excluded.

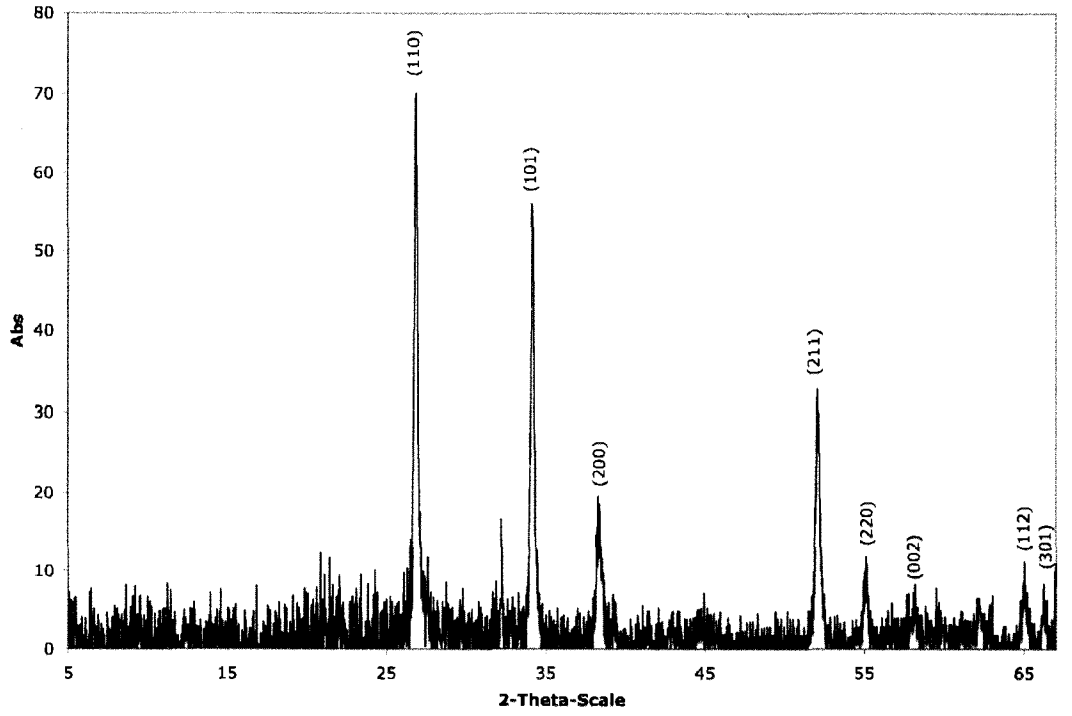

Figure 6.4 XRD pattern of material from area A2 (from Figure 6.3) indicates that the rutile phase of SnO_2.

Figure 6.5 shows a low magnification SEM image of the Si wafer after the synthesis process. Two areas (denoted as A1, and A2), containing different materials, were found on the same piece of Si wafer. Area A1 was the original location of the $Sn(dedtc)_4$ powder, appeared to be gray color after the reaction; whereas area A2 was the bare Au-coated Si substrate (free of precursor powder) before pyrolysis, and appeared to be bluish color after the reaction. Figure 6.6 shows a higher magnification SEM image of area A1. Irregular structures were found from the region containing the reacted $Sn(dedtc)_4$ powder. EDX results suggested that the structures in area A1 contained both Sn, S, with approximate atomic ratio of ~1:2.

Various amounts of carbon also were found in the sample (with no or little oxygen contamination in most cases). On the other hand, it was clear that after pyrolysis, area A2 was no longer a bare gold-coated Si substrate. The blue hue observed in area A2 indicated a coating was formed on the Si substrate. The magnified SEM image of area A2 reveals that this area was covered with 1-D nanostructures [Figure 6.7]. EDX results suggested that nanowires in area A2 consistently contained Sn and O, with the ratio of ~1: 2, and with various amounts of Si. It appears that the nanowires are SnO_2 with the Si signal coming from the substrate.

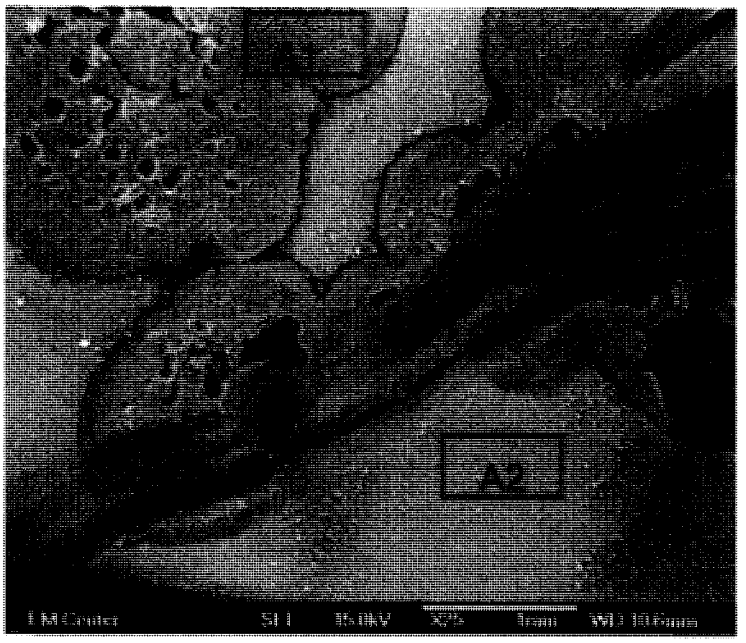

Figure 6.5 SEM image of the overall Si substrate with two distinct areas. A1: area where the single source precursor powder was loaded. A2: area where the 1-D nanostructures were found.

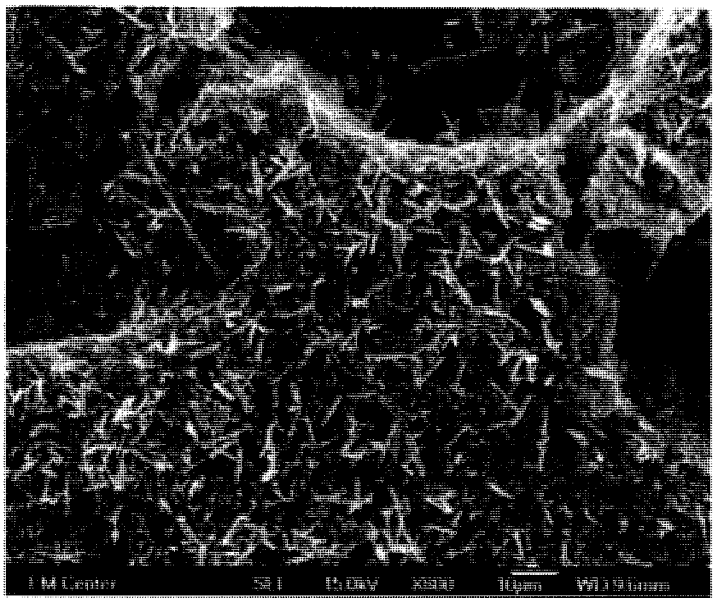

Figure 6.6 The magnified SEM image of area A1 from Figure 6.4.

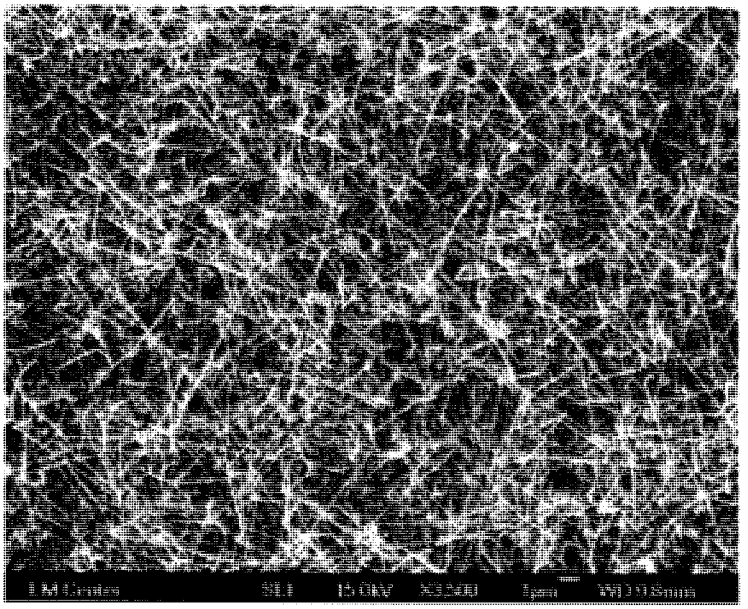

Figure 6.7 The magnified SEM image of area A2 from Figure 6.4.

The shapes of the SnO_2 1-D nanostructures varied from wires to tapered wires [Figure 6.8]. The diameters of the 1-D nanostructures ranged from 40 to 140 nm, with an average of 75 nm. The 1-D nanostructures were at least 10 μm long, but the exact lengths were not determined since they were tangled together. A different material was frequently observed at the tip of the 1-D nanostructures [Figure 6.8, green arrow]. EDX results revealed various amounts of Si and Au in such tips.

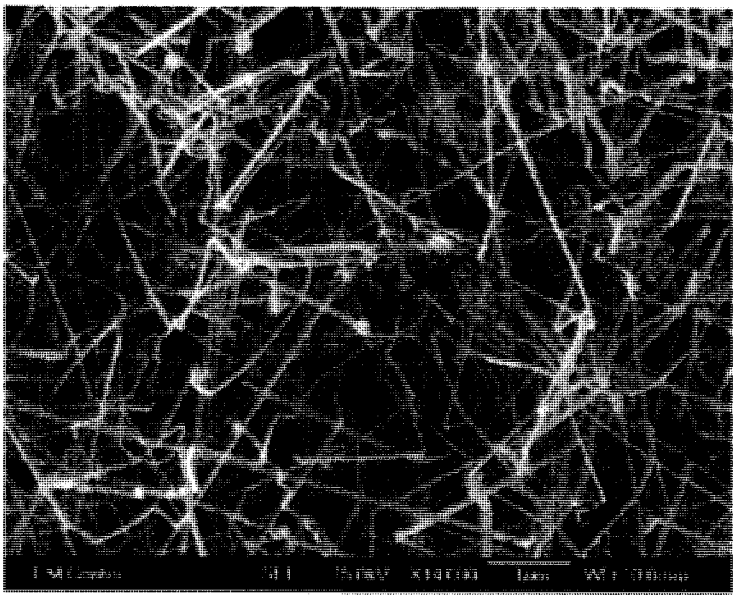

Figure 6.8 SEM image of SnO_2 1-D nanostructures. Green arrow indicates a foreign material attached to the tip of one nanowire.

Similar to SEM observations, TEM studies also confirmed the presence of a foreign material at the tip of nanostructures [Figure 6.9a]. Most of these foreign materials were of spherical, while others displayed irregular structures. Foreign materials on the tips of nanowire is an indication of a VLS growth mechanism. TEM results also indicated that the 1-D nanostructures were not uniform in shape. Figure

6.9b shows a different square-tip morphology where no foreign material attached. This could be the result from a broken wire, the original growth end with no catalyst particles, or from another possible growth mechanism. The vapor-solid (V-S) mechanism, a self-catalyst growth mechanism, is another plausible explanation for the formation of the nanowires showing no foreign material on the tip, however, it is unlikely that the growth conditions could support two competing growth mechanisms that result the similar shaped products. HR-TEM images of these nanostructures [Figure 6.10] were also obtained. They frequently revealed uniform lattice fringes with a 2.2 Å spacing showing that some of these 1-D nanostructures were single-crystalline.

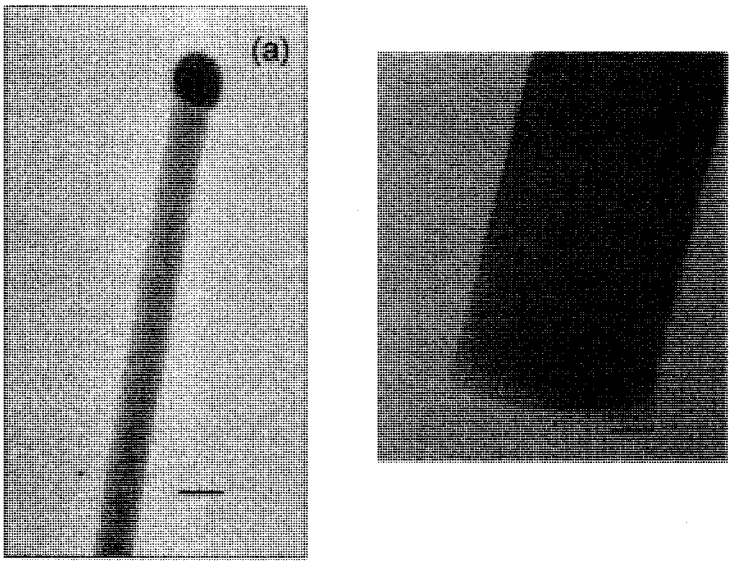

Figure 6.9 TEM images revealed different tip shapes of the 1-D nanostructures. a: spherical object attached to the tip, b: flat (square) tip of the 1-D structures. The scale bar is equal to 10 nm.

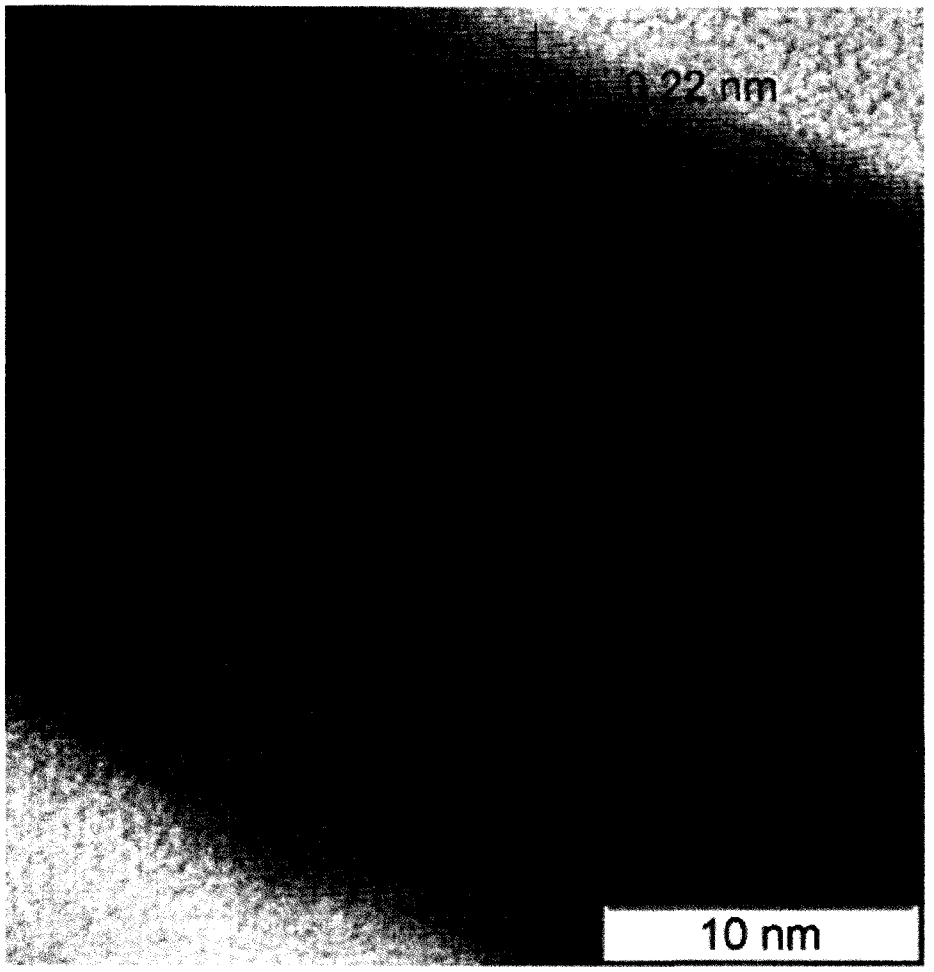

Figure 6.10 HR-TEM image reveals the lattice fringes on the 1-D nanostructure.

6.4.2 Experimental results from varying different reaction parameters

Experiments were carried out varying the reaction time from 0.5 hour to 1.5 hours (Table 6.1, Exp.#1-3). Figure 6.11 shows SEM images of the obtained 1-D nanostructures on the Au-coated Si wafer with (a) 0.5 hour duration (b) 1 hour duration at 600 °C. With shorter reaction time, only short 1-D nanostructures were found. These shorter structures had larger diameters, and irregular shapes. The longer reaction time (1 hour) produced longer and more slender 1-D nanostructures.

However, no obvious difference was observed when comparing the products obtained from 1 hour and 1.5 hours reaction time. One could speculate that the source (i.e. Sn) was exhausted after about 1 hour of heating, terminating the growth of the 1-D nanostructures.

The effect of reaction temperature on the 1-D nanostructure synthesis was also investigated. Three different furnace temperatures (350, 475 and 600 °C) were employed (Table 6.1, Exp.# 4-6). The same substrate preparation (Au-coated Si) and heating procedures were used. No 1-D nanostructures could be found on the Au-coated Si substrate from the experiments at the two lower temperatures (350 and 475 °C). Only bead-like nanoparticles containing Au were found on the Si substrate. The reacted precursor powder area, indicated by the SEM/EDS results, was amorphous-like, with no specific structures were found from the area. Only higher furnace temperatures of around 600 °C resulted in growth of the 1-D nanostructures. The higher temperature might generate some Sn vapor pressure from decomposition of the precursor powder, which was then transported to the area around precursor, and consumed during the formation of 1-D nanostructures.

The Si substrates without gold deposition were used as a control (Table 6.1, Exp.# 7). $Sn(dedtc)_4$ powder was again distributed on the substrate, and the same heating procedure was carried out. After heating for one hour at 600 °C, it was found that the bare Si area (the area without precursor powder) did not produce any 1-D structures. It indicated that the presence of gold particles was necessary for the growth of SnO_2 1-D nanostructures, which supports the proposed VLS mechanism.

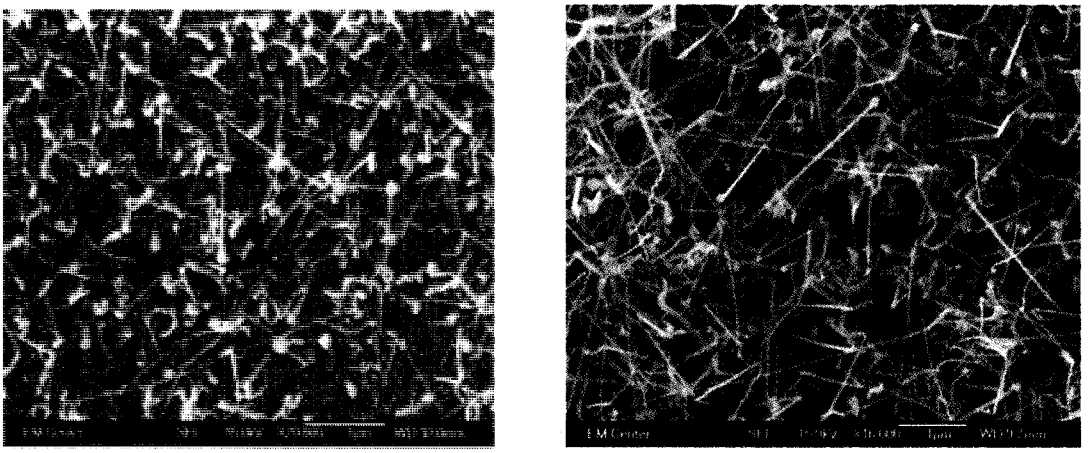

Figure 6.11 SEM images of the 1-D nanostructures produced by two different reaction durations: (left-a) 0.5 hour, (right-b) 1.5 hours.

As mentioned previously, SEM and TEM images both revealed foreign materials at the tip of some 1-D nanostructures, and EDX results indicated that this foreign material contained both Au and Si. A previous study has shown that Si from the substrate tends to diffuse into the Au seeds when the reaction temperature exceeds the eutectic temperature of the Au-Si system (363 °C).[29] Since the reaction temperature was 600 °C in this case, the eutectic melt of the Au-Si alloy is believed to initiate the nucleation of the 1-D nanostructures. As the precursor of Sn decomposed at 600 °C, a small amount of vapor containing Sn was generated and re-deposited back to the surrounding area containing heads of Au-Si melt. Supersaturation of this melt with Sn and subsequent reaction with oxygen contamination in the furnace led to the growth of SnO_2 1-D nanostructures.

Oxygen contamination was found to be important in the growth of SnO_2 1-D nanostructures. With the furnace setup eliminating the oxygen source (see Section

6.3), no 1-D nanostructure was found from the Au-coated Si substrate. Only bead-like nanoparticles [Figure 6.12] were found from the substrate. This finding suggested that oxide formation promotes the growth of SnO_2 1-D nanostructures.

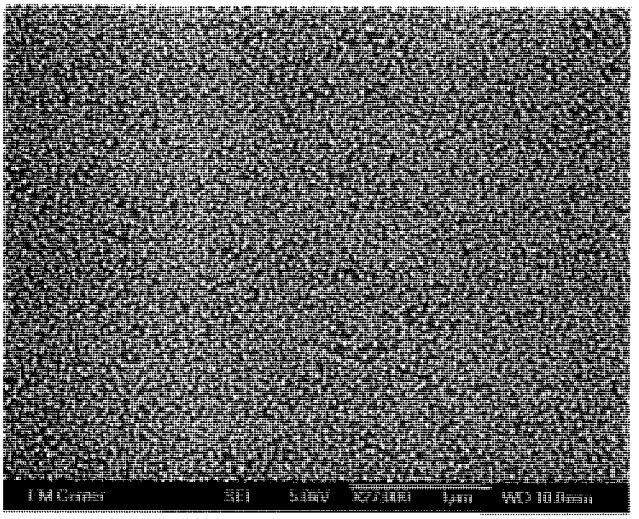

Figure 6.12 SEM image of the Au-coated Si substrate after pyrolysis with Lindberg blue M furnace. The bead-like nanoparticles containing Au were found on the substrate.

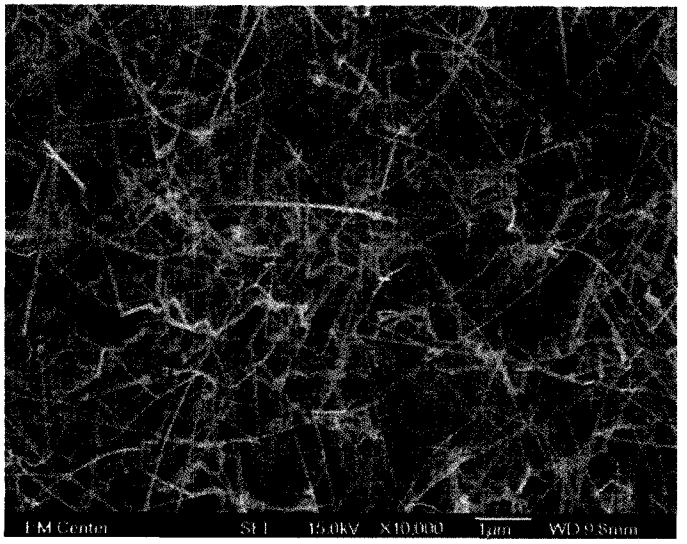

Figure 6.13 SEM image of the 1-D nanostructure grown on the Au-coated Mo substrate.

Silicon, copper, and molybdenum were all utilized as the substrate (Table 6.1, Exp.# 8-9). The same cleaning treatment, along with 5 nm of Au deposited on the surface, were done for all substrates. In addition the same heating procedure (at 600 °C, 1 hour duration) was carried out. When copper was applied as the substrate, no 1-D nanostructures were observed. On the other hand, when molybdenum was employed, SnO_2 1-D nanostructures were found, as shown in Figure 6.13. It indicated that the growth process of these 1-D nanostructures is substrate dependent, which again suggested that the importance of alloy formation for initiating the growth of nanostructures. However, the findings contradicted the information given by the phase diagram: from the Cu-Au phase diagram, Au and Cu do not form an alloy at 600 °C; and no Mo-Au phase diagram can be found since Au and Mo are not miscible at any temperature. It is possible that other factors could also contribute to the alloy formation of Mo-Au system which is still an unknown at this point.

According to the proposed mechanism, it appears that $Sn(dedtc)_4$ might not be necessary to support the reaction. Another precursor, which provides the source of Sn, might also be used in this reaction for generating SnO_2 1-D nanostructures. To prove this point, tin (IV) tetrachloride pentahydrate ($SnCl_4 \cdot 5H_2O$) was used as the precursor instead of $Sn(dedtc)_4$ (Table 6.1, Exp.#10). By carrying the same experimental procedures, 1-D nanostructures were formed [Figure 6.14]. The shapes of these 1-D nanostructures, however, appeared to be different from those generated with $Sn(dedtc)_4$ as the precursor. Two major types of 1-D nanostructures were found within the sample: one structure was thinner, with tapered ends. The other was more

rigid and contained larger sized crystals with spherical shaped materials attached to the tip. EDS results revealed that these materials obtained Sn and O, with the ratio of 1:2, and with Si contamination. Further investigation is required in order to explain the difference in appearance of these 1-D nanostructures made from $SnCl_4 \cdot 5H_2O$.

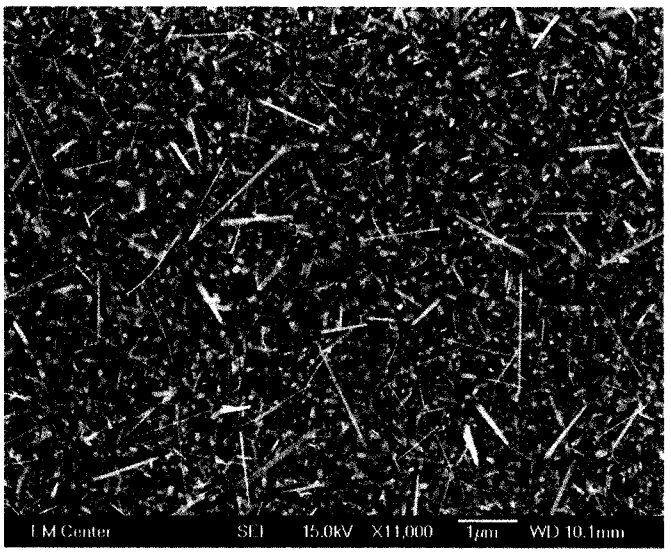

Figure 6.14 SEM image of 1-D nanostructures with $SnCl_4 \cdot 5H_2O$ used as the precursor.

The growth mechanism can be described as follows: the growth process begins with the formation of beads of Au-Si alloy. The Sn vapor from the precursor [$Sn(dedtc)_4$] dissolves in Au-Si alloy melts and then reacts with oxygen in the furnace to form nanowires. The supersaturation of SnO_2 in Au-Si alloy leads to the precipitation of SnO_2 nanowires at the end.

6.5 Conclusion:

A simple, one-step pyrolysis procedure for synthesizing 1-D SnO_2 nanostructures was investigated. The effects of reaction parameters, such as reaction duration, temperature, the identity of the substrate and single source precursor, were investigated. The presence of foreign materials attached to the tip of the 1-D nanostructures suggests the VLS growth mechanism. Further experimentation is necessary to explore the structural differences of nanostructures composed of $Sn(dedtc)_4$ compared to those composed of $SnCl_4$.

***Reference*:**

1. Cobden, D. H., Molecular electronics. Nanowires begin to shine. *Nature* **2001,** 409, (6816), 32-33.

2. Tseng, G. Y.; Ellenbogen , J. C., Nanotechnology. Toward nanocomputers. *Science* **2001,** 294, (5545), 1293-1294.

3. Service, R. F., Nanocomputering. World's smallest transistor. *Science* **2001,** 293, (5531), 796.

4. Gao, T.; Meng, G. W.; Zhang, J.; Sun, S.; Zhang, L., Template synthesis of Y-junction metal nanowires. *Appl. Phys. A* **2002,** 74, (3), 403-406.

5. Zhang, X. Y.; Zhang, L. D.; Chen, W.; Meng, G. W.; Zheng, M. J.; Zhao, L. X.; Phillipp, F., Electrochemical fabrication of highly ordered semiconductor and metallic nanowire arrays. *Chem. Mater.* **2001,** 13, (8), 2511-2515.

6. Martin, C. R., Nanomaterials-a membrane-based synthetic approach. *Science* **1994,** 266, 1961-1966.

7. Manna, L.; Scher, E. C.; Alivisatos, A. P., Synthesis of soluble and processable rod-. arrow-. teardrop-, and tetrapod-shaped CdSe nanocrystals. *J. Am. Chem. Soc.* **2000,** 122, (51), 12700-12706.

8. Peng, Z. A.; Peng, X. G., Mechanisms of the shape evolution of CdSe nanocrystals. *J. Am. Chem. Soc.* **2001,** 123, 1389-1395.

9. Pan, Z. W.; Dai, Z. R.; Wang, Z. L., Nanobelts of semiconducting oxides. *Science* **2001,** 291, 1947-1949.

10. Peng, X. S.; Meng, G. W.; Wang, X. F.; Wang, Y. W.; Zhang, J.; Liu, X.; Zhang, L. D., Synthesis of oxygen-deficient indium-tin-oxide (ITO) nanofibers. *Chem. Mater.* **2002,** 14, (11), 4490-4493.

11. Lopez-Lopez, M.; Guillen-Crvantes, A.; Rivera-Alvarez, Z.; Hernandez-Calderon, I., Hillock formation during the molecular beam epitaxial growth of ZnSe on GaAs substrates. *J. Cryst. Growth* **1998,** 193, (4), 528-434.

12. Kind, H.; Yan, H.; Law, M.; Messer, B.; Yang, P., Nanowire UV photodetector and optical switches. *Adv. mater.* **2002,** 14, 158-160.

13. Law, M.; Kind, H.; Messer, B.; Kim, F.; Yang, P. D., Photochemical sensing of NO_2 with SnO_2 nanoribbon nanosensors at room temperature. *Angew. Chem. Int. Ed.* **2002,** 41, 2405-2408.

14. Hu, J. Q.; Bando, Y.; Golberg, D., Self-catalyst growth and optical properties of novel SnO_2 fishbone-like nanoribbons. *Chem. Phys. Lett.* **2003,** 372, 758-762.

15. Badawy, W. A.; Afify, N. H.; Elgiar, E. M., Optical and photovoltaic characteristics of In-modified SnO_2 thin films. *J. Electrochem. Soc.* **1990,** 137, 1592-1595.

16. He, Y. S.; Campbell, J. C.; Murphy, R. C.; Arendt, M. F.; Swinnea, J. S., Electrical and optical characterization of Sb: SnO_2. *J. Mater. Res.* **1993,** 8, 3131-3134.

17. Moreno, M. S.; Varela, A.; Otero-Diaz, L. D., Cation nonstoichiometry in tin-monoxide-phase $Sn_{1-\delta}O$ with tweed microstructure. *Phys. Rev. B* **1997,** 56, 5186-5192.

18. Watson, J., The tin oxide gas sensor and its application. *Sens. Actuators* **1984,** 5, 29.

19. Yamazoe, N., New approaches for improving semiconductor gas sensors. *Sens. Actuators B* **1991,** 5, 7.

20. Sberveglieri, G., Classical and novel techniques for the preparation of SnO_2 gas sensors. *Sens. Actuators B* **1992,** 6, 239.

21. Nayral, C.; Viala, E.; Colliere, V.; Fau, P.; Senocq, F.; Maisonnat, A.; Chaudret, B., Synthesis and use of a novel SnO_2 nanomaterial for gas sensing. *Appl. Surf. Sci.* **2000,** 164, 219-226.

22. Wang, Y. L.; Jiang, X. C.; Xia, Y. N., A solution-phase, precursor route to polycrystalline SnO_2 nanowires that can be used for gas sensing under ambient conditions. *J. Am. Chem. Soc.* **2003,** 125, 16176-16188.

23. Kim, T. W.; Lee, D. U.; Lee, J. H.; Choo, D. C.; Jung, M.; Yoon, Y. S., Structural, electrical, and optical properties of SnO_2 nanocrystalline thin films grown on p-InSb (111) substrates. *J. Appl. Phys.* **2001,** 90, (1), 175-180.

24. Yu, K. N.; Xiong, Y. H.; Liu, Y. L.; Xiong, C. H., Microstructural change of nano-SnO_2 grain assemblages with the annealing temperature. *Phys. Rev. B* **1997,** 55, (4), 2666-2671.

25. Dai, Z. R.; Pan, Z. W.; Wang, Z. L., Ultra-long single crystalline nanoribbons of tin oxide. *Solid State Commun.* **2001,** 118, 351-354.

26. Peng, X. S.; Zhang, L. D.; Meng, G. W.; Tian, Y. T.; Lin, Y.; Geng, B. Y.; Sun, S. H., Micro-raman and infrared properties of SnO_2 nanobelts synthesized from Sn and SiO_2 powders. *J. Appl. Phys.* **2003,** 93, (3), 1760-1763.

27. Liu, Y. K.; Zheng, C. L.; Wang, W. Z.; Yin, C. R.; Wang, G. G., Synthesis and characterization of rutile SnO_2 nanorods. *Adv. mater.* **2001,** 14, (24), 1883-1887.

28. Zheng, M. J.; Li, G. G.; Zhang, X. Y.; Huang, S. Y.; Lei, Y.; Zhang, L. D., Fabrication and structural characterization of large-scale uniform SnO_2 nanowire array embedded in anodic alumina membrane. *Chem. Mater.* **2001,** 13, 3859-3861.

29. Paulose, M.; Karghese, O. K.; Grimes, C. A., Au-Si composite nanowires from SLS growth. *J. Nanosci. Nanotech.* **2003,** 3, 341-346.

Chapter 7: Concluding Remarks And Future Work

This dissertation reviewed three different synthetic routes for the preparation of metal chalcogenide nanostructures: laser ablation, solution-phase synthesis, and pyrolysis. Different metal chalcogenides (including MoS_2, TaS_2, and SnS) and metal oxide (SnO_2) of different morphologies were resulted by employing the three synthetic routes. Various standard techniques, such as TGA, TEM, HR-TEM, SEM/EDX, and XRD, were performed in order to characterize the nanostructures.

In the laser ablation project, three different laser ablation conditions were employed for nanomaterial synthesis: laser ablation in an inert gas atmosphere with a nanosecond pulsed laser [Chapter 3], laser ablation in solution phase synthesis with a nanosecond pulsed laser [Chapter 4], and laser ablation with a femtosecond pulsed laser [Chapter 4]. The reaction conditions and their products are summarized in Table 7.1.

Table 7.1 Summary of laser ablation experiments

Laser ablation/target materials	Ablated environment	Laser type	Products
Project 1 (TaS_2)	Ar gas (200 Torr)	Nanosecond pulsed laser	Nanoplatelets, spheroids
Project 2 (TaS_2)	TBS	Nanosecond pulsed laser	Polydisperse-nanospheres
Project 3 (MoS_2)	Ar gas (50 Torr)	Femtosecond pulsed laser	Nanospheres, flake-like nanoparticles, nano-octahedra

For the first laser ablation project [Chapter 3], a TaS_2 pellet was used as the target material. A pulsed Nd:YAG laser was used to ablate the TaS_2 target under an Ar atmosphere. Nanoplatelets of TaS_2 were synthesized as the majority product through this process. Different laser power densities were employed in order to study their effects on the nanomaterials. It was found that smaller nanoplatelets were formed with the higher power laser ablation. Furthermore, the size distribution of the smaller sized nanoplatelets was closer to the normal distribution (Gaussian distribution).

A growth mechanism for laser ablation of TaS_2 in Ar atmosphere was proposed. It was suggested that the interaction of laser pulse with target materials (TaS_2) leads to vaporization, and ionization of the materials. Plasma expansion after the laser pulse causes cooling of the plasma plume, which creates the environment for cultivating nanomaterials. During the cooling process, Ta vapor first condenses to form a template metal crystallite. The template of Ta then reacts with the surrounding S vapor leading to the formation of TaS_2 nanoplatelets. Since the higher the laser power density, the faster the cooling rate is. Smaller nanoplatelets can be generated with a higher laser power density.

The unprotected TaS_2 nanoplatelets were found to be unstable when exposed to air. The periphery of the nanoplatelets contains unsaturated bonds that lead to the oxidation of the material. XRD and TEM images confirmed the oxidation of these nanoplatelets. In order to prevent the oxidation and to further disperse the materials, the as-produced nanoplatelets were sonicated in 3-MPA solution. TEM results

indicated that 3-MPA treated TaS_2 nanoplatelets remained after exposure to air for 8 days.

For the second laser ablation related project (Chapter 4), the reaction took place in a liquid medium, with TaS_2 used as the target material. The powder of TaS_2 was first dispersed in TBS. A pulsed Nd: YAG laser was employed as the laser source. The dispersion of TaS_2 was exposed to laser pulses while being stirred. Polydisperse TaS_2 nanospheres were produced. The larger-size nanospheres displayed the closed-cage structures. The identity of the smaller-size nanospheres, remains unknown. Some of these smaller size nanospheres appeared to be crystalline. In order to study different sizes of nanospheres prepared by this laser irradiation process, separation procedure, such as through sedimentation, will be necessary. Acquisition of XRD will also be required in order to provide a full characterization of these nanospheres. Finally, a large range of different laser power densities should be employed to fully study the effect on the nanostructures.

In the third laser ablation project, a MoS_2 target pellet was laser ablated by a femtosecond pulsed laser. The project is a collaboration between the Parkinson group and the Squier group at the Colorado School of Mines. It is known that the plasma characteristics produced by the femtosecond pulsed laser is different from that of the nanosecond pulsed laser, and the formation of the nanostructures from the laser ablation is directly related to the plasma plume. The alteration of the nanostructure morphology by switching from a nanosecond to femtosecond pulse laser, therefore,

was proposed. The preliminary result, however, shows that high yield of nano-octahedra were formed from the ablation with femtosecond pulsed laser.

The laser ablation with femtosecond pulsed laser project is still in progress. More experiments will be necessary in order to elucidate the effect of using the femtosecond pulsed laser on the nanostructures synthesis. Different ablation parameters will be varied: different pressures of the inert gas (i.e. Ar) will be used, different laser power densities will also be employed. Some studies suggested that nanostructures can be found from the craters on the target, which are created by the impact of laser ablation. Therefore, it will be beneficial to further examine the craters.

In project of solution-phase synthesis, SnS 1-D nanostructures were prepared [Chapter 5]. Single source precursor, $Sn(dedtc)_4$ which contained both Sn and S sources, was first dispersed in diethylene glycol and was added to the hot tergitol. The mixture was under reflux, and yielded SnS 1-D nanostructures.

In this particular reaction, the concentration of a single source precursor was found to be critical in terms of synthesizing the desired 1-D nanostructures: high concentration of single source precursors did not yield any 1-D nanostructures. Only with low concentration of a single source precursor, were able to generate 1-D nanostructures. Reaction mixture temperature when precursor dispersion was added was also found to be affecting the morphology of the 1-D nanostructure. Only with the appropriate intermediate temperature of 310 °C yielded the desired 1-D nanostructures. Reaction temperature of too high or too low yielded amorphous or

bulk materials. Finally, the use of different secondary solvents, including diethylene glycol, ethyelene glycol, and tergitol, was investigated for the reactions. Only when diethylene glycol was used as the secondary solvent, did the SnS 1-D nanostructures form. In the solution-phase synthesis, diethylene glycol was acted in two roles: (a) to transfer single source precursor to the hot-tergitol, (b) to create the appropriate temperature of the reaction mixture (tergitol and diethylene glycol) for both decomposing the single source precursor and nucleation of the 1-D nanostructures.

The reaction conditions of the solution-phase synthesis might not yet be optimized, as other SnS nanostructures, such as nano-tetrahedra, were also found among the products. Nonetheless, the SnS 1-D nanostructures were always the majority products from this solution-phase synthesis.

The growth mechanism of the solution-phase synthesis follows the path of nucleation and growth of crystals: single source precursor is transferred to the hot tergitol by diethylene glycol, and leads to the decomposition of precursors. Nucleation, dissolution, and growth occur simultaneously that lead to the formation of SnS 1-D nanostructures.

In the project of pyrolysis, SnO_2 1-D nanostructures were synthesized [Chapter 6]. The same single source precursor from the solution-phase project, $Sn(dedtc)_4$, was distributed on a Au-coated Si substrate. The prepared substrate then was pyrolysied in the furnace at 600 °C under the flow of nitrogen. The 1-D nanostructures of SnO_2 were found from the surrounding of the precursor powder.

The spherical materials found on the tips of most 1-D nanostructures depicted the VLS growth mechanism. Different experiments have been conducted in order to further demonstrate the growth mechanisms of this specific pyrolysis. It was found that substrate, as well as catalyst seeds (i.e. Au), were the important factors in the growth of 1-D nanostructure, indicated that the formation of an alloy of Au/Si was necessary for the growth. The heating temperature was also found to be important, since it controlled the amount of Sn ready for the reaction.

The overall growth mechanism of SnO_2 nanostructures via VLS mechanism can be viewed as follows: When the Si substrate is heated above the eutectic temperature of Au-Si system, Si diffuses into Au and forms Au-Si alloy. The Sn vapor (from heating the precursor powder) reacts with the oxygen (contamination from furnace), and diffuses into the Au-Si alloy seeds. The supersaturation of SnO_2 in Au-Si alloy then leads to the precipitation of SnO_2 nanowires at the end.